Summer 8-17-2018

Development of Macromolecular Prodrug Conjugates for the Diagnosis and Treatment of Musculoskeletal Diseases

Xin Wei
University of Nebraska Medical Center

DEVELOPMENT OF MACROMOLECULAR PRODRUG CONJUGATES FOR THE DIAGNOSIS AND TREATMENT OF MUSCULOSKELETAL DISEASES

by

Xin Wei

A DISSERTATION

Presented to the Faculty of

The Graduate College in the University of Nebraska

In Partial Fulfillment of the Requirements

For the Degree of Doctor of Philosophy

Department of Pharmaceutical Sciences

Under the Supervision of Professor Dong Wang

University of Nebraska Medical Center

Omaha, Nebraska

July 2018

Supervisory Committee:

Dong Wang, Ph.D.

Kevin L. Garvin, M.D.

Joseph A. Vetro, Ph.D.

Geoffrey M. Thiele, Ph.D.

Dedicated to my dear grandparents, my parents and my in-laws who supported me with all their love, my beloved husband, Gang, my two distracting little boys, Marc and Victor without whom this thesis would have been completed two years earlier…

TABLE OF CONTENTS

ACKNOWLEDGEMENTS

Firstly, I would like to sincerely thank my supervisor and the chair of my supervisory committee, Dr. Dong Wang for his diligent and tireless guidance throughout my Ph.D. research. From the first time I met him at a meeting in Beijing, China, I was deeply impressed by his gentleman manner and immense knowledge. I have been extremely lucky to have a mentor who cared so much about not only my work but also my personal life and my career development. He taught me not only to become a troubleshooter, an experiment designer, a pure great scientist, but also to be an enthusiastic, grateful and kind person.

I also would like to thank members of my PhD supervisory committees, Drs. Kevin Garvin, Geoffrey Thiele, and Joseph Vetro for their valuable guidance, suggestions and encouragement on my project. Specially, I want to thank Dr. Thiele for his guidance on the immunology aspect of my studies; Dr. Vetro for his suggestions regarding my experimental design and his generosity in sharing his instruments; and Dr. Garvin for guiding me with his immense clinical knowledge and expertise.

I would like to thank the China Scholarship Council (Grant # 201206170147) and National Institute of Health (R01 AR062680, R01 AI119090) for financial support during my study. I would like to thank the UNMC Graduate Studies and Department of Pharmaceutical Sciences. I would like to thank all the UNMC core facility staff and members in the UNMC animal facility for their extraordinary support.

I would also like to thank all the present and present members from Dr. Wang's lab. I wish to especially thank Drs. Zhenshan Jia, Fei Li, Jianbo Wu and Rongguo Ren for their professional advice and guidance on chemistry throughout my project. I would like to thank Drs. Hongjiang Yuan, Fang Yuan, Ke Ren, Yijia Zhang, and Yanzhi Liu for their training on animal surgery and biological analyses, and Ms. Xiaoyan Wang for her help on micro-CT analysis. I would like to thank Dr. Libin Yang and Fan Zhang for their help on animal experiments, and Dhruvkumar Soni for HPLC analysis. I would like to thank Laura Weber for her suggestions on scientific writing. I would also like to thank Xiaobei Wang, Drs. Junxiao Yang and Zhirong Zhong for their support and help.

I would like to thank all my friends and colleagues for their help and support in the past six years. I would like to thank Xinyan Zhang, Fang Yuan, Ke Ren, Yijia Zhang, Jianbo Wu, Rongguo Ren, Zhenshan Jia, Hongjiang Yuan, Dongwei Guo, Zhihao Mao, Yuning Zhang, Xiaoyan Wang, Chao Fu, Yang Peng, Hongjun Wang, Yuliang Zhang, Tian Zhou, Zhiyi Lin, Fan Zhang, You Zhou for the lifelong friendship. Without them, life cannot be so valuable and memorable.

Finally, I would like to thank all my family. I would like to thank my husband, my colleague and co-author of my published papers, Gang Zhao, who is always there for me with endless love, tolerance and company, in the school and at home; to my parents Li Ma and Jun Wei, who are continuously encouraging me and always being a good and hardworking model for me; to my in-laws Qinghua Shan and Lijun Zhao, who loves me as their own daughter and supporting our family with all their love without any complain; and to my two little boys, Marc Zhao and

Victor Zhao, from whom I know more about what love, responsibility, and trust is; for whom I will never give up to become stronger, braver and better me.

ABSTRACT

DEVELOPMENT OF MACROMOLECULAR PRODRUG CONJUGATES FOR THE DIAGNOSIS AND TREATMENT OF MUSCULOSKELETAL DISEASES

Macromolecular prodrug conjugate is a promising strategy for better diagnosis and treatment of musculoskeletal diseases. Our lab has pioneered this effort and has successfully developed multiple prodrug formulations. The general approach we have taken is to incorporate active ingredient (AI, including imaging probe or therapeutic agents) containing monomers into water-soluble and biocompatible polymers, such as *N*-(2-Hydroxypropyl) methacrylamide (HPMA) copolymers. Structural parameters of these polymeric prodrugs, such as molecular weight (MW), drug loading, prodrug activation mechanism and the selection of drug payload may greatly affect therapeutic efficacy and the safety of the macromolecular prodrugs. To investigate the impact of these structural parameters in my research, (1) We have synthesized a series of the HPMA copolymer-based dexamethasone prodrugs with different molecular weight and drug loading. After labeling with ^{125}I or fluorescent dye, these prodrugs were administered to a murine implant loosening model. The *in vivo/ex vivo* pharmacokinetics and biodistribution of these polymers and *in vitro* and *in vivo* cellular internalization were analyzed and compared. (2) We designed and synthesized dexamethasone-containing monomers with different releasing chemistry and copolymerized with HPMA. The different *in vitro* releasing rates of these prodrugs were confirmed. When evaluated in an adjuvant induced arthritis rat model, these prodrugs demonstrated significantly different

therapeutic efficacy and duration. (3) To understand if the design principle we learned from the dexamethasone prodrug can be extrapolated to other class of drugs, we replaced dexamethasone with Tofacitinib (Tofa, a disease-modifying antirheumatic drug or DMARD) in the prodrug design. The resulting prodrug (P-Tofa) was found to effectively ameliorate joint inflammation of the adjuvant-induced arthritis rat model. Collectively, the results from these systematic investigations provide us with more insight into the polymeric prodrug design principle and are instructive for the future development and clinical translation of the macromolecular prodrugs for musculoskeletal and other relevant diseases.

LIST OF TABLES

LIST OF FIGURES

LIST OF ABBREVIATIONS

AA	Adjuvant-induced arthritis
AI	Active ingredient
AI	Articular index
AIBN	2,2′-azobisisobutyronitrile
ALP	Alkaline phosphatase
ALT	Alanine aminotransferase
APMA	*N-(3-aminopropyl) methacrylamide hydrochloride*
arg1	Arginase-1
AST	Aspartate aminotransferase
AUC	Area under the concentration-time curve
AUC_{blood}	Area under the concentration-time curve in plasma
AUC_{last}	Area under the concentration-time curve up to the last measurable concentration
AUC_{tissue}	Area under the concentration-time curve in soft tissues
BA	Basophils
BMD	Bone mineral density
BMM	Bone marrow derived macrophage
BS/TV	Bone surface density
BV	Bone volume
BV/TV	Percent bone volume
CL	Total clearance
CMC	Critical micelle concentration

CT	Computerized tomography
CTA	Chain transfer agent
DEMARD	Disease-modifying antirheumatic drug
Dex	Dexamethasone
DIPEA	Diisopropylethylamine
DLS	Dynamic light scattering
DMARDs	Disease modifying anti-rheumatic drugs
DMF	*N,N-dimethylformamide*
DMSO	Dimethyl sulfoxide
EDC	*N-(3-dimethylaminopropyl)-N'-ethylcarbodiimide hydrochloride*
ELVIS	*Extravasation through Leaky Vasculature and Inflammatory cell-mediated Sequestration*
EO	Eosinophils
FACS	Fluorescence-activated cell scanning
FDA	Food and Drug Administration
FPLC	Fast protein liquid chromatography
GC	Glucocorticoids
HEMA	Hydroxyethyl methacrylate
HEMA-COCl	Methacryloxyethyl chloroformate
HOBt	Hydroxybenzotriazole
HPLC	High performance liquid chromatography
HPMA	*N*-(2-Hydroxypropyl) methacrylamide
IACUC	Institutional Animal Care and Use Committee

ID/g	Injected dose per gram of tissue isolated
IHC	Immunohistochemistry
JAK	Janus kinase
LUV	Large unilamellar vesicle
LY	Lymphocytes
MA-Dex	*N*-Methacryloyl glycylglycylhydrazyl dexamethasone
MA-Tyr-NH_2	*N*-Methacryloyl tyrosine amide
MLV	Multilamellar vesicle
M_n	Number average molecular weight
MO	Monocytes
MPS	Mononuclear phagocytic system
MRI	Magnetic resonance imaging
MSD	Musculoskeletal diseases
MTX	Methotrexate
MW	Molecular weight
M_w	Weight average molecular weight
NE	Neutrophils
NIR	Near-infrared
NSAIDs	Nonsteroidal anti-inflammatory drugs
PBS	Phosphate-buffered saline
PCL	Poly(ε-caprolactone)
P-Dex	HPMA copolymer-dexamethasone conjugate
P-Dex-A	HPMA copolymer-dexamethasone conjugate with monomer A

P-Dex-Alexa	Alexa Fluor® 488-labeled HPMA copolymer-dexamethasone conjugate
P-Dex-APMA	Copolymers of HPMA and *N*-(3-aminopropyl) methacrylamide
P-Dex-B	HPMA copolymer-dexamethasone conjugate with monomer B
P-Dex-C	HPMA copolymer-dexamethasone conjugate with monomer C
P-Dex-D	HPMA copolymer-dexamethasone conjugate with monomer D
P-Dex-E	HPMA copolymer-dexamethasone conjugate with monomer E
P-Dex-IRDye	IRDye® 800 CW-labeled HPMA copolymer-dexamethasone conjugate
PDI	Polydispersity index
PGA	Poly(glycolicacid)
PHPMA	HPMA homopolymer
PK	Pharmacokinetic
PK/BD	Pharmacokinetics and biodistribution
PLA	Poly(lactic acid)
PLGA	Poly (lactic acid-co-glycolic acid)
PMMA	Poly(methylmethacrylate)
P-Tofa	HPMA copolymer-Tofa conjugate
P-Tofa-Alexa	Alexa Fluor® 647-labeled P-Tofa
RA	Rheumatoid arthritis
RAFT	Reversible addition-fragmentation chain transfer
ROI	Regions of interest
SA-Dex-OA	Sialic acid-dextran-octadecanoic acid

SDS	Sodium dodecyl sulfate
SUV	Small unilamellar vesicle
$t_{1/2}$	Half-life
Tb.N	Trabecular number
Tb.Sp	Trabecular separation
Tb.Th	Trabecular thickness
Tofa	Tofacitinib
V_d	Volume of distribution
WBC	White blood cells

LIST OF CONTRIBUTORS

1. Chapter 2- Dr. Zhenshan Jia designed and guided the synthesis of Dex monomers. Dr. Fang Yuan and Dr. Ke Ren guided the characterization of macromolecular prodrug. Dr. Junxiao Yang guided the polymerization of P-Dex. Dexuan Kong helped with the *in vitro* release study.

2. Chapter 3- Dr. Fei Li radiolabeled the polymers. Dr. Ke Ren and Dr. Hongjiang Yuan guided the animal model establishment. Gang helped with the gamma counter based pharmacokinetics study and flow cytometry study. Dr. Ke Ren and Dr. Yijia Zhang guided the use of Licor system. Dr. Fang guided the flow cytometry study. Drs. Edward Purdue and Christine Averill, Josselyn Galdamez helped with cell culture study. Dr. Yazen Alnouti and Yashpal Singh Chhonker guided and helped with the pharmacokinetics data analyses. Dr. Kevin Garvin helped with reviewing the data and the manuscript. Xiaoyan Wang helped with the optical images data processing.

3. Chapter 4- Gang Zhao, Ningrong Chen and Yuanyuan Sun helped with the *in vivo* experiment. Yuanyuan Sun helped with the micro-CT scanning. Gang Zhao helped with the micro-CT data collection and analyses.

4. Chapter 5- Dr. Jianbo Wu guided with the synthesis of the P-Tofa. Dhruvkumar Soni conducted drug loading and in vitro release study, data interpretation and manuscript preparation.

5. Chapter 6- Drs. Josselyn Galdamez and Edward Purdu helped the cell culture studies and CXCL10 ELISA assays, participated in the data interpretation and manuscript preparation. Gang Zhao assisted with μ-CT scanning/data processing, designed the immunohistochemistry experiments. Drs. Xiaoyan Wang and Yanzhi Liu assisted with μ-CT scanning, animal care, joint measurement, scoring and administration of analgesics.

CHAPTER 1.

INTRODUCTION

1.1 Musculoskeletal Disorders

The musculoskeletal system is comprised of bones, muscles, cartilage, tendons, and ligaments, as well as joints, and other connective tissues [1]. In addition to supporting the body, providing locomotion, the musculoskeletal system protects the vital soft tissue organs in the body and harbors hematopoietic tissues (in the bone marrow) and act as a reservoir for inorganic ions such as calcium and phosphorus [2]. The pathologic disorders of the musculoskeletal tissues affect large population of people, resulting in acute or chronic pain, loss of body motion, reduction of the life quality and even mortality. The musculoskeletal diseases (MSD) show highly related with age, body weight (obesity) and work type. Significant economic burden has been reported to be associated with MSD, which affects more than one out of every two persons in the United States age 18 and over, and nearly three out of four age 65 and over [3]. The rate of chronic musculoskeletal conditions found in the adult population is 76% greater than that of chronic circulatory diseases, which include coronary and heart conditions, and nearly twice that of all chronic respiratory conditions [4]. The diseases of the musculoskeletal cover a wide range of the pathological conditions, e.g., metabolic bone disorders (osteoporosis [5], Paget's disease [6], etc.); autoimmune diseases (rheumatoid arthritis,

systemic lupus erythematosus, etc.); degenerative joint disease (osteoarthritis); bone trauma or trauma-induced bone diseases (bone fracture, bone implant loosening, trauma-induced heterotopic ossification) and bone cancers (osteosarcoma, bone metastasis), etc. In this chapter, we will provide an overview of several MSD with high impact.

1.2 Rheumatoid Arthritis

Rheumatoid arthritis (RA) is a chronic, inflammatory disorder that affects 0.8 percent of adults worldwide and around 1 percent of adults in the United States [7, 8]. The disease often leads to crippling pain associated with progressive articular cartilage damage and peri-articular bone erosion. At present, there is no cure for RA [9, 10].

Multiple classes of medications have been developed for the treatment of RA patients. Nonsteroidal anti-inflammatory drugs (NSAIDs) such as ibuprofen, aspirin, ketoprofen and naproxen have been shown to ease pain and inflammation associated with RA [11, 12] but they do not prevent joint damage and are often associated with significant gastrointestinal, renal [13] and cardiovascular side effects [14]. Glucocorticoids (GC) have been widely used to treat RA patients [13]. Their long-term use, however, has been associated with serious side effects including bone loss with increased incidence of fractures, infections, hypertension and cardiovascular complications, and diabetes mellitus [15, 16]. Disease-modifying anti-rheumatic drugs (DMARDs), including methotrexate (MTX), sulfasalazine and leflunomide are currently being utilized to inhibit joint inflammation and

have been shown to impede joint destruction [17]. Multiple biological DMARDs, which selectively target proinflammatory cytokines or immunomodulatory pathways, have also been developed and shown to be clinically effective in suppressing joint inflammation and attenuating joint destruction [18]. The identification of the key role of intracellular kinase signaling pathways in the regulation of proinflammatory cytokines and immune cell activation has led to the recent development of orally available low molecular weight drugs that selectively target individual members of the Janus kinase pathway [19]. As an emerging class of medications, Janus kinase inhibitors (JAK inhibitors) offer new hope to RA patients who have experienced severe side effects or are refractory to current treatments [20].

1.3 Particle-induced implant loosening

Total joint replacement is considered as an excellent surgery for improving the life quality for the patients who are suffering the end-stage of some musculoskeletal disorders, especially joint diseases such as osteoarthritis, inflammatory rheumatoid arthritis or the traumatic bone injury. In 2011, 711,398 total knee replacements and 464,452 total hip replacements were performed. The total cost was over 19 billion dollars [21]. 10-20% of replaced joints, however, need to be revised within 10-20 years after arthroplasty due to the osteoclast-mediated periimplant osteolysis at the interface between bone and implant [22].

The aseptic implant loosening is considered as one of the main causation of the implant failure [23, 24], which is mainly induced by the granulomatous inflammatory reaction triggered by the wear-particle-activated macrophages [25-29].

Macrophages release prostaglandins, cytokines, metalloproteinases and lysosomal enzymes (e.g. TNF-α, IL-1β, IL-6, and PGE-2) upon activation which initiate the bone resorbing pathways cascades [30, 31].

Commonly used imaging tools such as x-ray, computerized tomography (CT) and MRI in clinic have been used in the diagnosis of established bone loss of osteolysis and implant loosening. These methods are very effective in detecting osteolysis and associated loss of implant fixation. However, they only reveal anatomical changes within the limit of their imaging resolution, meaning when definitive evidence of osteolysis is detected, considerable bone loss has already occurred. To better prevent the osteolysis, there is a critical need for a theranostic system that could both detect early wear particle-induced inflammatory events and in addition therapeutically target the inflammatory process and prevent incipient osteolysis. Intervention at the early stage of inflammation would definitely prolong the life-time of the implant and improve long-term patient life quality.

1.4 Heterotopic ossification

Though genetic mutation causing heterotopic ossification (HO) is rare with a prevalence around one of two million [32-35], HO is a common occurrence after multiple forms of extensive trauma, including arthroplasty [36-39], traumatic burn injury [40-43], and central nervous system (CNS) injury [44-47]. It has been reported that the incidence rate of tHO is 10-20% in patients receiving arthroplasty [36], 0.1-3.3% in postburn patients [41], and 20%–30% in spinal cord injured patients [48]. The occurrence rate increases to as high as 63% following combat-related amputation [49] and 60.1% in patients undergoing limb salvage [50]. The

cost of the treatment and prophylaxis of tHO varies depending on the severity, cause, and therapeutic methods [51-53]. tHO does not only induce severe permanent pain [33], joint spasticity and autonomic dysreflexia [54, 55], but also causes increased pressure to the tissue under the tHO site leading to blood clot and deep vein thrombosis which affects blood circulation, possibly resulting in fatality [56].

tHO is a complex process that involves trauma, injury, and stimulations inducing the activation of the inflammation cascade and differentiation of stem cells into chondrocytes and osteoblasts. Severe systemic and stimulation-specific inflammation evident by immediate elevated levels of inflammatory cytokines and elevated injury severity score is associated with the development of tHO [57]. No single simple mechanism currently exists, although many common cellular mechanisms have been investigated within fibrodysplasia ossificans progressiva (FOP) and acquired forms of heterotopic ossification. Several contributory factors have been suggested, including prostaglandin activity, specifically PGE-2, as well as hypercalcemia, tissue hypoxia, alterations in sympathetic nerve activity, prolonged immobilization and imbalances between parathyroid hormone activity and calcitonin [48]. With the discoveries relating cell phenotypes underlying tHO [58-64], the main cellular process of its development is attributed to the differentiation of endothelial-derived mesenchymal stem into chondrocytes and osteoblasts. The micro-environment also plays a role in tHO. When stimulation in the soft tissue occurs, the inflammation starts to play its important precursor role in forming HO [65]. The local implantation that releases BMPs, part of the transforming growth

factor (TGF)-beta superfamily which are central to tissue homeostasis and osteogenesis, induces the formation of the acquired HO [66]. It has been deeply investigated in FOP, that the overactivation of activin receptor-like kinase-2 (ALK2), a type I BMP receptor, is the cause of the FOP. The inhibition of the BMP receptor 1-mediated BMP/SMAD pathway can therefore effectively inhibit HO [67].

The current treatment and prophylaxis for tHO usually include nonsteroidal anti-inflammatory drugs (NSAIDs), radiotherapy, surgical excisions, and physical therapy. In the comparison trial studies, indomethacin showed superior therapeutic efficacy in preventing HO [68] formation compared to other NSAIDs; i.e. ibuprofen [69], aspirin [70], or other COX-2 selective NSAIDs [71-73]. However, side effects typically occur, such as the development of gastrointestinal hemorrhage [68], perforated ulcer [68], and non-selective inhibition of COX-1 leading to the reduction of thromboxane A2, which is essential to platelet aggregation [69]. Systemic administration of high-dose indomethacin and other NSAIDS for HO prophylaxis also leads to an imbalance of the formation and resorption of bone. Irradiation therapy of bone growth and repair was first demonstrated in the 1950s [74], and was established into HO prevention and proven to be effective after hip surgery in 1980s [75]. Currently, lower dose radiation therapy (RT) is used prophylactically pre- and post-operatively in patients with bone trauma or operative treatment [76, 77]. The potential side effects of RT also raise concern, however, such as radiation-induced carcinoma, bony nonunion, and azoospermia [78]. Bisphosphonate was approved from Food and Drug Administration (FDA) to treat tHO to reduce the hypercalcemia

and chemical absorb the calcium, however, limited because its GI toxicity and potential to induce the hypocalcemia and induce the apoptosis of the osteoclast. Surgical excision is sometimes chosen by the patient when partially or completely restricted range of motion (ROM) is evident. However, postoperative prophylaxis is still a reliable way to prevent new HO blast formation [79]. Although the goal of physical therapy in patients with HO is to maintain the ROM and preserve function, the outcome is debatable, because of the passive stretching may cause microtrauma or local hemorrhage leading to inflammatory conditions [80]. Notably, the treatment of FOP not only includes what mentioned above, but also high-dose administration of glucocorticoids to reduce lymphocytic infiltration and tissue edema and treat submandibular swelling [81]. Administration of dexamethasone in particular showed reduced ectopic calcification and limb impairment in ACVR1Q207D overexpressed mice versus vehicle-treated ACVR1Q207D overexpressed mice [67]. However, long-term use of corticoids has not been tested clinically due to the concern of its various side effects [67, 82, 83].

From these disease examples, we learned that the causes, treatments, medical interventions and financial burdens of different MSDs vary significantly. However, the MSD also showed similarities, such like underlying inflammatory conditions, including angiogenesis, inflammatory cell infiltrations, bone, tendon or cartilage involved, which gave the scientists more targets for the drug development strategy for the better therapeutic efficacy and reduced systemic off-target side effect.

1.5 Novel Nanomedicine for Treatment and Diagnosis of the Musculoskeletal Disorders

Different from conventional pharmaceutical product, nanomedicine is a promising approach to offer targeted, sustained and controlled release of drugs at the musculoskeletal pathology. To formulating nanomedicine, we shall understand the nature of the nanomedicine and the factors which will also influence the nanomedicine itself.

1.5.1 Liposomes

Liposomes have been defined as a vehicle for drug delivery since the 1960s [84]. Liposomes are composed of spherical bilayer phospholipid membrane surrounded aqueous core separated from the continuous aqueous solvent. According to the number of lipid layers and the size of the liposomes, they can be categorized into multilamellar vesicle (MLV) [85], small unilamellar vesicle (SUV) [86] and large unilamellar vesicle (LUV) [87]. As drug delivery systems, liposomes have been applied to encapsulate both hydrophobic and hydrophilic drug. Besides its wide drug category loading capacity, liposomes delivery system can also protect the cargoes from enzymatic degradation or oxidation and enhance the intracellular uptake. To ensure their stealth against the mononuclear phagocyte system (MPS) liposome formulations can be decorated with inert water-soluble polymers (e.g., PEG, HPMA copolymer, etc.). For certain purpose, targeting moieties or imaging probes can also be used to modify the surface of the liposomes. The first FDA

approved nano-drug, liposomal-doxorubicin (also called Doxil or Lipodox or Myocet), was approved to use on the treatment of several cancer disease including the treatment of soft tissue sarcomas [88-90].

1.5.2 Micelles

Micelles are amphiphilic molecules consisted self-assembled colloidal systems, which can spontaneously aggregate into particles at a concentration higher than the critical micelle concentration (CMC). The size and the shape of the micelle can varie from 10 nm to over 100 nm, spherical [91], ellipsoid cylindered, worm-like or monolayer micelle [92]. A typical micelle has hydrophilic tails forming a shell structure, and the inner hydrophobic structure can encapsulate or conjugate with poorly water-soluble drugs. This structure can be achieved using three types of the macromolecular drugs: 1. The molecule is composed of the one polar end (hydrophilic group) and one non-polar end (hydrophobic group) [93]. 2. Two polar ends with the non-polar center [91]. 3. Two non-polar ends with the polar center [94]. There are no FDA approved micellar drugs to treat MSDs now, however there are many researchers investigating on this type of nanomedicine [95]. Xu, *et al.* developed a conjugation system of sialic acid-dextran-octadecanoic acid (SA-Dex-OA), which can self-assemble into micelle and load with the anti-rheumatic drug (methotrexate, MTX). The significant higher bone mineral density in the adjuvant induced arthritis rats treated with MTX-loaded SA-Dex-OA micelles as compared to in those treated with free MTX and Dex-OA/MTX micelles may be contributed to not only the MTX prevention on bone erosion but also the effect of promoting MC3T3-E1 cell differentiation and mineralization by endogenous sialic acid [96].

Investigators, Low, *et al.* also cooperated the aspartic acid oligopeptides, which adsorb to hydroxyapatite, the mineral portion of bone, in their micelle formulation. The adsorption of this aspartic acid oligopeptides and hydroxyapatite is the strongest where bone turnover is highest or where hydroxyapatite is freshly exposed, such like in the condition of bone fracture. The biodistribution study of this aspartic acid oligopeptides containing micelle conjugated with the ^{125}I labeled anabolic agent, GSK3β Inhibitor showed a preferential accumulation of the micelle after a i.v. systemic injection to the fracture site in the murine model [97]. The improved fracture repair by this micellar drug and its branch derivative were shown in the same animal model [98].

1.5.3 Nanoparticles

Nanoparticles can be categorized as drug nanoparticles, solid nanoparticles, polymer-based nanoparticles, lipid-based nanoparticles and nanocapsules. Drug nanoparticles or so-called nanosuspension are dispersed water-insoluble drug particles in the nano-size range in an aqueous environment. Drug nanoparticles can be achieved by breaking down the bigger particles by high-pressure homogenization method or by special crystallization techniques. Polymer-based nanoparticles are commonly composed of poly(lactic acid) (PLA), poly(glycolicacid) (PGA), poly (lactic acid-co-glycolic acid) (PLGA), poly(ε-caprolactone) (PCL), and poly(methylmethacrylate) (PMMA). Chemical synthesis, salting-out, emulsification-diffusion, nanoprecipitation and freeze-drying methods are used to obtain polymer-based nanoparticles. Lipid-based nanoparticles mostly composed of fats or

waxes and can be obtained by homogenization. For certain applications, nanoparticles may be tailored into different shape, such as sphere nanoparticles [99], cube nanoparticles [100], rod-like nanoparticles [101], hollow spherical nanoparticles [102] and random shape nanoparticles. The use of the FDA approved nanoparticle drug or medical material used for the MSD conditions are mostly for the bone mimics, such like EquivaBone (Zimmer Biomet) [103], NanOss (RTI Surgical) [104], Ostim (Heraeus Kulzer) [105, 106], OsSatura (IsoTis Orthobiologics) [107], Vitoss (Stryker) [108]. These nanoparticles can provide a nanostructure with more surface area which allowed increased potential for cell attachment, and the similarity to nature bone, which increases the potential to remodel into new bone. Under the same category of nanoparticles, there are a sub-category of the nanoparticles are approved by FDA to be used as the diagnostic tool, e.g. superparamagnetic nanoparticle, Magnevist, was approved by FDA as a contrast agent for magnetic resonance imaging to facilitate the visualization of lesions with abnormal vascularity in the body [109].

1.5.4 Dendrimers.

Dendrimers are highly uniformed, branched or star-shaped macromolecules. Dendrimers can be synthesized by divergent [110] or convergent approaches [111]. They are often of uniform molecular weight and very low polydispersities. Dendrimers also have modifiable surface functional group as well as internal cavities [112]. For example, Newkome *et al*. [113] have synthesized a dendrimer containing hydrophobic interior and hydrophilic surface functionality. During or after synthesis of dendrimers, the drug molecules can be physically entrapped or

chemically conjugated to the dendrimer [114]. There are no FDA approved dendrimer drug to treat MSDs, however, researchers has put efforts on developing the bone-targeting dendrimers such as Yamamoto group has developed aspartic acid conjugated PAMAM dendrimer or alendronate conjugated PAMAM dendrimer, those dendrimers showed strong targeting effect to the bone tissue [115, 116]. When the alendronate conjugated dendrimer loaded with MTX and administrated to a bone metastasis murine model, the pharmacokinetics and therapeutic effect showed a preferential accumulation of the dendrimer to the bone tissue and a significant lower cancer cells proliferated in the metastasis site.

1.5.5 Macromolecular conjugates.

Macromolecular prodrug or polymeric conjugates which have a hydrodynamic diameter of less than 10 nm [117] may result in much less RES uptake and provide a better-controlled drug releasing profile by optimizing the covalent bond or linker between the drug and the carrier backbone. Previously, in our lab, we have developed and tested a macromolecular theranostic system that has the capacity to detect early signs of wear particle-induced peri-implant granulomatous inflammation, and in addition to deliver potent anti-inflammatory and/or anti-bone resorptive agents specifically to the peri-implant tissues with minimal “off-target” side effects. Conceptually, this system is based upon our discovery that macromolecular theranostic agents can specifically target to sites of inflammation and undergo uptake and activation by inflammatory cells [118, 119]. Besides HPMA conjugated macromolecular polymer drug, the PEGylated drug conjugates have also shown its promise in the drug delivery system development. These conjugates have a

large population in the list of the approved of FDA approved nanomedicine, among which pegloticase (Krystexxa; Savient Pharmaceuticals), FDA approved PEGylated porcine-like uricase, showed a significant decrease of plasma uric acid level in about 40% of patients suffered with chronic gout (associated with a tendency for tophi dissolution) [120]. The nanoformulation improved stability of protein through PEGylation, however, the targeting, retention and reduction immunogenic uricases of the drug still need to be developed since there were about 60% patients showed no change of their disease progression.

The great challenge for the development of the nanomedicine to treat or and diagnose the MSDs also remains a great opportunity for the researchers to develop smarter and safer drug delivery systems and diagnostics. These smarter and safer tools with the tropism to the MSD site may use different targeting strategies.

1.6 Targeting strategies

After choosing the delivery tool for drug, scientists made tremendous efforts to modify the delivery system to obtain a better targeting property to further enhance the therapeutic efficacy and reduce the off-target systemic toxicity. Fortunately, MSDs have many unique features that can help nanomedicines differentiate the disease site with normal site and benefit them with a sustained retention.

1.6.1 Passive targeting

In 1979, the antitumor protein drug neocarzinostatin (NCS) was conjugated with a synthetic copolymer of styrene maleic acid copolymer (SMA) which was

called SMANCS (molecular weight 16,000 g/mol) by Maeda [121]. This antitumor protein drug conjugate exhibited many unique properties, including prolonged half-life in circulation (20-fold), improved tumor-targeting capacity (2000 fold intra-tumor concentration than plasma), no immunogenicity and higher lipophilicity [122-124]. These properties led to the conceptualization of the Enhanced Permeability and Retention effect (EPR effect) [125]. With the advantage of EPR effect, SMANCS became the first macromolecular anticancer drug approved in 1993 in Japan [122]. The EPR effect has been observed in the applications of many nanomedicine formulations, such as polymer conjugates, polymeric micelles and liposomes [126, 127]. Most HPMA copolymers utilize the EPR effect to achieve better tumor targeting and delivery of drugs. EPR effect is a tumor vasculature-dependent phenomenon. Most tumors are well vascularized with high density and the rapid growth of blood vessels leads to irregular vascular alignment and defects of the junction between endothelial cells. The increased local fenestration of macromolecules paired with the ill-developed lymphatic drainage at the tumor lesion lead to the local accumulation of macromolecules over time [122, 128-132]. Wang et al. first described macromolecules' Extravasation through Leaky Vasculature and their subsequent Inflammatory cell-mediated Sequestration (ELVIS) [133]. It explains the passive targeting of the HPMA copolymer–dexamethasone conjugate (P-Dex) to inflammations [134, 135]. Unlike the traditional understanding of EPR effect that macromolecules only can passively target to solid tumors (not inflammation) due to the leaky vasculature and impaired lymphatic drainage, they found

although the extravasated macromolecules are cleared from the inflammatory tissue quickly, rapid internalization by inflammatory infiltrates and locally activated cells provide the mechanism for the sustained retention of the macromolecular drug conjugate at the site of inflammation.

1.6.2 Active targeting

The use of passive targeting mechanism is that researchers are taking the advantages of the nature of disease site, such like the EPR effect at tumor site and ELIVIS effect at inflammation site. Different from this smart design, researchers also utilized many active targeting strategy to target and keep the drugs at the musculoskeletal sites. Because of those unique features of the musculoskeletal system, we can design the drugs with the targeting moieties with higher affinities to those tissues.

1.6.2.1 Bone targeting

Bone system is the hardest system in the body because of the needle-like crystals composed by organic matrix and inorganic mineral phase of hydroxyapaptite (HA) [136]. Researchers choose to target the mineral composition (apatite) of the bone to obtain osteotropicity due to its biggest composition in bone and difficulties to target the organic matrix (such as the collagens which is ubiquitous in the body). There are many bone-targeting moieties can be utilized in the bone targeting drugs, including: 1. Tetracyclines have well-defined metal complexing abilities [137] and the nature of their chelation with surface calcium ions in bones [138]; 2. Pyrophosphate, bisphosphate, or alendronate can chelate the calcium ions because of their

phosphate structure [139], 3. Polymeric amino acid specific with certain sequence and abundance of the such amino acids like Asp, Glu, Gla or phosphorylated Ser/Thr can show the controlled nucleation capacity [2]. Some of those bone targeting moieties have its own cellular medical or toxicity effect, ones need to pay much attention when conjugating them to the nanomedicine or nanodiagnostics.

1.6.2.2 Tendon targeting

Unlike bone targeting, there is no many strategies for tendon targeting. However, researchers have found that the muscle cells migration has its own direction which will end at the tendon tissue. Tendon cells here are crucial in providing guidance for muscle migration by the formation of the complex between its type1 transmembrane protein, which containing a leucine-richrepeat (LRR) domain in its extracellular region, and the Robo proteins in the muscle cells. This natural cross-communication with the existing targeting mechanism behind may inspire the drug delivery scientists in designing the drug to treat tendon disease [140].

1.6.2.3 Cartilage targeting

Drugs that can be injected intra-articular still face to another challenge that it is difficult to have enough drug penetrating into the cartilage tissue and reach the cell and matrix tissue. This is not only because of the highly charged oligosaccharides introducing an effective polar barrier for penetration of lipophilic drug molecules, but also an intrinsic challenge results from the fact that low-molecular-weight solutes in the joint will be eliminated due to the convective transport and lymphatic uptake. Researchers have investigated using the addition of cationic domains or

proteins that favorable bind-to heparan sulfate or the glycosaminoglycan binding domain to obtain the longer retention at the intra-articular site and deeper penetration to the chondrocytes using the drug delivery carrier.

While the large amount of unmet medical needs of the drugs for the treatment and diagnosis of the musculoskeletal diseases remained, the nature of those types of diseases also provide the unique opportunities for the development and optimization of the targeted drug delivery system. In the following chapters, we will introduce our work on development of macromolecular prodrug conjugates for the diagnosis and treatment of musculoskeletal diseases.

CHAPTER 2

DESIGN, SYNTHESIS AND CHARACTERIZATION OF MACROMOLECULAR PRODRUG WITH DIFFERENT MOLECULAR WEIGHT, DRUG COTENT, AND DRUG-CONTAINING MONOMER

2.1 Introduction

As discussed in Chapter 1, to meet the clinical need for the treatment and early detection of the implant lossening, we have explored the potential utility of N-(2-hydroxypropyl) methacrylamide (HPMA) copolymer conjugates as a theranostic platform for early diagnosis and prophylactic treatment of peri-prosthetic osteolysis. [118, 141]. Because of the nature of this synthetic, water-soluble polymer-based theranostic platform, structural parameters (such as average molecular weight (MW), drug loading, and the presence of active targeting ligands) are all known to have significant impact on the platform's in vivo pharmacokinetic and biodistribution (PK/BD) profile. In addition, the pathophysiology features (e.g., inflammation) may have a profound impact on the platform's in vivo fate. HPMA copolymer conjugates' PK/BD profiles have been characterized in multiple animal models of human diseases. [142-144] In this chapter, we will focus on synthesizing a series of HPMA copolymers with different molecular weight (MW) and/or Dex contents which were labeled using Alexa Flour® 488, IRDye 800 CW, and radio isotope ^{125}I respectively for the following *in vitro* and *in vivo* evaluation (Figure 2. 1); and HPMA copolymers with different Dex containing monomer (Figure 2. 2) to provide different releasing rates for the *in vitro* releasing characterization and *in vivo* therapeutic investigation.

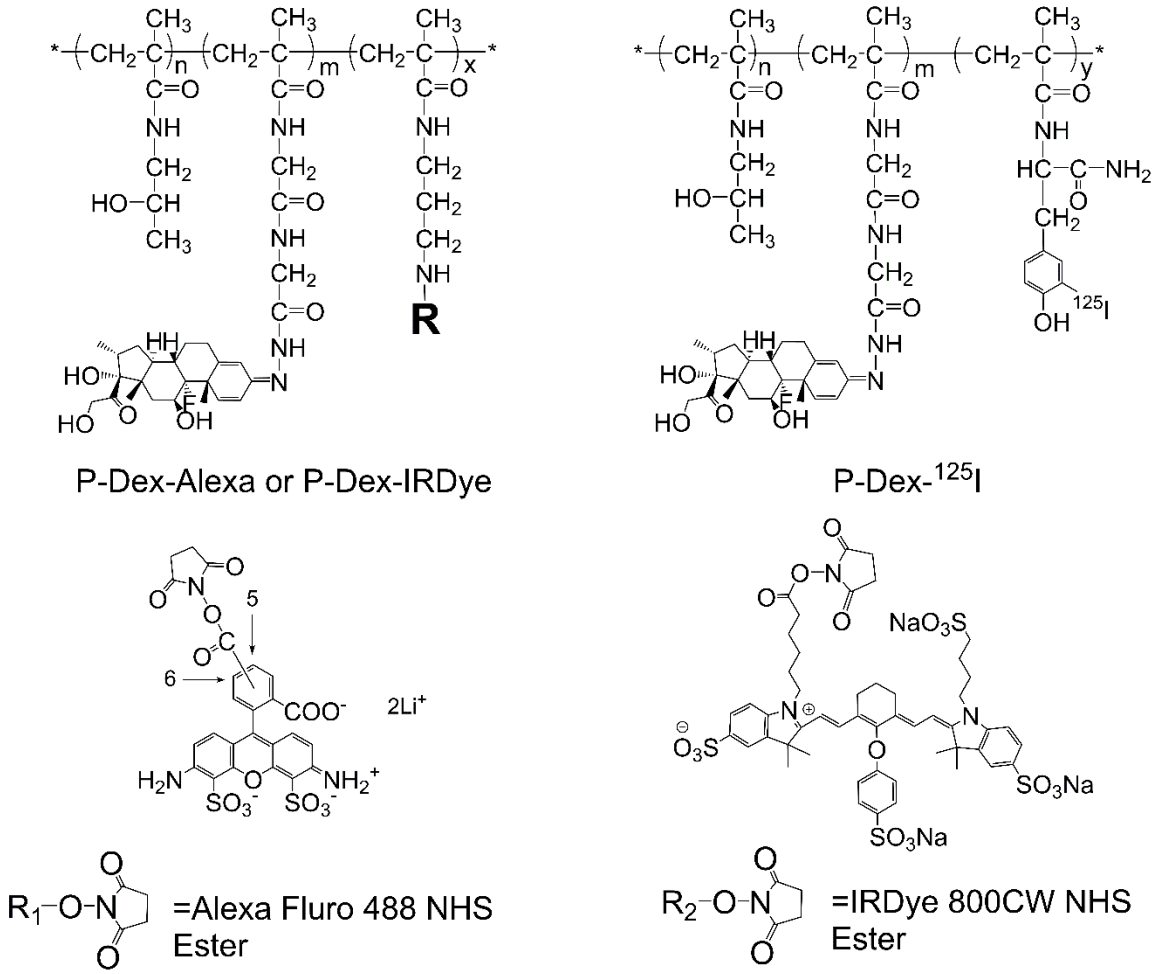

Figure 2. 1 General structure of the HPMA copolymer conjugates.

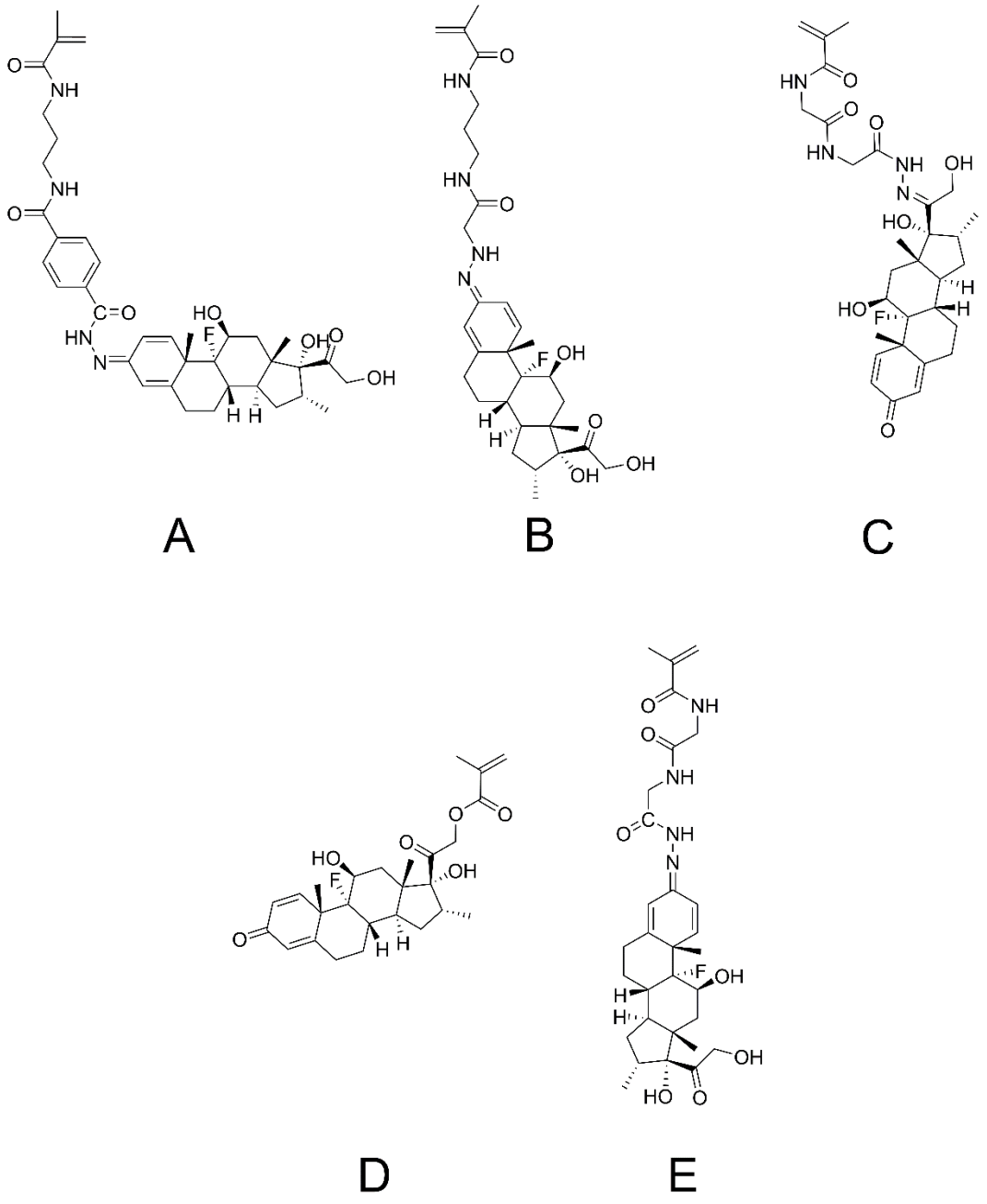

Figure 2. 2 Chemical structure of different Dex containing monomer.

2.2 Materials and Methods

2.2.1 Materials

N-(2-Hydroxypropyl) methacrylamide (HPMA), N-methacryloyl glycylglycyl hydrazinyl dexamethasone (MA-Dex), *N*-methacryloyl tyrosine amide (MA-Tyr-NH_2), and *S,S′*-bis(*α,α′*-dimethyl-*α″*-acetic acid)-trithiocarbonate (CTA, purity >97%) were prepared as reported previously [145]. Sephadex LH-20 resin and PD-10 columns were obtained from GE HealthCare (Piscataway, NJ). The $Na^{125}I$ was purchased from PerkinElmer (Waltham, MA). IRDye 800CW NHS ester was purchased from LI-COR, Inc. (Lincoln, NE). Alexa Fluor® 488 NHS ester was purchased from Life Technologies (Eugene, OR). All other reagents and solvents were purchased from either Sigma-Aldrich (St. Louis, MO) or Acros Organics (Morris Plains, NJ). All compounds were reagent grade or higher and used without further purification.

2.2.2 Instruments

^{1}H and ^{13}C NMR spectra were recorded on a 500 MHz NMR spectrometer (Varian, Palo Alto, CA). A lambda 10 UV/vis Spectrometer (PerkinElmer, Waltham, MA) was used for UV/vis spectrophotometric analyses. A ÄKTA Fast Protein Liquid Chromatography system (FPLC, GE Healthcare Bio-Sciences, Pittsburgh, PA) equipped with Superdex 200 column, UV, and RI (KNAUER, Berlin, Germany) detectors was used for analyses of P-Dex molecular weight. HPLC analyses were performed on an Agilent 1100 HPLC system (Agilent Technologies, Inc., Santa Clara, CA) with a reverse phase C18 column (Agilent, 4.6 × 250 mm, 5 μm).

Zetasizer Nano ZS90 (Malvern, Worcestershire, UK) was used in P-Dex aggregation analyses.

2.2.3 Synthesis of the macromolecular prodrugs with different molecular weight and drug content

The HPMA copolymer-dexamethasone conjugates were synthesized by a reversible addition−fragmentation chain transfer (RAFT) copolymerization as described previously [146]. *N*-(2-Hydroxypropyl) methacrylamide (HPMA), *N*-methacryloyl glycylglycyl hydrazinyl dexamethasone (MA-Dex), and *N*-methacryloyl tyrosine amide (MA-Tyr-NH_2) were dissolved in anhydrous methanol and then copolymerized under argon at 45 °C for 48 h with 2,2″-azobis(isobutyronitrile) (AIBN) as an initiator and *S,S′*-bis(*α,α′*-dimethyl-*α″*-acetic acid) trithiocarbonate (CTA) as the RAFT agent. The ratio of AIBN and CTA was adjusted to obtain HPMA copolymer-dexamethasone conjugates (P-Dex) with different molecular weight, and the dexamethasone (Dex) content was regulated by adjusting the MA-Dex feed-in ratio (Table 2. 1). The final tyrosine amide-containing HPMA copolymer-Dex conjugates (P-Dex-Tyr-NH_2) were obtained by lyophilization after the removal of the unreacted low molecular weight compounds using LH-20 column.

P-Dex-15 kDa-12%				
	Molar ratio (%)	Mw (g/mol)	mmol	mg
HPMA	89.84	143.20	2.7933	400.00
MA-Dex	6.41	588.70	0.1992	117.26
AIBN	1.78	168.75	0.0554	9.35
CTA	0.99	264.70	0.0308	8.14
APMA	0.99	178.57	0.0306	5.47
METHANOL	3.74 mL			
P-Dex-25 kDa-12%				
	Molar ratio (%)	Mw (g/mol)	mmol	mg
HPMA	91.05	143.20	2.7933	400.00
MA-Dex	6.49	588.70	0.1992	117.26
AIBN	0.94	168.75	0.0288	4.86
CTA	0.52	264.70	0.0160	4.24
APMA	1.00	178.57	0.0306	5.47
METHANOL	3.74 mL			
P-Dex-35 kDa-12%				
	Molar ratio (%)	Mw (g/mol)	mmol	mg
HPMA	91.48	143.20	2.7933	400.00
MA-Dex	6.48	588.70	0.1979	116.49
AIBN	0.67	168.75	0.0206	3.47
CTA	0.37	264.70	0.0114	3.03

APMA	1.00	178.57	0.0304	5.44
METHANOL	3.74 mL			
P-Dex-45 kDa-12%				
	Molar ratio (%)	Mw (g/mol)	mmol	mg
HPMA	91.64	143.20	2.7933	400.00
MA-Dex	6.49	588.70	0.1979	116.49
AIBN	0.56	168.75	0.0171	2.89
CTA	0.31	264.70	0.0095	2.52
APMA	1.00	178.57	0.0304	5.44
METHANOL	3.74 mL			
P-Dex-20 kDa-12%				
	Molar ratio (%)	Mw (g/mol)	mmol	mg
HPMA	89.40	143.20	2.7933	400.00
MA-Dex	6.50	588.70	0.2031	119.57
AIBN	2.00	168.75	0.0623	10.24
CTA	1.11	264.70	0.0346	9.78
MA-Tyr-NH_2	1.00	248.30	0.0312	7.76
METHANOL	3.74 mL			
P-Dex-30 kDa-12%				
	Molar ratio (%)	Mw (g/mol)	mmol	mg
HPMA	90.93	143.20	2.7933	400.00
MA-Dex	6.50	588.70	0.1997	117.55

AIBN	1.01	168.75	0.0311	5.10
CTA	0.56	264.70	0.0173	4.87
APMA	1.00	248.30	0.0307	7.63
METHANOL	3.74 mL			
P-Dex-40 kDa-12%				
	Molar ratio (%)	Mw (g/mol)	mmol	mg
HPMA	91.45	143.20	2.7933	400.00
MA-Dex	6.50	588.70	0.1985	116.88
AIBN	0.68	168.75	0.0207	3.40
CTA	0.38	264.70	0.0115	3.24
MA-Tyr-NH_2	1.00	248.30	0.0305	7.58
METHANOL	3.74 mL			
P-Dex-30 kDa-6%				
	Molar ratio (%)	Mw (g/mol)	mmol	mg
HPMA	94.31	143.20	3.4916	500.00
MA-Dex	3.25	588.70	0.1203	70.83
AIBN	0.93	168.75	0.0343	5.62
CTA	0.51	264.70	0.0190	5.37
APMA	1.00	248.30	0.0370	9.19
METHANOL	4.15 mL			
P-Dex-30 kDa-0%				
	Molar ratio (%)	Mw (g/mol)	mmol	mg

HPMA	97.69	143.20	3.4916	500.00
MA-Dex	0.00	588.70	0.0000	0.00
AIBN	0.84	168.75	0.0300	4.93
CTA	0.47	264.70	0.0167	4.66
APMA	1.00	248.30	0.0357	8.87
METHANOL	4.15 mL			

Table 2. 1 Feed-in ratio of the AIBN, CTA, HPMA and MA-Dex, was adjusted to obtain HPMA copolymer-dexamethasone conjugates (P-Dex) with different molecular weight, and the dexamethasone (Dex) content.

2.2.4 Synthesis of ^{125}I labeled P-Dex (P-Dex-^{125}I)

To label the P-Dex-Tyr-NH_2 with ^{125}I, the tyrosine containing copolymers (~1 mg) were dissolved in saline (50 μL, 0.9%) in a glass vial (1 mL). Chloramine-T (100 μL, 4.8 mg/mL, saline) and NaI^{125} solution (pH = 12, 20 μL, 1 mCi) were sequentially added to the solution. This reaction was stirred at room temperature (0.5 h) and quenched by $Na_2S_2O_3$ (6 mg/mL, in 100 μL saline). After purification by PD-10 column, twice, the resulting solution (1.5 mL) was obtained with strong radioactivity (~0.08−0.12 mCi). The entire labeling process was done according to a protocol approved by the University of Nebraska Medical Center Radiation Safety Office in a fume hood with face velocity of 100 FPM and with lead shield protection. Post labeling cleaning and contamination survey were performed to ensure the absence of any radiation contamination in the working area.

2.2.5 Synthesis of IRDye 800CW-labeled P-Dex (P-Dex-IRDye)

P-Dex-APMA (the copolymers of HPMA and *N*-(3-aminopropyl) methacrylamide,10 50 mg, containing ~0.0037 mmol of amine) and IRDye 800CW NHS ester (1.25 mg, 0.001075 mmol LI-COR Biosciences, Lincoln, NE) were dissolved in dimethylformamide (DMF, 900 μL) with 15 μL of *N,N*-diisopropylethylamine (DIPEA) added. The solution was stirred overnight in darkness at room temperature. The product was then purified on an LH-20 column and lyophilized. The IRDye 800CW content was determined using Lambda 10 UV/vis Spectrometer.

2.2.6 Synthesis of Alexa Fluor® 488 labeled P-Dex (P-Dex-Alexa)

P-Dex-APMA (50.0 mg, containing ~0.0037 mmol of amine) and Alexa Fluor 488 NHS ester (0.75 mg, 0.001 mmol, Life Technologies, Eugene, OR) dissolved in DMF (900 μL) with DIPEA (15 μL) added. The mixture was stirred overnight in darkness at room temperature. The product was then purified on an LH-20 column and lyophilized. The Alexa Fluor 488 content was determined using a Lambda 10 UV/vis Spectrometer.

2.2.7 Synthesis of HPMA copolymer conjugates with different Dex-containing monomer (P-Dex-A, P-Dex-B, P-Dex-C, P-Dex-D)

2.2.7.1 Synthesis of Monomer A

As shown in Figure 2.3,dexamethasone and imidazole were dissolved in anhydrous DMF and the solution was cooled to 0 °C by ice bath. TBSCl was added. The solution was stirred at 0 °C for 1h and then allowed to room temperature for 3h. Ethyl acetate (200 ml) was added and the solution was then washed with saturated brine. The organic phase was then dried over Na_2SO_4 and then the solvent was removed to get crude product 1.

The crude product was then dissolved in a solution of hydrazine monohydrate in methanol, and then acetic acid was added. The solution was stirred at room temperature for 4h. Ethyl acetate was added and the solution was then washed with saturated brine. The organic phase was then dried over Na_2SO_4 and then the solvent was removed to get the residue. Flash column chromatography to give product 2. Some compound 1 was recovered.

N-(3-aminopropyl)methacrylamide hydrochloride and Et_3N were dissolved in anhydrous DMF at 0 °C. Mono-methyl terephthalate and DCC were then added. The solution was stirred at room temperature for 6h. Ethyl acetate was added and the solution was then washed with saturated brine. The organic phase was then dried over Na_2SO_4 and then the solvent was removed. The residue was purified by column chromatography to give product 3.

Compound 3 was dissolved in a mixture of water and methanol, KOH was then added. The solution was stirred at room temperature overnight. HCl solution was added to neutralize the KOH. Ethyl acetate was used to extract the product from the aqueous phase. Then the solvent was removed, the residue was purified by flash chromatography to give the product 4.

Compound 2, DCC, HOBt and DIPEA were dissolved in anhydrous DMF, then compound 4 was added. The solution was stirred at room temperature 3h. Ethyl acetate was added and the solution was then washed with saturated brine. The organic phase was then dried over Na_2SO_4 and then the solvent was removed. The residue was purified by column chromatography to give product 5.

Compound 5 was dissolved in THF and TBAF (1M, THF) was added. The solution was stirred at room temperature for 1h. Ethyl acetate was added and the solution was then washed with saturated brine. The organic phase was then dried over Na_2SO_4 and then the solvent was removed. The residue was purified by column chromatography to give product 6 (Monomer A).

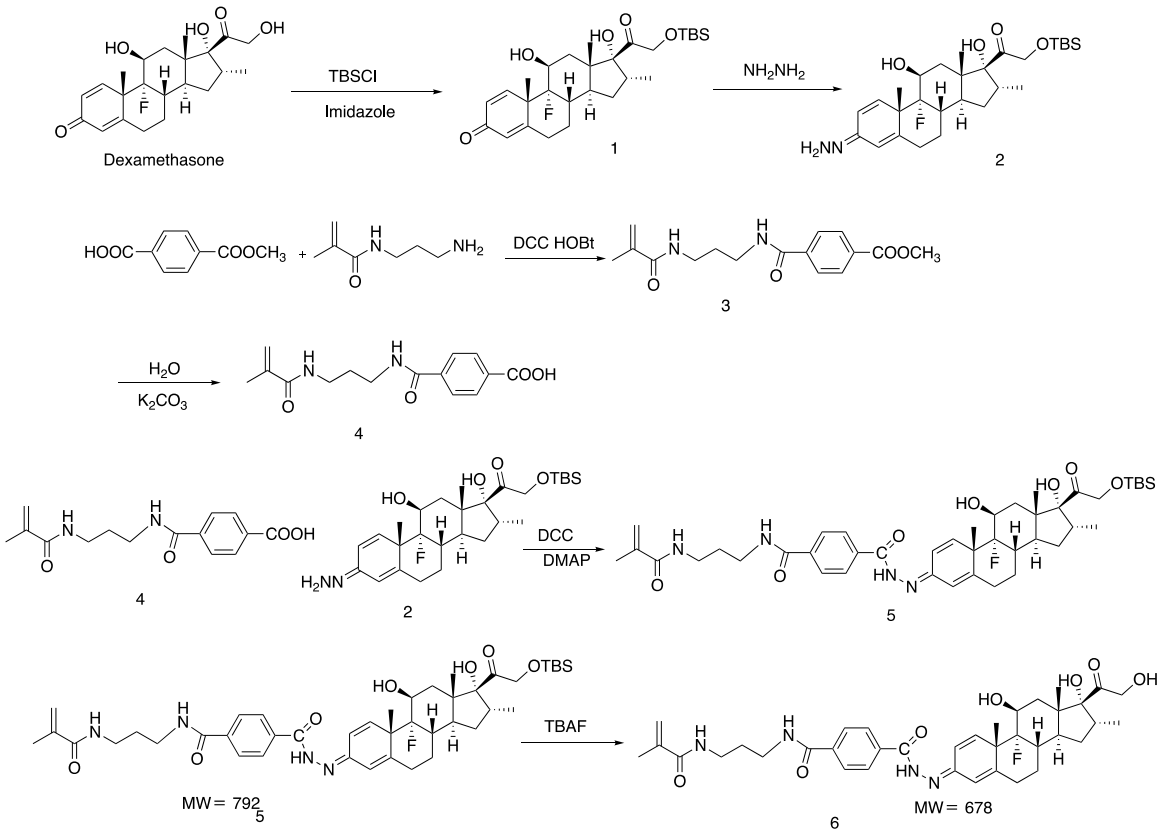

Figure 2.3 Synthesis route of Monomer A.

2.2.7.2 Synthesis of Monomer B

As shown in Figure 2.4 compound 2 and methyl bromoacetate were dissolved in anhydrous DMF, potassium carbonate was then added to the solution. The solution was heated to 80°C for 2h. Ethyl acetate was added and the solution was then washed with saturated brine. The organic phase was then dried over Na_2SO_4 and then the solvent was removed. The residue was purified by column chromatography to give product 7.

Compound 7 and 1,3-diaminopropane were dissolved in MeOH. The solution was stirred at room temperature overnight. Ethyl acetate was added and the solution was then washed with saturated brine. The organic phase was then dried over Na_2SO_4 and then the solvent was removed to give the crude product 8.

The crude compound 8 and triethylamine were dissolved in dichloromethane. The solution was then cooled to 0°C with ice-water bath. The methacryl chloride in dichloromethane was added dropwise. After addition, the solution was then stirred 1 hour at 0°C for 1h. Ethyl acetate was added and the solution was then washed with saturated brine. The organic phase was then dried over Na_2SO_4 and then the solvent was removed. The residue was purified by column chromatography to give product 9.

Compound 9 was dissolved in THF and TBAF (1M, THF) was added. The solution was stirred at room temperature for 1h. Ethyl acetate was added and the solution was then washed with saturated brine. The organic phase was then dried

over Na_2SO_4 and then the solvent was removed. The residue was purified by column chromatography to give product 10 (Monomer B).

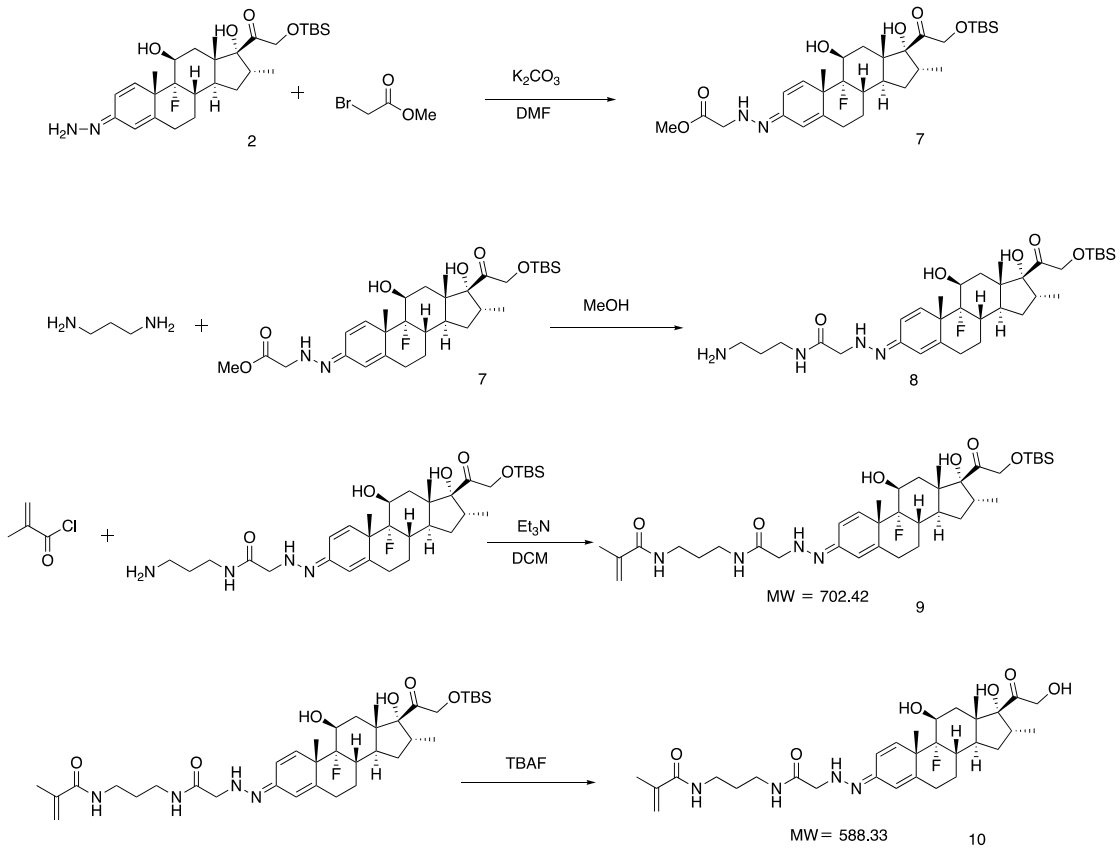

Figure 2. 4 Synthesis route of Monomer B

2.2.7.3 Synthesis of Monomer C

As shown in Figure 2.5, the isomer of compound 2 is a byproduct of the reaction of preparing compound 2. It was dissolved in anhydrous DMF with DCC. The solution was cooled to 0°C with ice-water bath and then added MA-Gly-Gly-OH and DMAP. The solution was stirred at 0°C for 3h. Ethyl acetate was added and the solution was then washed with saturated brine. The organic phase was then dried over Na_2SO_4 and then the solvent was removed. The residue was purified by column chromatography to give product 11.

Compound 11 was dissolved in THF and TBAF (1M, THF) was added. The solution was stirred at room temperature for 1h. Ethyl acetate was added and the solution was then washed with saturated brine. The organic phase was then dried over Na_2SO_4 and then the solvent was removed. The residue was purified by column chromatography to give product 12 (Monomer C).

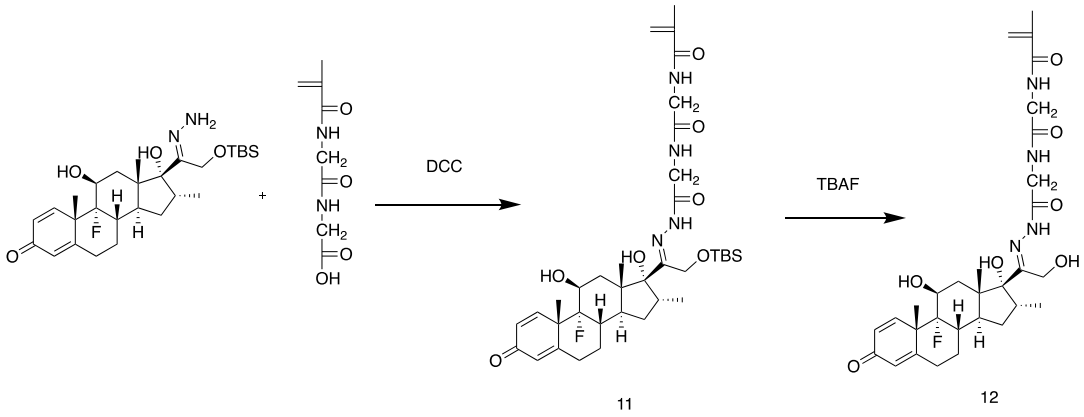

Figure 2. 5 Synthesis route of Monomer C

2.2.7.4 Synthesis of Monomer D

To get Monomer D, dexamethasone, DMAP and triethylamine were dissolved in anhydrous dichloromethane. The solution was cooled to 0°C with ice-water bath and then methacryl chloride in dichloromethane was added dropwise. The solution was then stirred 1 hour at 0°C for 1h. Ethyl acetate was added and the solution was then washed with saturated brine. The organic phase was dried over Na_2SO_4 and the solvent was removed. The residue was purified by column chromatography to give product 13 (Monomer D, shown in Figure 2.6).

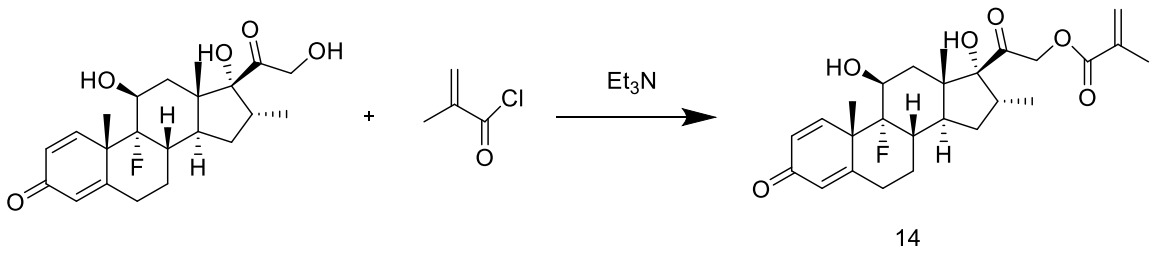

14

Figure 2. 6 Synthesis route of Monomer D

2.2.8 Characterization of the HPMA copolymer conjugates

Size exclusion chromatography (SEC) with an ÄKTA fast protein liquid chromatography (FPLC) system was used to determine the number-average molecular weight (Mn), weight-average molecular weight (Mw), and the polydispersity index (PDI) of the copolymers using a calibration of HPMA homopolymers with narrow PDI. To quantify Dex content in P-Dex, the copolymers were hydrolyzed in 0.1 N HCl (1 mg/ mL) overnight. The resulting solution was neutralized and analyzed on an Agilent 1100 high performance liquid chromatography (HPLC) system with a reverse phase C18 column (Agilent, 4.6 × 250 mm, 5 μm). Mobile phase, acetonitrile/water 2:3; detection, UV 240 nm; flow rate, 1 mL/ min; injection volume, 10 μL. The analyses were performed in triplicate. The mean value and standard deviation were obtained using Excel. The characterizations of all HPMA copolymer conjugates used in this study are summarized in Tables 2.2 and 2.3. The potential aggregation of the P-Dex (6 wt%) was characterized by DLS with a series of concentrations. Three measurements at each concentration were performed, and the results were averaged and summarized in Table 2.5.

The Dex content analysis of the HPMA copolymer with different Dex-containing monomers is as similar as described above. The weight average molecular weight (Mw), number of molecular weight (Mn) polydispersity (PDI) and Rayleigh Ratio (RΘ, dn/dc) of the P-Dex-A, P-Dex-B, P-Dex-C, and P-Dex-D were analyzed using a combination of AKTÄ pure FPLC system, Wyatt multiangle light scattering system and Optilab T-rEX refractive index concentration detector. In vitro releasing profile of the P-Dex (for a clear comparison, we named P-Dex as P-Dex-E in all

the following study related with the different releasing rate polymers evaluation), P-Dex-A, P-Dex-B, P-Dex-C, and P-Dex-D was conducted in different pH buffered solution (pH 5.0 acetate buffer, pH 6.0 acetate buffer, pH 7.0, pH7.4 and pH 8.7 phosphate buffer, pH 11 sodium carbonate buffer, human serum and rat serum). The copolymers were weighted and dissolved in to different buffer to the concentration of 4 mg/mL (polymer/solution) with Pluronic F127 (1 wt% of total Dex) added to create the “sink” condition. The copolymer-containing solutions were then fixed into a shaking incubator (60 r/min) at 37 °C. At pre-designed time points, the releasing solutions were withdrawn, neutralized and then extracted with 9 times in volume of METB. The 1/3 volume of METB was then withdrawn and evaporated using vacuum evaporator. (eg. 50 uL samples released in pH 4.5 solution was withdrawn and neutralized using 6.5 uL pH 10 solution. Then 508.5 uL METB was added for extraction and 169.5 uL METB supernatant was withdrawn followed with the solvent evaporated using vacuum evaporator. The residues were resuspended into 100 uL H_2O/MeOH solution (H_2O/MeOH=1:9) for HPLC injection). The HPLC analyses was based on the standard curve using dexamethasone base under the same flowing condition to determine the free Dex concentration. The METB extraction recovery rate was analyzed using the same method in the *in vitro* releasing part within the Dex concentration from 5-500 μg/mL.

2.3 Results

2.3.1 Characterization of HPMA copolymer conjugates

The synthesis of all the HPMA copolymer-dexamethasone conjugates and their labeling with ^{125}I and fluorescent labels were straightforward [146]. By employing

RAFT copolymerization, we were able to control the MW of the HPMA copolymer conjugates and manage their PDI in a narrow range as shown in Tables 2.2 and 2.3. The dynamic light scattering analysis results of P-Dex copolymers with different MW and Dex content were presented in Table 2.4 and results for P-Dex-35 kDa-6% at different concentration can be seen in Table 2.5. The DLS data clearly suggest that P-Dex-35 kDa-6% forms aggregates under the conditions tested. This finding may partially explain the unexpected fast clearance of P-Dex-35 kDa-6% found in the PK/BD study.

The HPMA copolymer conjugates with different monomers were characterized as described above. The results shown in Table 2.6 represented the MW and PDI of the polymers were as designed. The relatively low drug content in the P-Dex-B may be the result of the potential releasing of the Dex from the fast releasing monomer B during the polymerization.

Polymer conjugates	***M_w*** (× 10^3 g/mol)	**PDI**	**Dex content** (μmol/g)	**Radioactivity** (μCi/g)
P-Dex-20 kDa-12%	20.5	1.11	283.09 ± 35.16	138.8
P-Dex-30 kDa-12%	30.7	1.18	346.28 ± 10.70	394.8
P-Dex-40 kDa-12%	39.1	1.21	341.94 ± 25.98	354.8
P-Dex-30 kDa-6%	35.3	1.17	170.46 ± 22.42	200.4
P-Dex-30 kDa-0%	30.8	1.06	0	180.8

Table 2.2 The characterization of HPMA copolymer conjugates labeled with ^{125}I. M_w: weight average molecular weight; PDI: polydispersity index.

Polymer conjugates	**Mw** ($\times 10^3$ g/mol)	**PDI**	**Dex Content** (μmol/g)	**[Alexa 488]** (μmol/g)	**[IRDye 800CW]** (μmol/g)
P-Dex-15 kDa-12%	15.9	1.35	306.55 ± 27.24	10.89 ± 0.15	6.20 ± 0.14
P-Dex-25 kDa-12%	27.5	1.4	300.13 ± 11.23	13.82 ± 0.27	6.08 ± 0.31
P-Dex-35 kDa-12%	35.3	1.49	356.34 ± 39.55	10.25 ± 0.20	7.89 ± 0.04
P-Dex-45 kDa-12%	45.3	1.34	315.32 ± 18.40	12.63 ± 1.28	7.55 ± 0.14
P-Dex-35 kDa-6%	35.7	1.29	168.86 ± 20.33	11.83 ± 0.38	7.54 ± 0.10
P-Dex-35 kDa-0%	36.0	1.45	0	13.50 ± 0.30	7.83 ± 0.11

Table 2.3 The characterization of HPMA copolymer conjugates labeled with fluorescent probes. Mw: weight average molecular weight; PDI: polydispersity index; Dexamethasone content; [Alexa-488]: Alexa Fluor® 488 content; [IRDye-800CW]: IRDye 800CW content.

Sample Name	P-Dex-15 kDa-12%	P-Dex-35 kDa-12%	P-Dex-45 kDa-12%	P-Dex-35 kDa-6%	P-Dex-35 kDa-0%
Z-Ave (d.nm)	6.643	7.673	8.552	163.9	6.828
PDI	0.237	0.318	0.209	0.481	0.174

Table 2.4 Result of dynamic light scattering characterization of polymers at a concentration of 5 mg/mL. Z-Ave: Z-Average size (diameter.nm); PDI: Polydispersity index.

Concentration (mg/mL)	**5**	**37.5**	**150**
Z-Ave (d.nm)	163.9	282.9	313.6
PDI	0.481	0.769	1

Table 2.5 Result of dynamic light scattering characterization of P-Dex-35 kDa-6% at different concentration. Z-Ave: Z-Average size (diameter. nm); PDI: Polydispersity index.

Polymer conjugates	**Mw** ($\times 10^3$ g/mol)	**PDI**	**Dex Content** (μmol/g)
P-Dex-A	35.8	1.32	329.76 ± 8.80
P-Dex-B	36.7	1.36	113.61 ± 13.19
P-Dex-C	35.4	1.13	418.27 ± 12.63
P-Dex-D	31.9	1.48	303.66 ± 9.22
P-Dex-E	39.1	1.23	258.11 ± 6.40

Table 2.6 The characterization of HPMA copolymer conjugates conjugated with different Dex-containing monomers. M_w: weight average molecular weight; PDI: polydispersity index.

2.3.2 In Vitro release profile of the P-Dex-A, P-Dex-B, P-Dex-C, P-Dex-D, P-Dex-E in different releasing buffer

The in vitro Dex release was studied by incubating P-Dex-A, P-Dex-B, P-Dex-C, P-Dex-D, P-Dex-E in pH 5.0, pH 6.0, pH 7.0, pH 7.4, pH 8.7, pH 11.0, human serum and rat serum at 37°C (Figure 2.7). The polymers all showed different releasing rates in different buffers. When comparing the rates under the same buffer, different polymers released with differently rates. The releasing rates sequence also changed when the buffer changed (Figure 2.8). For example, under acidic condition, pH 4.5 and pH 5.5, the releasing rate trend was $R_{P\text{-}Dex\text{-}B} > R_{P\text{-}Dex\text{-}C} > R_{P\text{-}Dex\text{-}D} > R_{P\text{-}Dex\text{-}E} > R_{P\text{-}Dex\text{-}A}$. Under biological PBS buffer (pH 7.4) the releasing rate trend was $R_{P\text{-}Dex\text{-}D} > R_{P\text{-}Dex\text{-}B} > R_{P\text{-}Dex\text{-}C} > R_{P\text{-}Dex} > R_{P\text{-}Dex\text{-}A}$. Under basic condition (pH 10), considering the self-degradation of Dex, the releasing rate trend in the first 3 days was used to compare: $R_{P\text{-}Dex\text{-}D} > R_{P\text{-}Dex\text{-}C} > R_{P\text{-}Dex\text{-}B} > R_{P\text{-}Dex\text{-}A} > R_{P\text{-}Dex}$. The recovery rate was 97.18 ± 2.6%

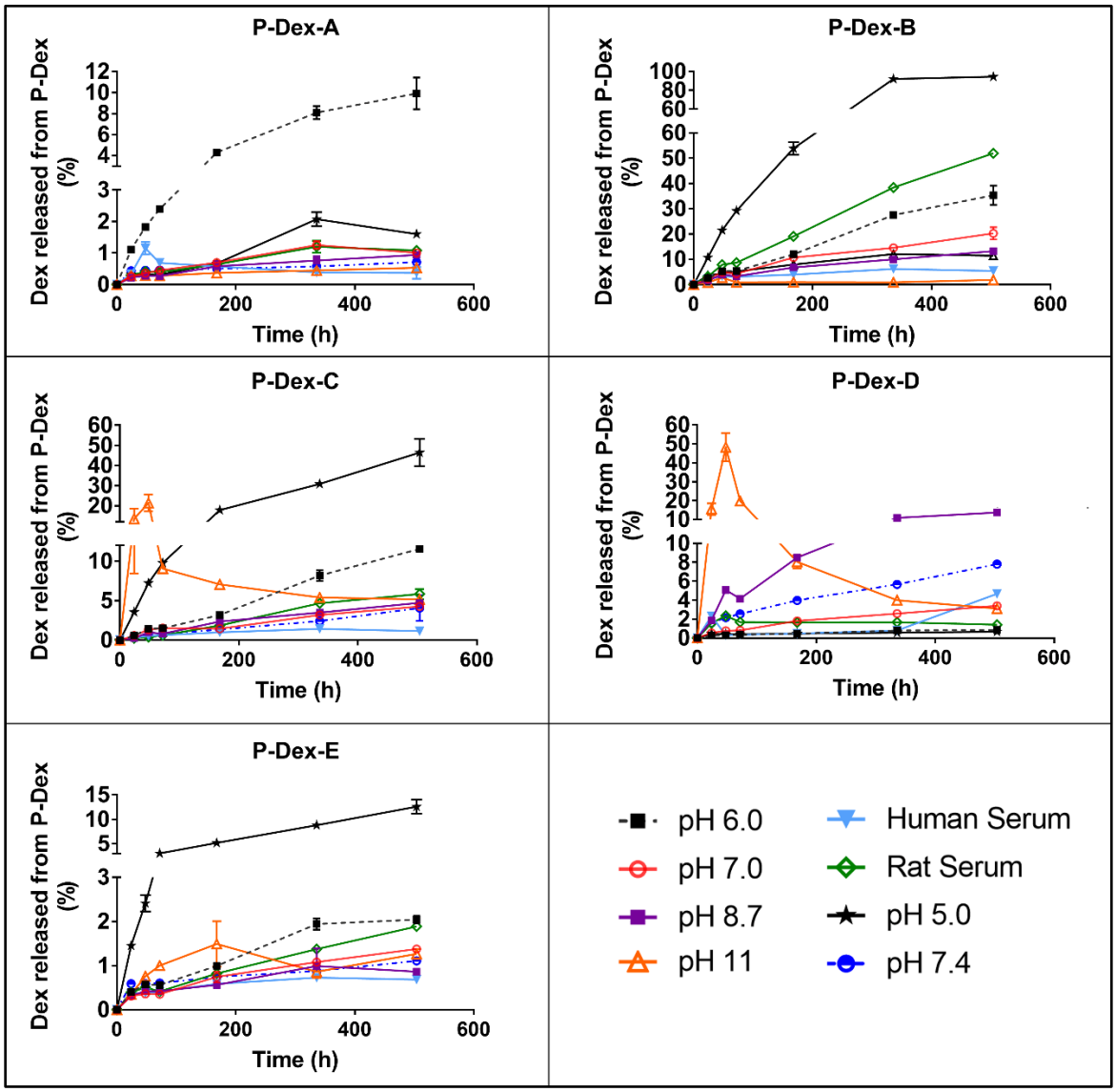

Figure 2.7 In Vitro Dex release from P-Dex P-Dex-A, P-Dex-B, P-Dex-C, P-Dex-D, P-Dex-E. The polymers showed different releasing rates under different pH. Each sample was measured three times. The mean values and standard deviation were calculated using GraphPad Prism 7.

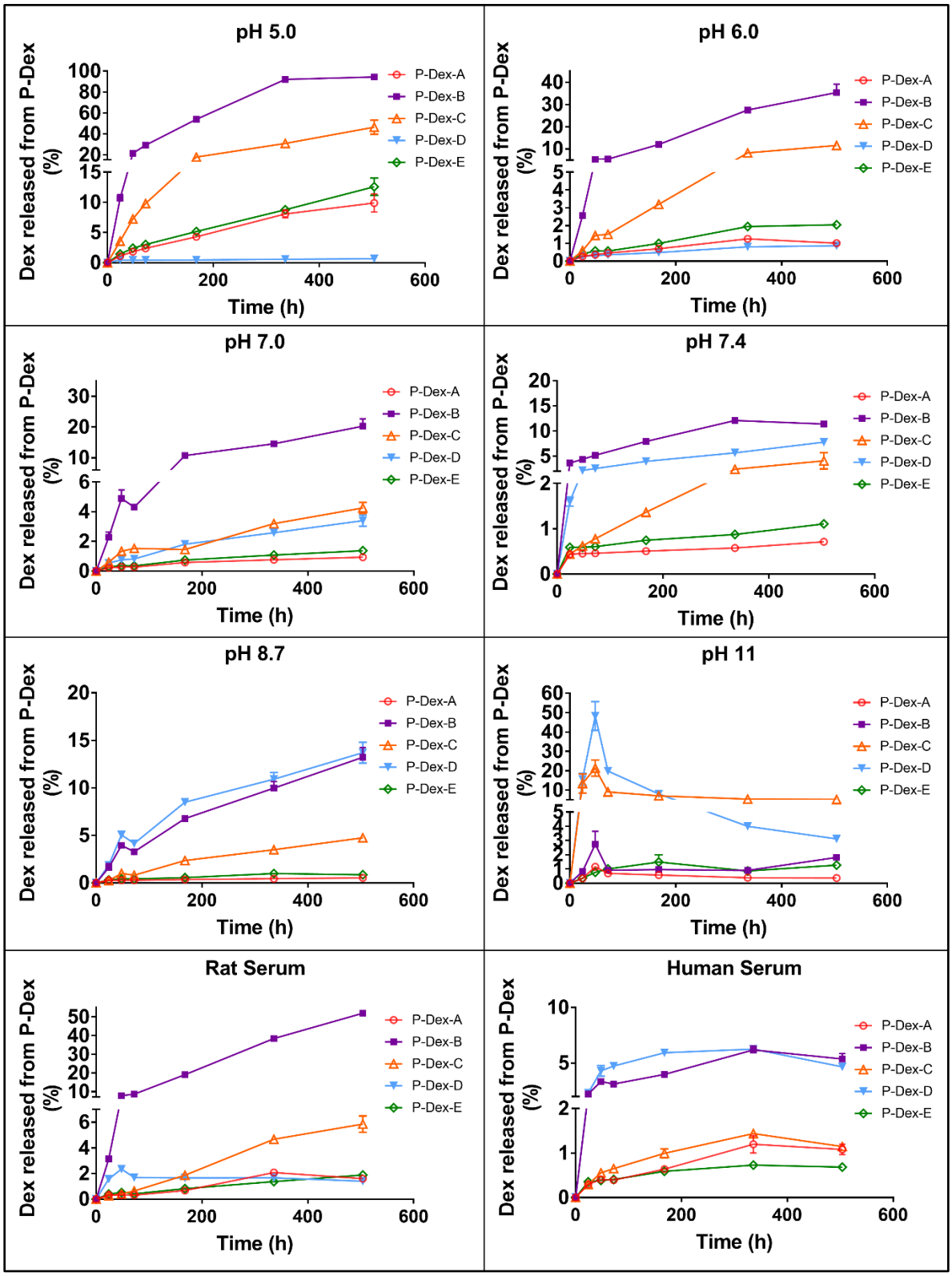
pH 5.0
pH 6.0
pH 7.0
pH 7.4
pH 8.7
pH 11
Rat Serum
Human Serum
Dex released from P-Dex (%)
Time (h)
P-Dex-A
P-Dex-B
P-Dex-C
P-Dex-D
P-Dex-E

Figure 2.8 *In Vitro* Dex release from P-Dex P-Dex-A, P-Dex-B, P-Dex-C, P-Dex-D, P-Dex-E at different releasing solution (pH=5.0, 6.5, 7.0, 7.4, 8.7 and 11, human serum and rat serum). Each sample was measured three times. The mean values and standard deviation were calculated using GraphPad Prism 7.

2.4 Discussion

The passive targeting of nanomedicines, including water-soluble macromolecules after systemic administration, has been validated in multiple animal models of inflammatory diseases, which encompass chronic systemic autoimmune disorders (e.g., rheumatoid arthritis, systemic lupus), acute local injuries (e.g., fracture), and chronic local inflammatory conditions (e.g., peri-implant osteolysis) [119, 146-148]. We posited that the mechanism for this passive targeting is different from the enhanced permeability and retention (EPR) effect [149] and may be explained by an ELVIS mechanism (Extravasation through Leaky Vasculature and Inflammatory cell-mediated Sequestration) [134, 150, 151], in which the systemically administered nanomedicine would extravasate through the leaky vasculature at the inflammatory lesion and be sequestered locally via inflammatory cell infiltrates and activated resident cell. Concurrently, for systemic inflammatory conditions, a fraction of the nanomedicine administered may also be sequestered by white blood cells (WBC) in the circulation and be actively transported to the inflammatory lesion. Previously, we have found that the HPMA copolymers' structural parameters, such as average MW and drug loading, have a significant impact on their pharmacokinetic and biodistribution (PK/BD) profile in a systemic inflammatory arthritis rat model[144]. The focus of this and the next chapter, therefore, is to define the impact of MW and drug loading on PK/BD profile of HPMA copolymer-dexamethasone conjugates in a model of localized inflammation. For this purpose, we synthesized a series of HPMA copolymers with different MW or Dex content as described above. Using both ^{125}I-labeling/gamma counter techniques and the NIR

optical imaging, we would validate the impact of MW and Dex content on the PK/BD profiles of HPMA copolymers in the mouse model of aseptic implant loosening in the following chapter.

Besides molecular weight and drug content, the chemical structure of the Dex containing monomer will also affect the conjugates' pharmacokinetics since it will affect the drug releasing property. To better understand the influence of the polymer properties on the biology system, and to further instruct the future drug development, the designation and synthesis of polymers with different Dex containing polymers were of high value. With a low drug loading of the P-Dex-B, it was excluded from the in vivo evaluation, with the consideration of the drug content shall be similar when comparing with the other polymers to avoid multiple factors in the same experiment. The results from *in vivo* therapeutic of those different monomers containing polymers would be compared in this chapter and following chapters.

2.5 Conclusion

In this chapter, we designed and synthesized a series of the HPMA copolymers with different structural parameters. The HPMA copolymers with different molecular weight (MW) and/or Dex contents were labeled using Alexa Flour® 488, IRDye 800 CW, and radio isotope ^{125}I respectively. Different Dex containing monomers were designed, synthesized and polymerized with HPMA to form different HPMA-Dex-copolymers with different Dex releasing rates. The conjugates were characterized for their molecular weight, polydispersity, labeling content, and *in vitro* releasing rate.

CHAPTER 3

PK/BD ANALYSIS AND IN VITRO INTERNALIZATION ANALYSIS OF MACROMOLECULAR PRODRUG WITH DIFFERENT MOLECULAR WEIGHT, DRUG COTENT IN THE ASEPTIC IMPLANT LOOSENING MOUSE MODEL

3.1 Introduction

As discussed in Chapter 1, we would focus on elucidating the impact of different structural parameters on HPMA copolymer conjugates' PK/BD profile in an aseptic orthopedic implant loosening mouse model. The results from the study of this chapter will help identify the optimal structural design of the HPMA copolymer-based theranostic platform for early diagnosis and prophylactic treatment of peri-prosthetic osteolysis, respectively. We would try to develop a novel theranostic strategy for early diagnosis and effective treatment of peri-implant orthopedic wear particle-induced osteolysis by systematically manipulating the structural parameters of the system to optimize its extravasation/lymphatic clearance, cellular uptake, partitioning and drug release using the novel intraosseous femoral implant mouse model.

3.2 Materials and Methods

3.2.1 Materials

Ten-week-old male CD 1 IGS mice were purchased from Charles River Laboratories and maintained under standard housing conditions. All animal experiments

were performed in accordance with protocols evaluated and approved by the Institutional Animal Care and Use Committee (IACUC) of the University of Nebraska Medical Center.

3.2.2 Instruments

Isoflurane vaporizer (Midmark Corp, Dayton, OH) was used to anesthetize animals during live imaging analyses. A Faxitron MX-20 Cabinet X-ray System (Faxitron Bioptics, Tucson, AZ) was used in the implant loosening model establishment to confirm the implant position. A Packard Cobra II Gamma Counter (PerkinElmer, Waltham, MA) was used in the tissue radioactivity counting in the gamma counter-based PK/BD study. A Pearl Impulse small animal imaging system (LI-COR, Lincoln, NE) was used for near-infrared (NIR) optical imaging of live animals. Flow cytometry on disaggregated cells was performed on a BD LSRII flow cytometer (BD Biosciences, San Jose, CA) and on BD FACS Scan and BD FACS Canto cytometers for the in vitro uptake studies.

3.2.2 Establishment of a murine prosthesis failure model

A murine prosthesis failure model was established surgically as we described previously [141]. Poly(methyl methacrylate) (PMMA) particles (1−10 μm, Bangs Laboratories, Fishers, IN) were used to induce the peri-prosthetic inflammation. The position of the implant was validated with Faxitron MX-20 Cabinet X-ray System. Mice were administrated antibiotics (cefazolin sodium, 20 mg/kg, s.c.) immediately after surgery, and analgesics (buprenorphine, 0.5 mg/kg, s.c.) were given

twice daily for 3 days after surgery. Biweekly intraarticular injection of PMMA particles (1 mg in 10 μL sterile saline) into the left knee joint was done postoperatively to mimic the gradual particle releasing process in the patients. Saline of similar volume was injected into the right knee as the control. A total of 180 male CD 1 IGS mice were used in the gamma counter-based PK/BD analysis experiment, and 25 mice were used for the NIR imaging-based PK/BD analysis.

3.2.3 Gamma counter-based pharmacokinetic and biodistribution analysis

On 30th day post implant introduction, ^{125}I-labeled and unlabeled P-Dex-Tyr-NH_2 conjugates (~1.5 μCi/mice, 5 mg polymer/mice) were mixed and administered to mice (5 mice/group) via tail vein injection. Animals were sacrificed at designated time points (0.5, 2, 6, 16, 48, 168 h). Blood and other major organs/tissues including, heart, lungs, kidneys, liver, spleen, and both hind limbs were isolated at euthanasia. They were processed and analyzed using a Packard Cobra II Gamma Counter without perfusion. The pharmacokinetic parameters, such as total clearance (CL), the volume of distribution (V_d), and biological half-life ($t_{1/2}$) were determined using the bolus intravenous input noncompartmental analysis of WinNonlin (version 6.3, Pharsight, Mountain View, CA). The area under the curve (AUC) was calculated using the trapezoidal rule. The relative exposure ratio was calculated by dividing AUC_{tissue} by AUC_{blood}. AUC_{last} from both tissues and blood was used for the relative exposure ratio.

3.2.4 Near-infrared optical imaging analysis

On the 30th day post implant introduction, mice were given P-Dex- IRDye (0.3 mg/mice) via tail vein injection (5 mice/group). The mice were imaged at designated time points (0.5, 24, 48, 72, 96, 120, 144, 168 h) using a Pearl Impulse small animal imaging system to evaluate the distribution and retention of the IRDye-labeled prodrug. All mice were anesthetized with 2% isoflurane throughout procedures and dehaired before imaging. Imaging acquisition condition is dual channel (800 nm and white light) with 85 μm resolution. Images for each mouse were normalized using the same intensity scale with a common minimum and maximum value. The signal intensity from the left joints was semiquantitatively analyzed by the resident software (Pearl Impulse Software). The regions of interest (ROI) with identical areas were selected manually as a 59 × 59 (pixels) ellipse shape using a drawing tool in the software at both knee joints and background (Figure 3.1). The center of the ROI was located to the knee joint manually. Signal intensity of the knee joint minus background signal intensity was then corrected for the area (pixels). Although the fluorescence dye content was controlled similar when synthesized, to compare with the signals from animals receiving different conjugates, a signal standardization method was developed as follows: conjugate solutions (20 μL, 3 mg/mL) were dropped on a Petri dish and imaged at the same imaging conditions (Figure 3.1A). The signals from the droplets were analyzed using the same method described above. The signal from the left knee joint was corrected according to the signal intensity obtained from conjugates droplets images in Figure 3.1A

in order to eliminate the impact of different dye content in the conjugates during the in vivo imaging analysis. The equation is listed below:

$$Standardized\ Mean\ Signal\ Intensity\ (\%) = \frac{I_L - I_B}{\frac{I_i - I_{Bi}}{20\mu L \times 3mg/mL} \times 5mg} \times 100\%$$

where I_L is mean signal intensity from left knee ROI, I_B is mean signal intensity from background, I_i is mean signal intensity from initial droplet, and I_{Bi} is mean signal intensity from background in initial droplet image.

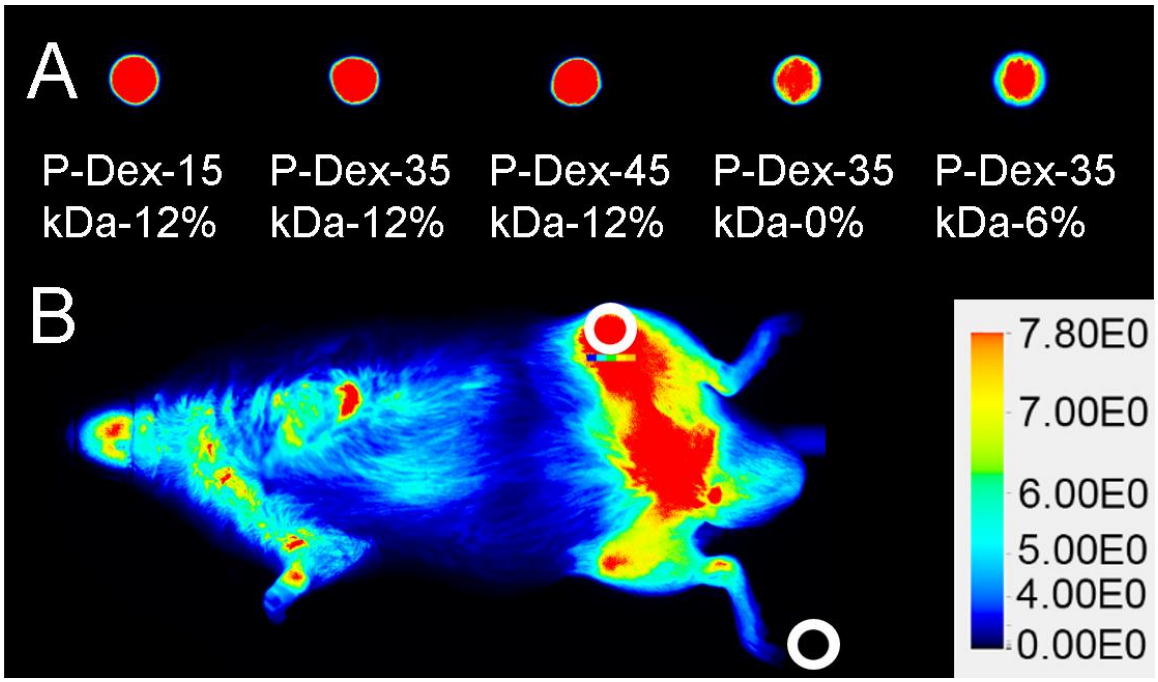

Figure 3.1 Near infrared imaging analysis of mice with systemic administration of P-Dex-IRDye conjugates. A. Images of conjugate solution drops (20 µL, 3 g/mL). The percentage represents the Dex content in each polymer conjugate tested. The circled areas identify representative regions of the ROI and background selected for analyses.

3.2.5 Fluorescence-activated cell scanning (FACS) analysis

The FACS analysis procedure was adapted from previous work [118]. Two days after the last intraarticular particle injection, the mice were given P-Dex-Alexa 488 (5 mg/mouse) via tail vein injection. At necropsy (24 h post injection), the left femurs were isolated and minced aseptically. The tissues were further digested with type IA collagenase (1 mg/mL, Sigma- Aldrich) at 37 °C for 30 min twice. After passing through a 70 μm cell strainer, ACK Lysing Buffer (Quality Biological, Gaithersburg, MD) was then used to remove the red blood cells. After centrifugation (1200 rpm, 5 min), a single cell suspension (1×10^6 cells/50 μL) was obtained. For FACS evaluation of dendritic cells, macrophage, monocytes, and fibroblast cells, the samples were incubated with the following antibodies: hamster anti-mouse CD11c (BD Biosciences, Pharmingen), Allophycocyanin (APC)-labeled rat antimouse F4/80 (eBioscience, San Diego, CA), APC-labeled rat antimouse Ly-6G (Gr-1, Gr1) (eBioscience, San Diego, CA), and Alexa Fluoro 647 labeled rabbit antimouse P4HB (Abcam, Cambridge, MA), respectively, for 30 min on ice. Cells incubated with hamster antimouse CD11c were further treated with Alexa Fluoro 647-labeled goat antihamster secondary antibody for another 30 min on ice. All the cells were then fixed in FACS fixation buffer and stored at 4 °C prior to analyses on a BD LSR II flow cytometer.

3.2.6 *In Vitro* internalization study of HPMA copolymer conjugates in macrophages.

To evaluate the internalization of HPMA copolymer conjugates in vitro, fluorescence microscopy and flow cytometry were used to conduct these studies.

3.2.6.1 Fluorescence microscope imaging.

Primary BMMs were prepared by conventional procedures and plated onto glass coverslips at a density of 2.5×10^5 cells per well of a 12-well plate in alpha-MEM medium supplemented with 10% fetal bovine serum and 25 ng/mL M-CSF. After overnight incubation, copolymers were added from a 20 mg/mL stock in PBS to a final concentration of 40 μg/mL. After additional 24 or 48 h incubation, cells were washed with HBSS, labeled with Hoechst 33342 (2 μg/mL for 5 min in HBSS), fixed with 2% paraformaldehyde for 15 min at 37 °C, washed with HBSS, and mounted using ProLong Gold Antifade mounting medium. Cells were imaged, and captured images were analyzed using a Nikon Eclipse fluorescence microscope.

3.2.6.2 Flow cytometric analysis.

Primary BMMs were prepared by conventional procedures and plated in alpha-MEM Petri dishes (one million cells in 8 mL per dish). After overnight incubation, polymers were added from a 20 mg/mL stock in PBS to a final concentration of 40 μg/mL. After additional incubation 4−48 h, cells were washed with PBS, trypsinized, washed again, and resuspended in 0.6 mL of stain buffer (BD Pharmigen). Cells were stained with a 7-AAD viability stain prior to flow cytometric analysis on FACScan or FACScanto cytometers.

3.3 Results

3.3.1 The pharmacokinetics and biodistribution of the HPMA copolymer conjugates in the peri-implant osteolysis mouse model

3.3.1.1 Gamma counter-based PK/BD analyses of HPMA copolymer conjugates in the peri-implant osteolysis mouse model using ^{125}I-labled conjugates

The percentage of injected conjugate dose per gram (ID/g) of tissue vs time (0.5, 2, 6, 16, 48, and 168 h postinjection) in all major organs, blood, and both femurs are shown in Figure 3.2. For P-Dex with different MWs but the same Dex content (~12 wt %), MW clearly had a major impact on the distribution of P-Dex conjugates in major organs. Of all the conjugates tested, P-Dex-40 kDa-12%, which has the highest MW, showed the maximum ID/g value in most of the organs examined at the earliest time points. In the kidney, however, the conjugate with the lowest MW (P-Dex-20 kDa-12%) was found with the highest ID/g values at the end point. While all other conjugates examined exhibited a biphasic clearance pattern, PDex-40 kDa-12%'s clearance showed a unique pattern. Increased ID/g values were found for P-Dex-40 kDa-12% during 2−6 h postinjection in all tissue and organs, during 16−48 h in the liver and both femurs, and during 48−168 h in the spleen. Increased ID/g values were also found in both femurs and spleen during 2−6 h postinjection with P-Dex-30 kDa-0%. In all organs and tissues, P-Dex-30 kDa-6% showed the lowest ID/g at every time point. The difference between the PMMA particle-injected left femur and nonparticle-injected right femur were not significant with all of the tested polymer conjugates, which is contrary to our previous findings [118].

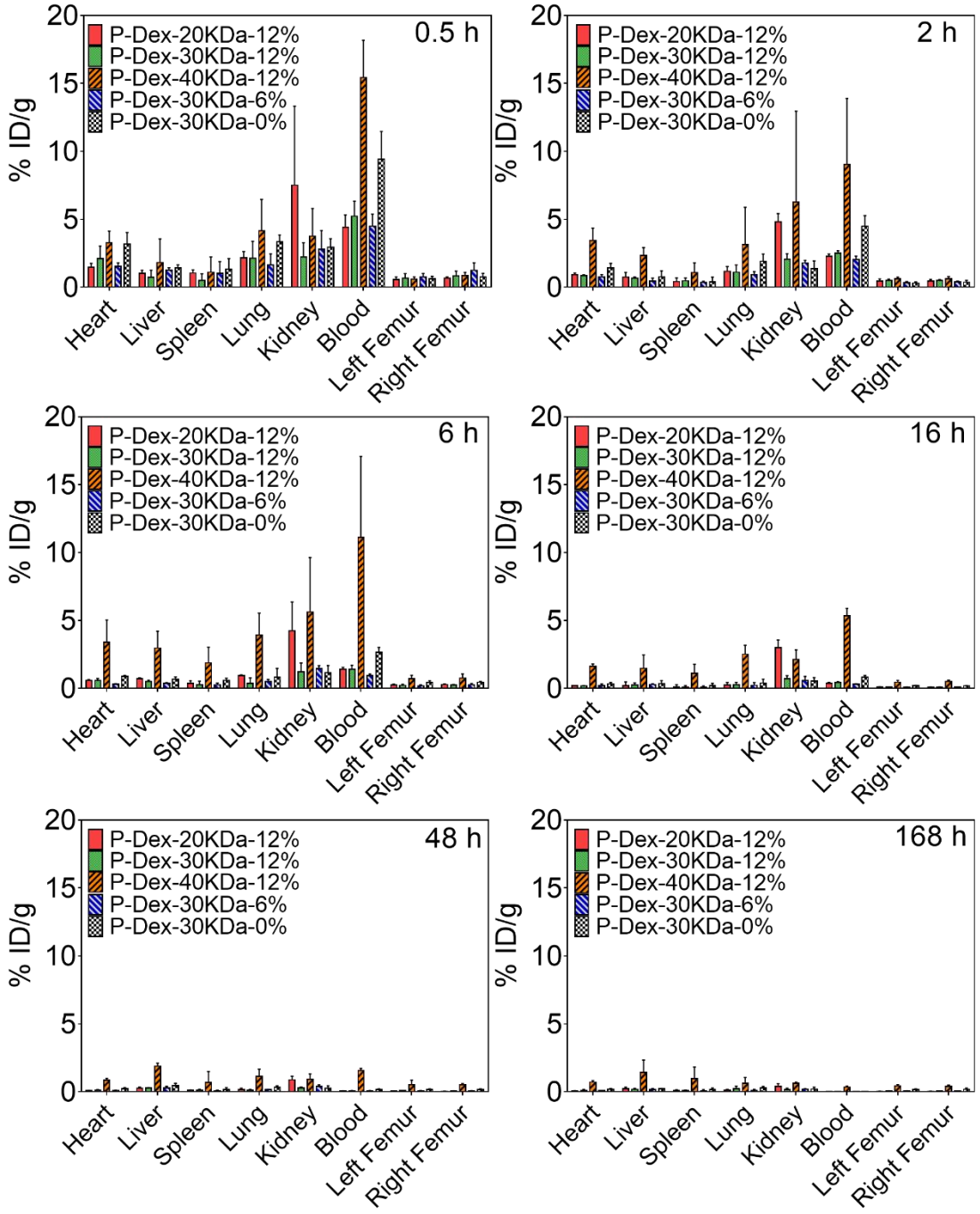

Figure 3.2 The pharmacokinetics profiles of HPMA copolymer conjugates with different molecular weights and Dex contents in blood and major organs/tissues over the time course of 7 days post i.v. administration. n=5.

3.3.1.2 Biodistribution of HPMA copolymer conjugates in tissues according to the live optical imaging

Due to the insensitivity of gamma counter-based PK/BD analysis techniques in defining the differential distribution pattern of P-Dex conjugates between the femur with peri-implant osteolysis and the control, we performed additional analyses using P-Dex conjugates labeled with IRDye 800CW. As shown in Figure 3.3, this approach confirmed the critical role of MW in determining the PK/BD profile. The retention time of the P-Dex in vivo increased with an increase in MW. Unlike the gamma counter-based PK/BD study, live NIR optical imaging permitted discrimination of the peri-implant inflammation site from the control site. The fluorescent signal intensity from left knee (with implant and particle infusion) increased with the increase of MW at the same time point post i.v. administration. When the signal from the knee joint was corrected as described in the equation in the methods section, the semiquantitative results (Figure 3.5) corroborate well with the visual observation. In Figure 3.4, the P-Dex-30 kDa-6% showed an unexpected PK/BD profile, comparing with all the other groups. The fast elimination of the conjugate was evidenced by the low signal from the mice after 48-h post-injection. This result was in agreement with the gamma counter-based PK/BD experiment finding using P-Dex-^{125}I.

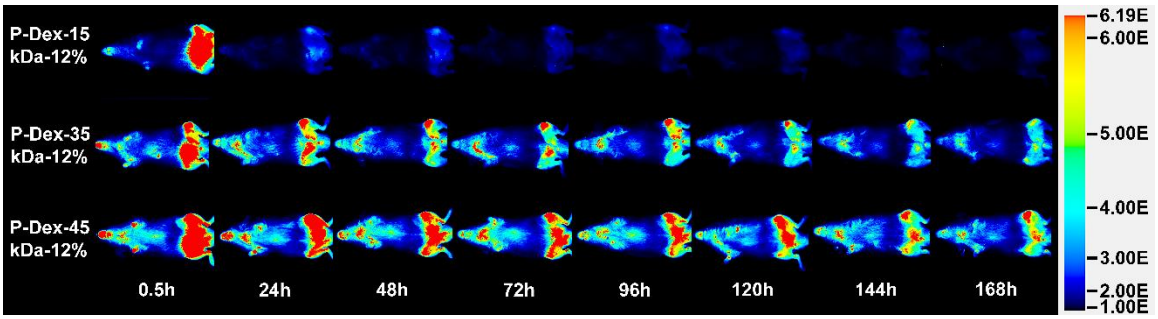

Figure 3.3 Representative NIR optical images of mice with femur implants challenged with PMMA particles on left femur and PBS on the contralateral side. Images were obtained 0.5, 24, 48, 72, 96, 120, 144, and 168 h after one intravenous injection of P-Dex-IRDye conjugates (Dex content ~12 wt %, with different MW). Pseudo color-coded signal intensity reflects the level of polymers within the mice. The signal intensity was normalized using the same intensity scale for each image.

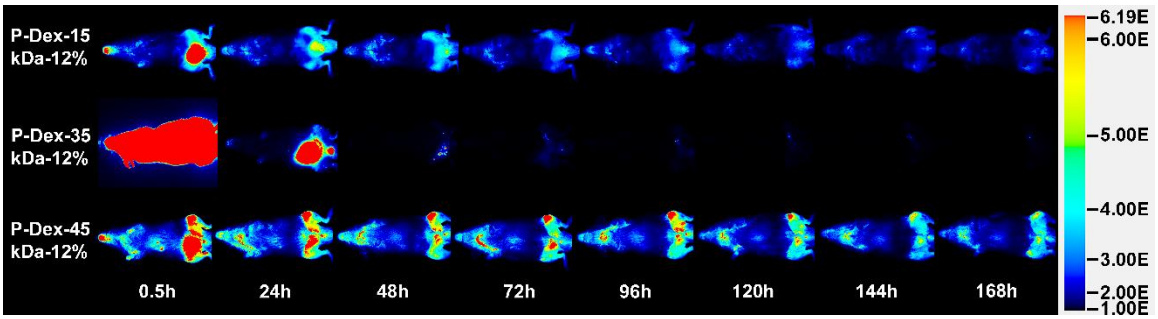

Figure 3.4 Representative NIR optical images of mice with femur implants challenged with PMMA particles on left femur and PBS on the contralateral side. Images were obtained 0.5, 24, 48, 72, 96, 120, 144, and 168 h after one intravenous injection of P-Dex (MW ~ 35 kDa, with different Dex content) at designed time points. Pseudo color-coded signal intensity reflects the level of polymers within the mice. The signal intensity was normalized using the same intensity scale for each image.

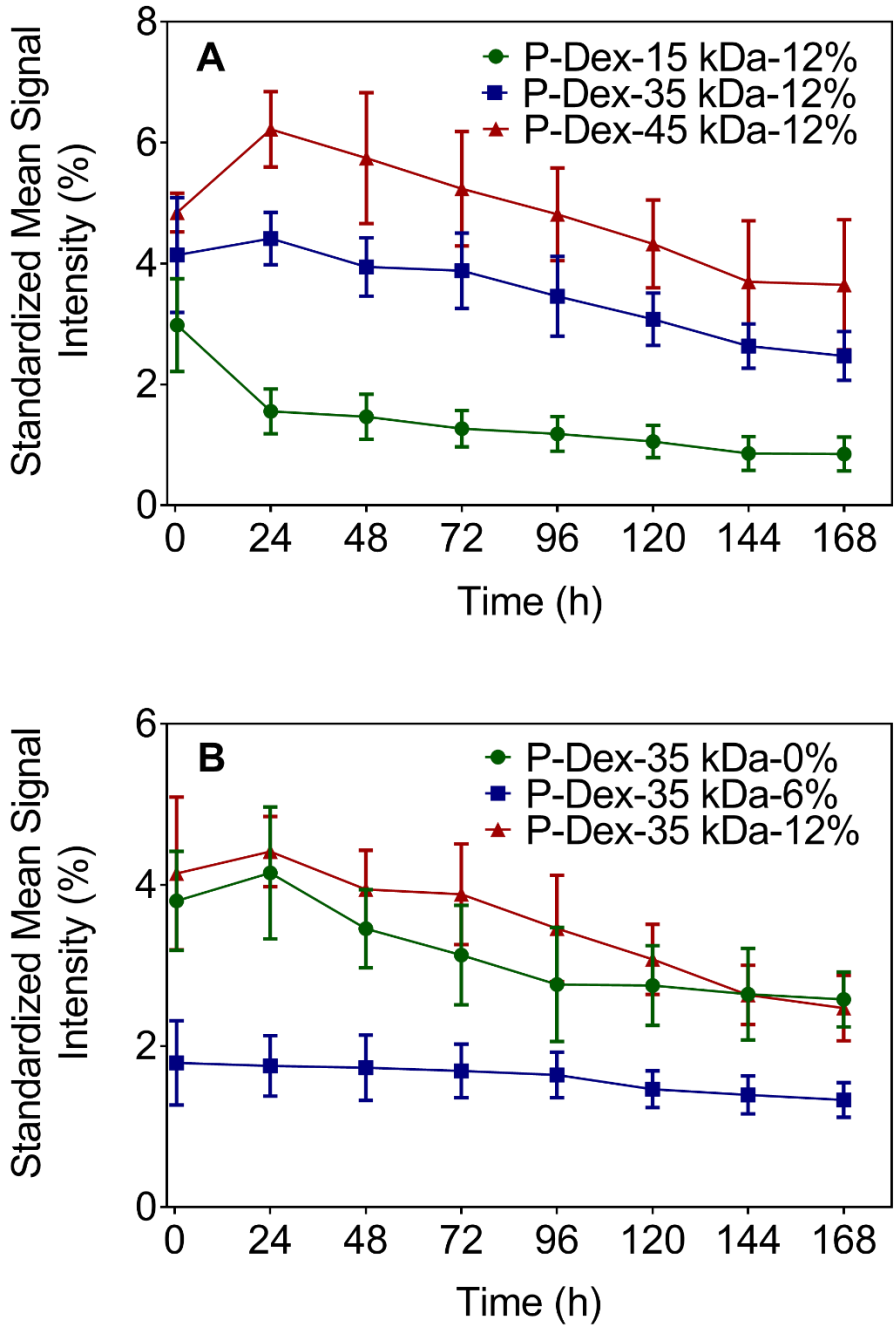

Figure 3.5 Semi-quantitative analysis of the image signals gained from optical image system.

3.3.2 Gamma counter-based pharmacokinetic analyses

PK parameters of the tested conjugates in blood and major organs/tissues were obtained using a noncompartmental analysis (Table 3.1). Systemic exposure as expressed by AUC and MRT increased with increasing MW. For example, AUC of PDex- 40 kDa-12% was ~26-fold higher than P-Dex-20 kDa-12%. Both V_d and Cl decreased with increasing MW, but the decrease in Cl was more pronounced, which leads to the overall increase in exposure as measured by AUC and MRT. Also the low Cl associated with higher MW formulation (P-Dex-40 kDa- 12%) led to the longer half-life of 35.8 h. Increasing the MW increased exposure of blood, as well as all other tissues as measured by AUC and MRT. Dex loading also affected the MRT and AUC. For example, P-Dex-30 kDa-0% had ~3-fold higher AUC0-∞ than P-Dex-30 kDa-6%, and Cl of P-Dex-30 kDa-6% was ~3-fold higher than P-Dex-30 kDa-0%; while PDex-30 kDa-12% had ~2-fold higher $AUC_{0-\infty}$ than P-Dex-30 kDa-6%, and Cl of P-Dex-30 kDa-6% was 2-fold higher than PDex- 30 kDa-12%.

Parameters (unit)	P-Dex-20 kDa-12%	P-Dex-30 kDa-12%	P-Dex-40 kDa-12%	P-Dex-30 kDa-6%	P-Dex-30 kDa-0%
$t_{1/2}$ (hr)	27.4 ± 5.9	22.3 ± 6.6	35.8 ± 3.7	23.9 ± 3.5	24.3 ± 4.7
Cl (mL/hr/kg)	316.9 ± 19.1	115.7 ± 10.6	12.5 ± 0.9	238.6 ± 11.6	73.9 ± 3.8
V_{ss}(mL/kg)	6,473.5 ± 301.6	1,850.6 ± 274.2	516.4 ± 77.7	4,225.1 ± 516.2	1,332.2 ± 154.3
$AUC_{0-\infty}$ (blood) (hr* count/gm)	376,071.8 ± 22102.0	1,057,256.4 ± 103135.1	10,134,744.0 ± 732647.0	520,626.4 ± 24637.4	1,682,399.0 ± 86933.0
AUC (% extrapolation)	1.1 ± 0.5	1.3 ± 1.5	4.2 ± 1.4	0.6 ± 0.3	0.7 ± 0.4
$AUC_{left\ femur}/AUC_{blood}$	0.34	0.38	0.23	0.43	0.39
$AUC_{right\ femur}/AUC_{blood}$	0.33	0.35	0.23	0.49	0.41
AUC_{heart}/AUC_{blood}	0.67	0.71	0.49	0.74	0.64
AUC_{liver}/AUC_{blood}	1.43	1.1	0.8	1.36	0.84
AUC_{spleen}/AUC_{blood}	0.64	0.52	0.42	0.45	0.43

AUC_{lungs}/AUC_{bood}	1.1	0.92	0.60	0.98	0.85
AUC_{kidney}/AUC_{bood}	6.02	1.6	0.57	2.32	0.77
$MRT_{0-\infty}$ (blood) (hr)	20.4 ± 0.6	16.1 ± 2.8	41.4 ± 5.9	17.7 ± 2.2	18.0 ± 1.3
$MRT_{left\ femur}/MRT_{bood}$	2.94	3.57	2.58	3.74	4.34
$MRT_{right\ femur}/MRT_{bood}$	2.97	3.54	2.44	3.43	4.33
MRT_{heart}/MRT_{bood}	2.64	3.36	2.03	3.29	3.30
MRT_{liver}/MRT_{bood}	4.06	4.09	2.38	3.83	3.68
MRT_{spleen}/MRT_{bood}	4.54	4.21	2.43	3.37	3.83
MRT_{lungs}/MRT_{bood}	2.88	4.29	1.70	3.08	3.85
MRT_{kidney}/MRT_{bood}	2.42	3.06	1.70	2.94	2.93

Table 3.1 The pharmacokinetic (PK) parameters of different HPMA copolymer conjugates after systemic administration. $t_{1/2}$, the half-life associated with the elimination phase; CL, total body clearance; Vss, volume of distribution in steady state; AUC, area under a concentration of analyte vs time curve.

3.3.3 *In Vivo* fluorescence-activated cell scanning (FACS) analysis

For all the tested cell phenotypes (CD11c+, F4/80+, Ly-6G (Gr-1, Gr1)+, and P4HB+, see Figure 3.6), the percentage of cells that internalized the P-Dex copolymers increased with the increase of the MW of the polymers (e.g., PDex-15 kDa-12%, P-Dex-35 kDa-12%, and P-Dex-45 kDa-12%). This increase was highly significant when the MW was raised from 15 to 35 kDa. For instance, the percentage of CD11c positive cell increased from 41.67% to 89.28% when treated with P-Dex-15 kDa-12% and P-Dex-35 kDa-12%, respectively. The difference in the percentage of the cells that internalized the polymers was not significant, however, when MW was raised from 35 to 45 kDa. The Dex content also affected the cell uptake of P-Dex copolymers. With the increase of Dex content, the percentage of the cells that internalized the P-Dex copolymers was also increased for several of the cell phenotypes tested in this study (see Table 3.2). As shown in Figure 3.7, over 90% of the cell-sequestered P-Dex-Alexa were found in Ly-6G (Gr-1, Gr1) positive cells. The cell uptake efficiency increased with the increases of P-Dex MW. The impact the Dex content has on cell internalization efficiency was more complex. For example, more P-Dex with higher Dex content was sequestrated by F4/80 positive cell, while more P-Dex with lower Dex content was sequestered by Ly-6G (Gr-1, Gr1) positive cells (see Table 3.3).

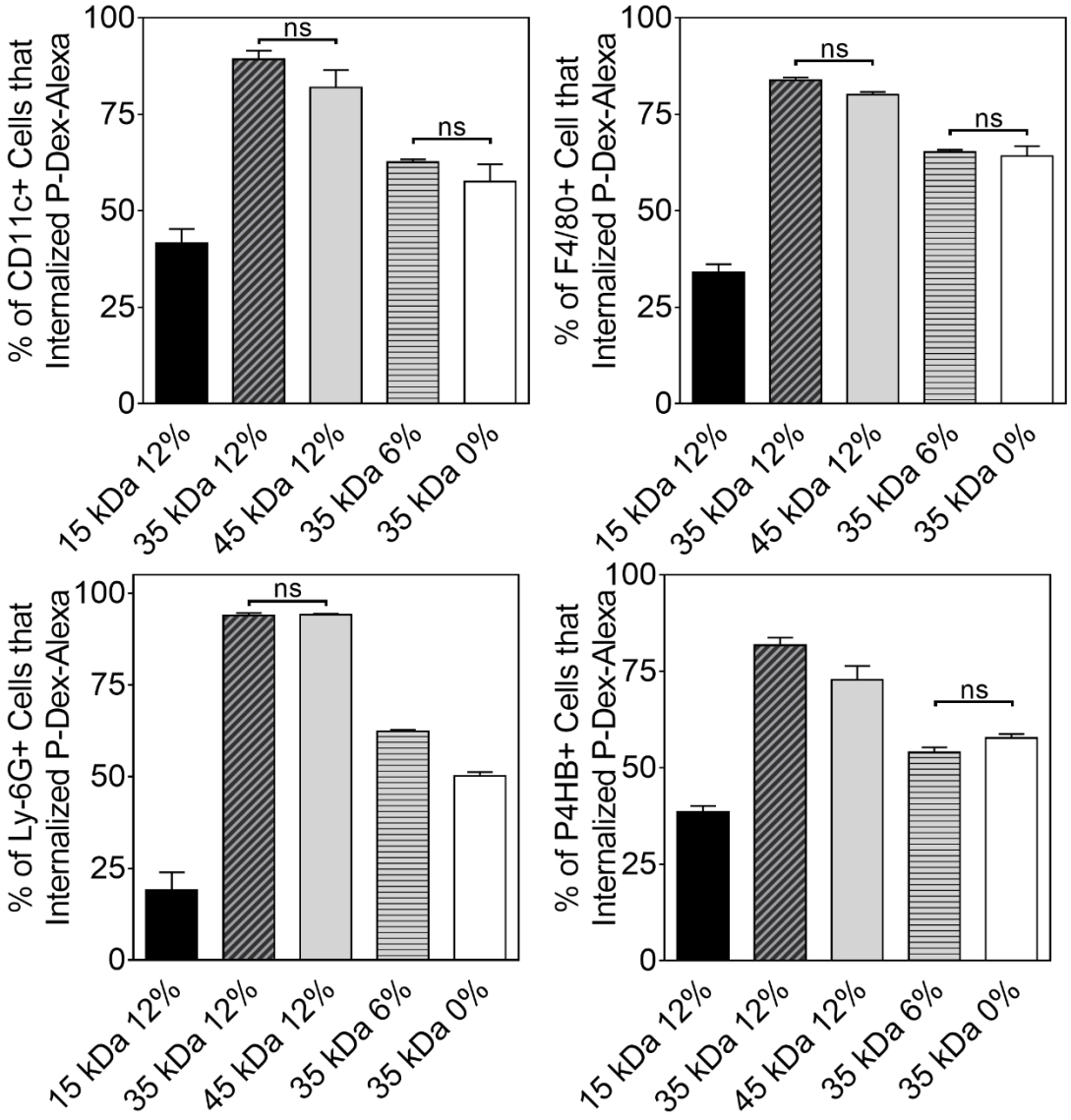

Figure 3.6 Percentage of different cell phenotypes isolated from peri-implant region that internalized different HPMA copolymers-Dex conjugate. Except for those noted as not significant (ns, $P > 0.05$), all the other paired group comparisons are statistically significant ($P < 0.05$).

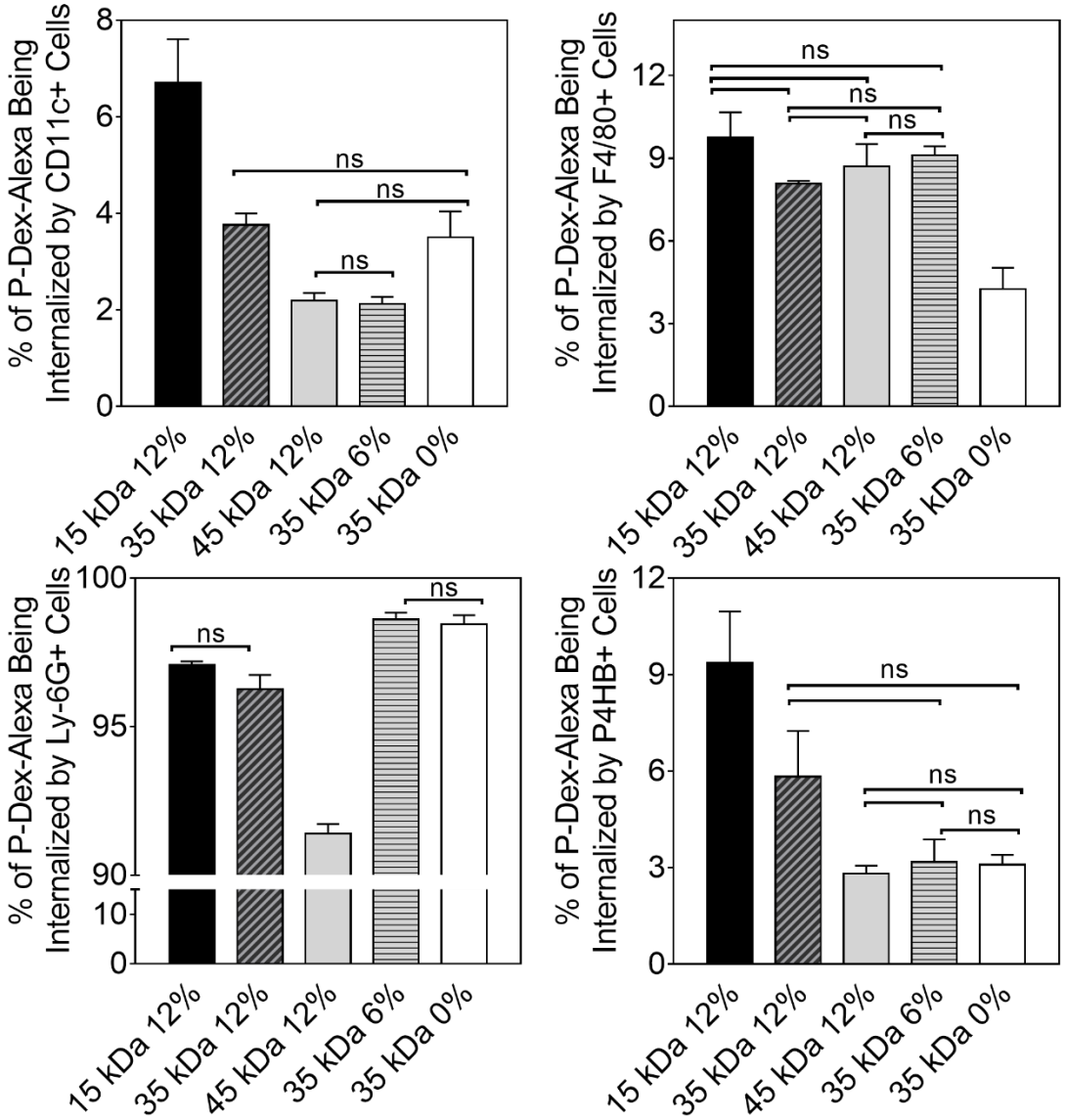

Figure 3.7 Percentage of P-Dex-Alexa internalized by different cell phenotypes isolated from peri-implant region. Except for those noted as not significant (ns, $P > 0.05$), all the other paired group comparisons are statistically significant ($P < 0.05$).

Polymer	P-Dex-15 kDa-12%	P-Dex-35 kDa-12%	P-Dex-45 kDa-12%	P-Dex-35 kDa-6%	P-Dex-35 kDa-0%
CD11c+	41.67	89.28	81.98	62.63	57.53
F4/80+	34.01	83.85	80.09	65.22	64.19
Ly6G+	18.99	93.94	94.16	62.38	50.20
P4HB	38.61	81.75	72.79	54.008	57.77

Table 3.2 The percentage of different cell phenotypes that internalized P-Dex-Alexa at the peri-implant region.

Polymer	P-Dex-15 kDa-12%	P-Dex-35 kDa-12%	P-Dex-45 kDa-12%	P-Dex-35 kDa-6%	P-Dex-35 kDa-0%
CD11c+	6.70	3.76	2.19	2.12	3.50
F4/80+	9.75	8.07	8.70	9.10	4.26
Ly6G+	97.07	96.26	91.40	98.61	98.45
P4HB	9.37	5.83	2.81	3.18	3.09

Table 3.3 The percentage of P-Dex-Alexa being sequestered by different cell phenotypes at the peri-implant region.

3.3.4 Impact of Structural Parameters on *in Vitro* BMM Internalization P-Dex.

To determine the effect of MW on cellular uptake of the HPMA copolymer conjugates, murine BMMs were incubated with Alexa-488 labeled P-Dex with Dex content ~12 wt % and different MW (ranging from 15 kDa to 45 kDa). Cells were analyzed using flow cytometry and fluorescence microscopy at 4, 24, and 48 h after addition of the copolymers to the cells. The flow cytometric data (Figure 3.8) revealed that all four of these copolymers were taken up by the BMMs, being detectable at 4 h and increasing throughout the time course. MW did not appear to have any significant effects on copolymer uptake since the kinetics and levels of uptake were very similar between the four copolymers. To determine the effect of Dex content on uptake of HPMA copolymers by BMMs, three copolymers of similar MW (~35 kDa), but differing Dex content were analyzed by flow cytometry and fluorescence microscopy as described above.

Flow cytometry revealed that the kinetics and levels of uptake of the P-Dex 35 kDa-6 wt % and P-Dex 35 kDa-12 wt % conjugates were indistinguishable (Figures 3.9 and 3.10). Uptake of the dexamethasone-free copolymer appeared somewhat higher than that of the dexamethasone-containing copolymers, which may in part be due to the relatively higher loading of Alexa Fluor 488 on this copolymer.

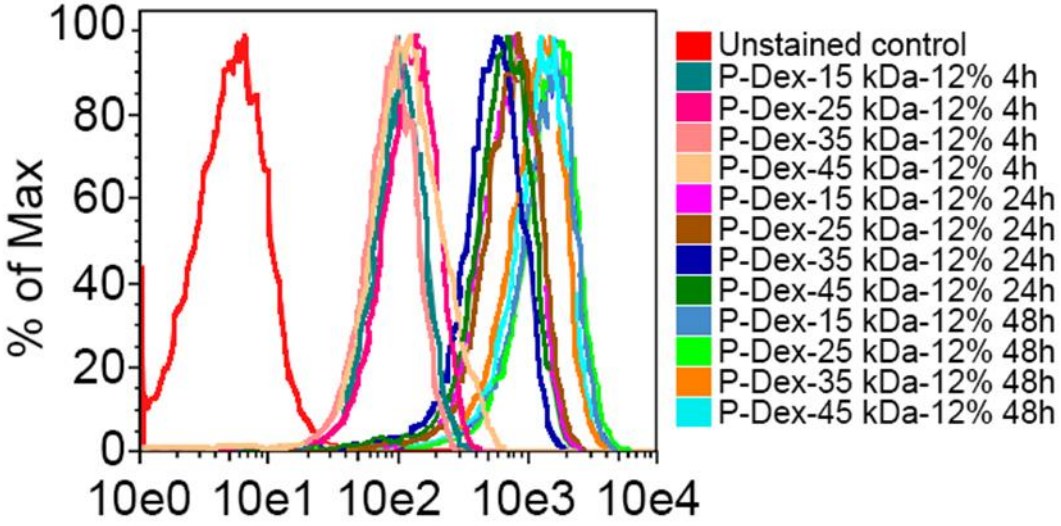

Figure 3.8 In vitro flow cytometry analysis of murine BMM internalization of P-Dex with different molecular weight (Dex content ~12 wt %, labeled with Alexa Fluor 488).

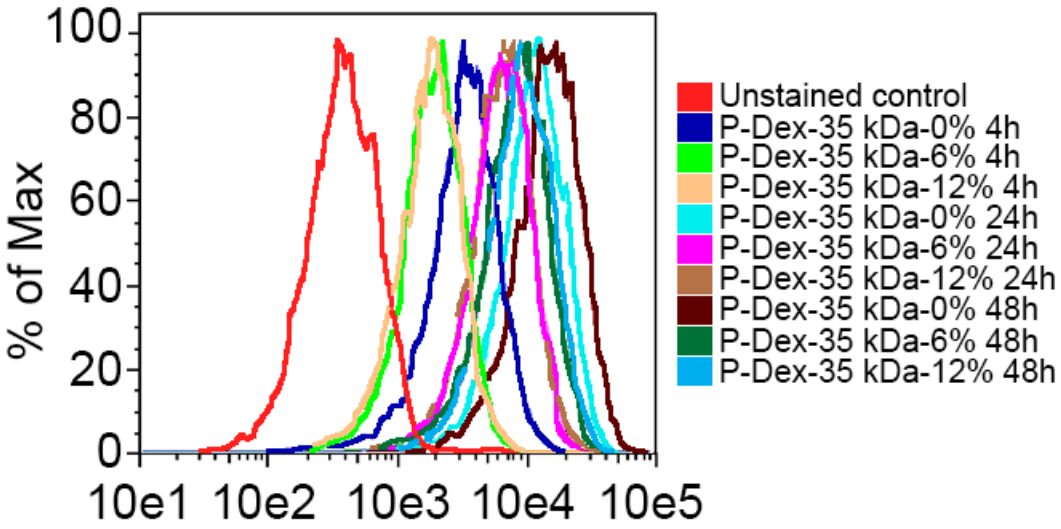

Figure 3.9 In vitro flow cytometry analysis of murine BMM internalization of P-Dex with different Dex content (MW ~ 35 kDa, labeled with Alexa Fluor 488).

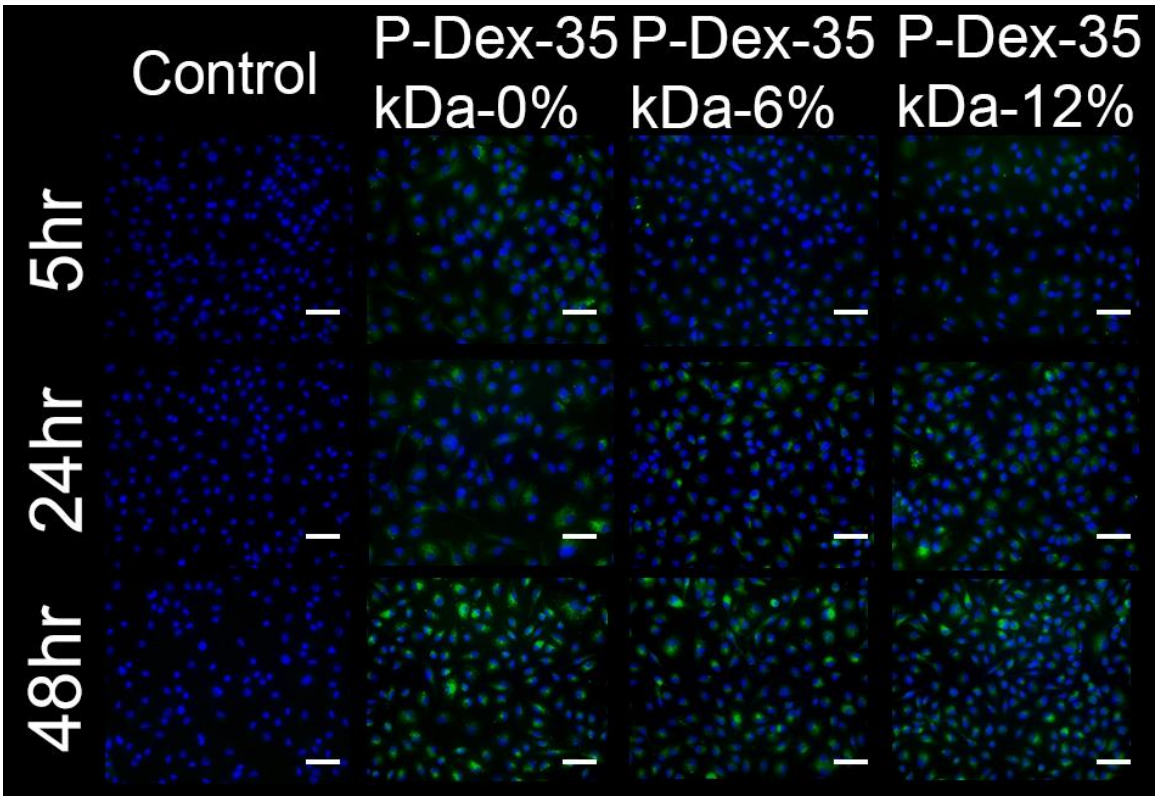

Figure 3.10 In vitro fluorescence microscope analysis of murine BMM internalization of P-Dex (MW ~ 35 kDa, with different Dex content), 20×, scale bar = 50 μm.

3.3.5 Dynamic Light Scattering Analysis of P-Dex

The dynamic light scattering analysis results of different P-Dex copolymers are presented in Table 3.4 and results for P-Dex-35 kDa-6% at different concentration can be seen in Table 3.5. The DLS data clearly suggests that P-Dex-35 kDa-6% forms aggregates under the conditions tested. This finding may partially explain the unexpected fast clearance of P-Dex-35 kDa-6% found in the PK/BD study.

Sample Name	P-Dex-15 kDa-12%	P-Dex-35 kDa-12%	P-Dex-45 kDa-12%	P-Dex-35 kDa-6%	P-Dex-35 kDa-0%
Z-Ave (d.nm)	6.643	7.673	8.552	163.9	6.828
PDI	0.237	0.318	0.209	0.481	0.174

Table 3.4 Dynamic light scattering (DLS) analysis of copolymers at a concentration of 5 mg/mL. Z-Ave: Z-Average size (diameter.nm); PDI: Polydispersity index.

Concentration (mg/mL)	**5**	**37.5**	**150**
Z-Ave (d.nm)	163.9	282.9	313.6
PDI	0.481	0.769	1

Table 3.5 Dynamic light scattering (DLS) analysis P-Dex-35 kDa-6% at different concentration. Z-Ave: Z-Average size (diameter.nm); PDI: Polydispersity index.

3.4 Discussion

As discussed in the chapter 2, the purpose of this chapter was to define the impact of MW and drug loading on PK/BD profile of HPMA copolymer-dexamethasone conjugates in a model of localized inflammation. Thus, we conducted this comprehensive comparison in a murine implant loosening model and obtained the following finds.

3.4.1 Impact of Molecular Weight on PK/BD Profile.

MW clearly had a major impact on the PK/BD profiles of P-Dex conjugates in the gamma counter-based analyses (Figure 3.2). There was greater uptake and retention of the conjugates with the higher MWs in the major organs at every time point evaluated, with the kidney as the only exception, which may be due to the fact that the HPMA copolymer conjugates are known to be cleared through the kidney, and the lower MW conjugates would be expected to have more rapid renal clearance [79, 152, 153]. This was also reported in our previous finding when analyzing the PK/BD profile of HPMA copolymer conjugates using inflammatory arthritis rat model [144]. The %ID/g of most of the P-Dex conjugates in all the organs and tissues decreased over time. In this analysis, we also found the ^{125}I activity (representing the amount of P-Dex) between the particle-injected left femur and nonparticle-injected right femur was not significantly different, which was not consistent with our previous findings [154, 155]. The systemic exposure of the conjugate increased when the MW was raised. The $AUC_{0-\infty}$ (blood) of the conjugates positively correlated with the MW of the conjugates, and Cl of the polymers

was negatively correlated to the MW of the polymers. There is no significant difference between $AUC_{left\ femur}/AUC_{bood}$ and $AUC_{right\ femur}/AUC_{bood}$ for all the tested polymer conjugates. Review of the protocol suggests that the discrepancy may be attributed to the technical limitation of not being able to isolate the peri-implant inflammatory tissue from the surrounding noninvolved tissues.

Instead, the whole leg was isolated without perfusion. Since the tissue samples harvested were much larger than the peri-implant inflammatory lesion in this model, the radioactivity associated with the large quantities of nonrelevant tissue may have masked the small activity of the P-Dex-^{125}I targeted to the peri-implant lesion, leading to the inconclusive results. In order to overcome the limitation of the gamma counter-based PK/BD analyses, we conducted a semiquantitative near-infrared optical imaging-based PK/BD analysis to better recapitulate the passive targeting of P-Dex to the peri-implant lesion. The methodology was successful in establishing the preferential localization of the P-Dex in the particle-injected left femurs, and this was true for all the polymer conjugates tested. Furthermore, as evident in Figures 3.3 and 3.5, the increase of MW provided longer retention of the polymers at the peri-implant inflammatory site and better differentiation of the left (with particle infusion) and right (without particle infusion) legs. Also shown in Figure 6, there was a trend of increase of ROI signal intensity at 1-day postinjection for both P-Dex-35 kDa-12% and P-Dex-45 kDa-12% groups. This may be due to recirculation of the copolymers in the system [156].

3.4.2. Impact of Drug Loading on the PK/BD Profile.

Based on the findings presented in Figures 3.2 and 3.4 and Table 3.1, higher Dex content provided a higher systemic exposure and a longer retention of conjugates at the inflammatory site. An unexpected finding was that the P-Dex with ~6 wt % Dex content exhibited unusually rapid elimination in both gamma counter analysis and NIR optical imaging studies, which was not found in our previous work using inflammatory arthritis rat model [144]. This experiment was repeated multiple times, and the results were confirmed. Further examination revealed that the PBS or DD water solution of P-Dex-30 kDa-6% and P-Dex-35 kDa-6% was cloudy, which suggested the potential of polymer aggregation in the solutions. DLS analyses of the P-Dex-35 kDa-6% in DD water confirmed the presence of aggregates, and the aggregation size was positively correlated with the increase of the concentration. Compared to nonaggregating HPMA copolymers, the P-Dex-35 kDa-6% aggregates (>150 nm even after dilution associated with systemic administration) may be more rapidly internalized by the mononuclear phagocytic system (MPS), leading to their enhanced clearance [157]. The gamma counter-based PK/BD analysis, however, did not find high radioactivity in livers or spleens after P-Dex-35 kDa-6% administration. The NIR optical imaging (Figure 3.4) seemed to support a very rapid renal clearance for the polymer. Clearly, the further investigations are necessary to better understand the mechanism of the copolymer aggregation and its rapid in vivo clearance.

To understand the impact of the P-Dex with different structural parameters on cell uptake and sequestration in vitro, BMMs were treated with P-Dex of different

MW and Dex content and analyzed at different time points for copolymer uptake and sequestration by flow cytometry and fluorescence microscopy. The results of these experiments revealed no significant differences in the kinetics or levels of uptake between P-Dex of different MW or Dex content (which correlates with the finding of others) [158], suggesting that cell autonomous mechanisms for copolymer uptake and sequestration operate independently of MW or Dex content. To explore cellular uptake in the peri-implant tissue in vivo, Alexa Fluor 488 labeled copolymers were given to mice. As shown in Figures 3.6 and 3.7 and Tables 3.2 and 3.3, the FACS analysis of the peri-implant tissue confirmed that all the copolymers were predominantly taken up by inflammatory myeloid cells (including inflammatory monocytes, macrophages, and dendritic cells), with a minor component internalized by fibroblastic cells. For all cell populations analyzed, there was a trend toward increased frequencies of cells internalizing copolymer with increasing MW. In addition, the increase of Dex content also enhanced the cell-mediated sequestration, especially for the CD11c+ cells. Since our in vitro cell culture study suggested that the alteration of MW and Dex content would have minimal impact on BMM internalization of the PDex, we speculate that the increased in vivo sequestration of PDex with higher MW polymers and/or higher Dex content might be mainly attributed to their increased exposure to the cells as demonstrated by their higher t1/2, AUC, MRT, and lower Cl. The results from this comprehensive study are informative in assisting the future structural design of HPMA copolymerbased theranostic system for early detection and prophylactic in-

tervention of peri-implant osteolysis. Based on the findings of this study, we believe the use of a high MW (less than 45 kDa to ensure eventual renal clearance) HPMA copolymer as the carrier for MRI, SPECT/CT, or PET/CT imaging modalities may provide the best early diagnostic tool. While this high MW would also cause the imaging probe's distribution to off-target anatomical locations, its potential risk of off-target toxicity is minimal due to its infrequent use and relatively low dosing level. For therapeutic intervention, the data from the current study also suggest that the use of a high MW (but less than 45 kDa to ensure eventual renal clearance) HPMA copolymer as the drug carrier to ensure the optimal targeting to the periimplant inflammatory lesion. The off-target distribution and associated toxicities, however, cannot be underestimated in this case. While our previous study suggests the long-term use of P-Dex in managing peri-implant osteolysis may not cause systemic osteopenia [119], its impact on other sensitive organs and tissues (e.g., adrenal gland) is yet to be evaluated. If the safety profile of the HPMA copolymer−drug conjugate is not acceptable, a localized delivery strategy may be considered as an alternative. Though the mechanism is not yet understood, the finding of P-Dex aggregation at certain Dex content (6 wt %) must be carefully evaluated when considering clinical translation of this potential macromolecular prodrug conjugate, in order to ensure safety and a favorable PK/BD profile.

3.5 Conclusion

Using gamma counter-based and optical imaging-based methodologies, we evaluated the impact of structural parameters (i.e., molecular weight and drug content) on the pharmacokinetic and biodistribution (PK/BD) profiles of HPMA copolymer-dexamethasone conjugates in an aseptic peri-implant inflammation/osteolysis mouse model. The study found that the increase of both the MW and Dex content facilitated targeting of P-Dex to sites of local inflammation through increasing systemic exposure and reduced renal clearance of the conjugates. At certain level of Dex content (6 wt %), P-Dex may aggregate, leading to a more rapid elimination of the copolymers from the system. Our findings will assist in the future design and development of HPMA copolymer-based theranostic platform for early detection and therapeutic intervention of peri-implant osteolysis and implant failure.

CHAPTER 4

IN VIVO EVALUATION OF MACROMOLECULAR PRODRUG WITH DRUG-CONTAINING MONOMERS THERAPEUTIC EFFICACY AND REDUCTION OF TOXICITY

4.1 Introduction

As discussed in Chapter 1, drug releasing kinetic would have influence on the drug therapeutic efficacy and toxicity reduction.

4.2 Materials and Methods

4.2.1 Instruments

Isoflurane vaporizer (Midmark Corp, Dayton, OH) was used to anesthetize animals during arthritis induction. Rats ankle diameter were measured using a digital caliper (World Prescision Instruments, Inc., Saraspta, FL, USA). Bone quality were analyzed using a Skyscan 1172 high resolution micro-CT system (Skyscan, Kontich, Belgium). A Faxitron® MX-20 Cabinet X-ray System (Tucson, Arizona, USA) was used to monitor the hard tissue decalcification progress. A Leica RM2255 rotary microtome (Leica Biosystems Inc., Buffalo Grove, IL, USA) was used for paraffin-embedded tissue sectioning.

4.2.2 The therapeutic evaluation of HPMA copolymers conjugates in adjuvant-induced arthritis rats

Male Lewis rats (175-200 g) obtained from Charles River Laboratories (Wilmington, MA, USA) were used to establish the adjuvant-induced arthritis (AA) rat

model as described previously [146]. The rats were randomly divided into seven groups: P-Dex-A, P-Dex-C, P-Dex-D, and P-Dex-E treatment (n = 7, single i.v. injection on day 14 post-induction, dose equivalent of Dex = 10 mg/kg), Dexamethasone Sodium Phosphate treatment (n=7, equivalent of Dex = 10 mg/kg, divided into 4 aliquots and injected on Day 14, 15, 16, 17), and saline control (n=4). An additional group (n=4) of healthy rats were used as a negative control. Rats' joint edema and body weight were monitored daily from day 11. Blood was collected for liver enzyme analysis at necropsy. All major organs and limbs were collected at the euthanasia and fixed with buffered formalin before paraffin embedding at day 44. All animal experiments were performed in accordance with protocols approved by the Institutional Animal Care and Use Committee (IACUC) of the University of Ne-braska Medical Center or Hospital for Special Surgery.

4.2.3 Observational assessment of AA rats' joint inflammation

The articular index (AI) score was recorded during the treatment by the same observers (XW and GZ) as described previously. An AI score was given to each hind limb from day 11 to day 56 post-arthritis induction. The AI scoring system is based on a 0-4 numeric system as the following: 0 = no signs of swell-ing or erythema; 1 = slight swelling and/or erythema; 2 = low-to-moderate edema and signs involving the tarsals; 3 = pronounced edema with limited use of the joint and signs extending to the metatarsals; 4 = excessive edema with joint ri-gidity and severe signs involving the entire hind paw. The sum of the two hind limb scores for each animal was recorded. Ankle diameter (medial to lateral) was measured using a digital caliper as confirmation of inflammation-associated edema/hyperplasia.

4.2.4 Micro-CT analysis of articular bone quality

Hind limbs were isolated after euthanasia and fixed with buffered formalin for no less than 48 hr. The ankle joint bone quality was analyzed using a Skyscan 1172 micro-CT system. Micro-CT scanning parameters were set as fol-lows: voltage, 70 kV; current, 142 μA; exposure time, 1915 ms; resolution, 13.26 μm; with aluminum filter (0.5 mm); rotation step = 0.4°; frame averaging = 4; random movement = 10; using 180° rotation scanning. Raw data were reconstructed using NRecon to obtain a visual representation of the results, and the volume rendering of the samples were performed via CTvox software (Skyscan). To quantitatively compare the four treatments, the entire calcaneus and the selected region of interest (ROI) of the trabecular bone within the calcaneus were used as the anatomical sites for micro-CT analyses. The ROI was defined by aligning the calcaneus bone along the sagittal plane using Data-viewer, with the ROI starts at the 75th slide away from the epiphyseal plate and continues for 76 slides (1.98 mm). The diameter of the cylindrical ROI was set at 1.00 mm. The morphometric parameters, such as percent bone volume (BV/TV), bone surface density (BS/TV), trabecular separation (Tb.Sp), trabecular number (Tb.N), bone mineral density (BMD), and trabecular thickness (Tb.Th) were cal-culated using CTAn (Skyscan

4.2.5 Statistical methods

Two-way analysis of variance (ANOVA), followed by Tukey's post hoc test to account for multiple comparisons, was used for data analysis using GraphPad Prism Software. P-values ≤ 0.05 were considered statistically significant.

4.3 Results

4.3.1 The polymers provides different pattern of sustained amelioration of joint inflammation in AA rats

Ankle diameter and AI score of the P-Dex-A, P-Dex-C, P-Dex-D, P-Dex-E, and Dex treated group exhibited different outcome upon treatment. Dex treated group showed an immediate recovery of the swelling, however, a dramatic flare upon cessation of Dex treatment on day 19 (Figure 4.1). A single injection of Dex containing HPMA conjugates (dose equivalent to the Dex treatment) resulted in different level of reductions in ankle swelling and AI score from day 15 to 44. The ankle diameter difference significance of different treatment group was summarized in Table 4.1, Table 4.2 and Table 4.3 for the comprehensive comparison. The therapeutic efficacy difference was also in agreement of the in vitro releasing profiles of the polymer conjugates (Figure 2.8).

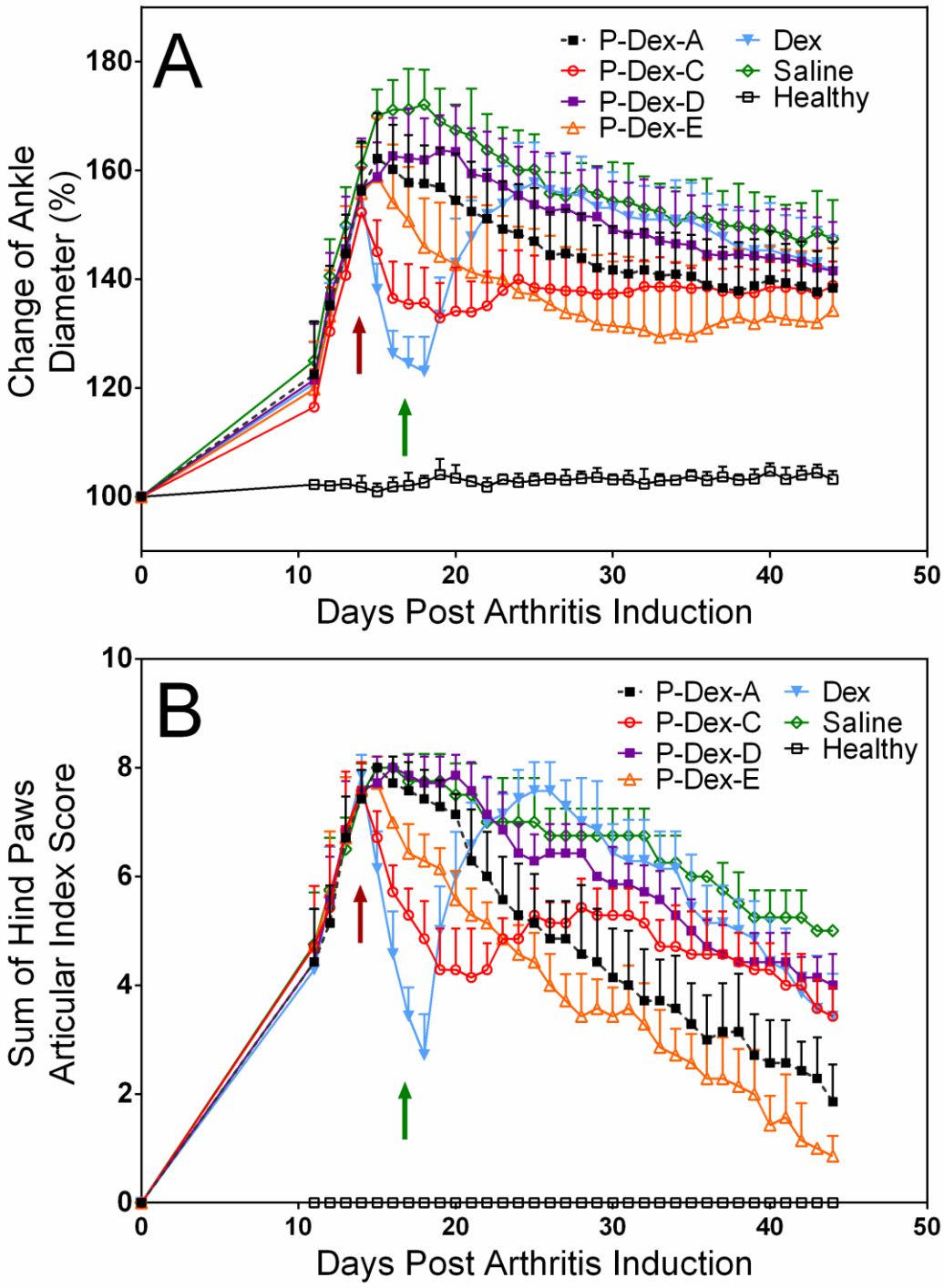
A
P-Dex-A
P-Dex-C
P-Dex-D
P-Dex-E
Dex
Saline
Healthy
Change of Ankle Diameter (%)
180
160
140
120
100
0
10
20
30
40
50
Days Post Arthritis Induction
B
P-Dex-A
P-Dex-C
P-Dex-D
P-Dex-E
Dex
Saline
Healthy
Sum of Hind Paws Articular Index Score
10
8
6
4
2
0
0
10
20
30
40
50
Days Post Arthritis Induction

Figure 4.1 HPMA conjugates polymerized with different dexamethasone containing monomers showed different therapeutic effect on amelioration of joint inflammation in an adjuvant-induced arthritis (AA) rat model. (A) The change of AA rats' left ankle joint size of different groups during the treatment study; (B) The change of articular index score of different groups during the treatment study. The red arrow indicated the day when rats received the single conjugates injection and the daily free Dex treatment was initiated. The green arrow indicated the day when rats received their last free Dex treatment. The prevention of arthritic ankle swelling by single injection of P-Dex-E was sustained for about one month from day 15 to day 44.

	Day 0	Day 11	Day 12	Day 13	Day 14	Day 15	Day 16	Day 17	Day 18	Day 19	Day 20	Day 21
P-Dex-A vs. P-Dex-C	ns	ns	ns	ns	ns	****	****	****	****	****	****	****
P-Dex-A vs. P-Dex-D	ns	ns	ns	ns	ns	ns	ns	ns	ns	ns	*	ns
P-Dex-A vs. P-Dex-E	ns	ns	ns	ns	ns	ns	ns	ns	**	***	**	**
P-Dex-A vs. Dex	ns	ns	ns	ns	ns	****	****	****	****	****	**	ns
P-Dex-A vs. Saline	ns	ns	ns	ns	ns	ns	*	**	***	**	**	**
P-Dex-A vs. Healthy	ns	****	****	****	****	****	****	****	****	****	****	****
P-Dex-C vs. P-Dex-D	ns	ns	ns	ns	ns	***	****	****	****	****	****	****
P-Dex-C vs. P-Dex-E	ns	ns	ns	ns	ns	***	****	****	*	**	ns	ns
P-Dex-C vs. Dex	ns	ns	ns	ns	ns	ns	*	**	**	ns	ns	***
P-Dex-C vs. Saline	ns	ns	ns	ns	ns	****	****	****	****	****	****	****
P-Dex-C vs. Healthy	ns	**	****	****	****	****	****	****	****	****	****	****
P-Dex-D vs. P-Dex-E	ns	ns	ns	ns	ns	ns	ns	**	****	****	****	****
P-Dex-D vs. Dex	ns	ns	ns	ns	ns	****	****	****	****	****	****	**
P-Dex-D vs. Saline	ns	ns	ns	ns	ns	*	ns	ns	ns	ns	ns	ns
P-Dex-D vs. Healthy	ns	****	****	****	****	****	****	****	****	****	****	****

P-Dex-E vs. Dex	ns	ns	ns	ns	ns	****	****	****	****	**	ns	ns
P-Dex-E vs. Saline	ns	ns	ns	ns	ns	*	****	****	****	****	****	****
P-Dex-E vs. Healthy	ns	****	****	****	****	****	****	****	****	****	****	****
Dex vs. Saline	ns	ns	ns	ns	ns	****	****	****	****	****	****	****
Dex vs. Healthy	ns	****	****	****	****	****	****	****	****	****	****	****
Saline vs. Healthy	ns	****	****	****	****	****	****	****	****	****	****	****

Table 4.1 The statistical analyses of the joint diameter of the rats from different treatment groups from Day 11 to Day 21 including the day of the adjuvant induction Day 0. Two-way analysis of variance (ANOVA), followed by Tukey's post hoc test to ac-count for multiple comparisons, was used for data analysis using GraphPad Prism Software. (*, $P \leqslant 0.05$; **, $P \leqslant 0.01$; ***, $P \leqslant 0.001$; ****, $P \leqslant 0.0001$).

	Day 22	Day 23	Day 24	Day 25	Day 26	Day 27	Day 28	Day 29	Day 30	Day 31	Day 32	Day 33
P-Dex-A vs. P-Dex-C	****	**	ns	ns	ns	ns	ns	ns	ns	ns	ns	ns
P-Dex-A vs. P-Dex-D	ns	ns	ns	ns	ns	ns	ns	*	ns	ns	ns	ns
P-Dex-A vs. P-Dex-E	**	*	**	*	*	**	**	**	*	*	**	**
P-Dex-A vs. Dex	ns	ns	ns	**	**	**	**	**	**	**	*	*
P-Dex-A vs. Saline	**	**	*	**	*	*	**	**	**	**	*	*
P-Dex-A vs. Healthy	****	****	****	****	****	****	****	****	****	****	****	****
P-Dex-C vs. P-Dex-D	****	****	****	****	***	****	***	***	**	*	*	ns
P-Dex-C vs. P-Dex-E	ns	ns	ns	ns	ns	ns	ns	ns	ns	ns	ns	ns
P-Dex-C vs. Dex	****	****	****	****	****	****	****	****	****	***	**	**
P-Dex-C vs. Saline	****	****	****	****	****	****	****	****	****	***	**	**
P-Dex-C vs. Healthy	****	****	****	****	****	****	****	****	****	****	****	****
P-Dex-D vs. P-Dex-E	****	****	****	****	****	****	****	****	****	****	****	****
P-Dex-D vs. Dex	ns	ns	ns	ns	ns	ns	ns	ns	ns	ns	ns	ns
P-Dex-D vs. Saline	ns	ns	ns	ns	ns	ns	ns	ns	ns	ns	ns	ns

P-Dex-D vs. Healthy	****	****	****	****	****	****	****	****	****	****	****	****
P-Dex-E vs. Dex	**	***	****	****	****	****	****	****	****	****	****	****
P-Dex-E vs. Saline	****	****	****	****	****	****	****	****	****	****	****	****
P-Dex-E vs. Healthy	****	****	****	****	****	****	****	****	****	****	****	****
Dex vs. Saline	*	ns	ns	ns	ns	ns	ns	ns	ns	ns	ns	ns
Dex vs. Healthy	****	****	****	****	****	****	****	****	****	****	****	****
Saline vs. Healthy	****	****	****	****	****	****	****	****	****	****	****	****

Table 4.2 The statistical analyses of the joint diameter of the rats from different treatment groups from Day 22 to Day 33 including the day of the adjuvant induction Day 0. Two-way analysis of variance (ANOVA), followed by Tukey's post hoc test to ac-count for multiple comparisons, was used for data analysis using GraphPad Prism Software. (*, $P \leqslant 0.05$; **, $P \leqslant 0.01$; ***, $P \leqslant 0.001$; ****, $P \leqslant 0.0001$).

	Day 34	Day 35	Day 36	Day 37	Day 38	Day 39	Day 40	Day 41	Day 42	Day 43	Day 44
P-Dex-A vs. P-Dex-C	ns	ns	ns	ns	ns	ns	ns	ns	ns	ns	ns
P-Dex-A vs. P-Dex-D	ns	ns	ns	ns	ns	ns	ns	ns	ns	ns	ns
P-Dex-A vs. P-Dex-E	**	**	ns	ns	ns	ns	ns	ns	ns	ns	ns
P-Dex-A vs. Dex	*	*	**	*	ns	ns	ns	ns	ns	ns	ns
P-Dex-A vs. Saline	ns	*	**	*	*	*	ns	ns	ns	*	ns
P-Dex-A vs. Healthy	****	****	****	****	****	****	****	****	****	****	****
P-Dex-C vs. P-Dex-D	ns	ns	ns	ns	ns	ns	ns	ns	ns	ns	ns
P-Dex-C vs. P-Dex-E	ns	ns	ns	ns	ns	ns	ns	ns	ns	ns	ns
P-Dex-C vs. Dex	**	**	*	*	ns	ns	ns	ns	ns	ns	ns
P-Dex-C vs. Saline	*	**	*	*	*	*	ns	ns	ns	*	ns
P-Dex-C vs. Healthy	****	****	****	****	****	****	****	****	****	****	****
P-Dex-D vs. P-Dex-E	****	****	***	**	**	***	**	**	**	*	ns
P-Dex-D vs. Dex	ns	ns	ns	ns	ns	ns	ns	ns	ns	ns	ns
P-Dex-D vs. Saline	ns	ns	ns	ns	ns	ns	ns	ns	ns	ns	ns

P-Dex-D vs. Healthy	****	****	****	****	****	****	****	****	****	****	****
P-Dex-E vs. Dex	****	****	****	****	***	***	**	**	**	**	ns
P-Dex-E vs. Saline	****	****	****	****	****	****	***	***	***	****	**
P-Dex-E vs. Healthy	****	****	****	****	****	****	****	****	****	****	****
Dex vs. Saline	ns	ns	ns	ns	ns	ns	ns	ns	ns	ns	ns
Dex vs. Healthy	****	****	****	****	****	****	****	****	****	****	****
Saline vs. Healthy	****	****	****	****	****	****	****	****	****	****	****

Table 4.3 The statistical analyses of the joint diameter of the rats from different treatment groups from Day 34 to Day 44 including the day of the adjuvant induction Day 0. Two-way analysis of variance (ANOVA), followed by Tukey's post hoc test to ac-count for multiple comparisons, was used for data analysis using GraphPad Prism Software. (*, $P \leqslant 0.05$; **, $P \leqslant 0.01$; ***, $P \leqslant 0.001$; ****, $P \leqslant 0.0001$).

4.3.2 The polymers provides different protection of joint bone structure in AA rats

The most severe bone damage was found in the saline group, with extensive erosion of the entire distal tibia. P-Dex-A, P-Dex-C, P-Dex-D, and P-Dex-E treated animals demonstrated different level of reduced ankle bone erosion compared to the saline group. One month following the single dose polymer administration, there were only minor bone erosion found in P-Dex-A, P-Dex-C and P-Dex-E treated groups. The quantitative analysis of the hind paw calcaneus trabecular bone (Figure 4.2 A) micro-CT data showed that P-Dex-A, P-Dex-C and P-Dex-E treatment preserved the bone quality at different level (different P value compared with Saline control group), as is evident in the morphometric parameters, such as percent BV/TV, BS/TV, Tb.Sp, Tb.N, BMD, and Tb.Th, with their values similar to those observed for healthy controls, and significantly better than those observed for the free Dex-treated. When the entire calcaneus bone was analyzed (Figure 4.2 B), the P-Dex-D, Dex and saline groups were found with significantly increased calcaneus tissue volume, calcaneus total porosity and calcaneus bone surface and significantly decreased calcaneus bone volume percentage, when compared to the healthy and P-Dex-A, P-Dex-C and P-Dex-E treated groups.

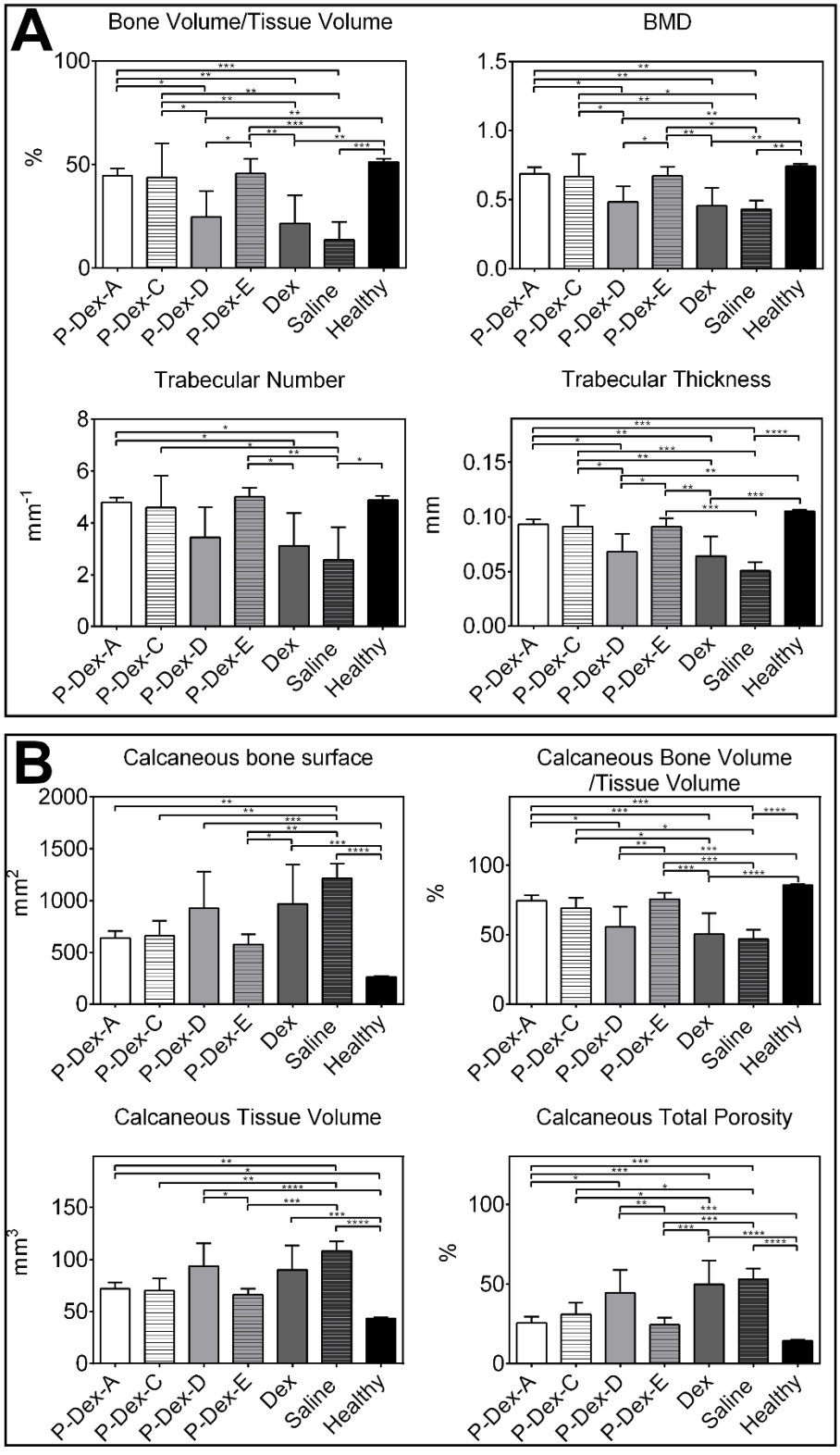
A
Bone Volume/Tissue Volume
%
BMD
Trabecular Number
mm-1
Trabecular Thickness
mm
B
Calcaneous bone surface
mm2
Calcaneous Bone Volume /Tissue Volume
%
Calcaneous Tissue Volume
mm3
Calcaneous Total Porosity
%
P-Dex-A
P-Dex-C
P-Dex-D
P-Dex-E
Dex
Saline
Healthy

Figure 4.2 Micro-CT analyses of the hind paw of the rats from different treatment groups. (B) Bone morphometric parameters of the trabecular bone ROI within calcaneus bone. (C) Bone morphometric parameters of the entire calcaneus bone. (*, $P \leqslant 0.05$; **, $P \leqslant 0.01$; ***, $P \leqslant 0.001$; ****, $P \leqslant 0.0001$).

4.4 Discussion

The HPMA polymer conjugates polymerized with different Dex-containing monomers synthesized in Chapter 2 were validated the difference therapeutic efficacy in this chapter. The adjuvant induced arthritis rats model were used for the proof-of-concept. The amelioration of the rats' ankles swelling which was measured daily showed different trend in the rats received different treatment on day 14 post-induction. It was found that the drug releasing rates may have significant impact on the drug therapeutic effect. For example, the significant joint amelioration of the P-Dex-C and P-Dex-E treatment was found from the following day post-injection on Day 15 compared with Saline treated group. This significance between P-Dex-E and Saline was found until the animals were sacrificed. However, the significance between P-Dex-C and Saline groups showed smaller from Day 31 (from P value <0.0001 to a higher P value), until Day 40 (26 days after injection) when significance can hardly be found in joints diameter data. This phenomena correlated with the fast Dex releasing profile of P-Dex-C than P-Dex-E, which can offer an immediate therapeutic effect but shorter sustention. This shorter sustention may also lead to a less protection of the bone structure than P-Dex-E showed in those Micro-CT data, such like trabecular bone percentage (Figure 4.2). When comparing P-Dex-A and P-Dex-E therapeutic efficacy using Saline as a control group, we could learn that the P-Dex-A treated animals started to show significant reduced joints diameter from Day 16 (the third day after injection), which is slower

than P-Dex-E, correlated with the Dex in vitro releasing profile that P-Dex-A released slower than P-Dex-E cannot offer as the same immediate anti-inflammatory effect as P-Dex-E. The joints diameter reduction significance of of P-Dex-A treatment compared with Saline treatment showed smaller than that P-Dex-C and P-Dex-E compared with Saline (bigger or equal P value in the comparison between P-Dex-A and Saline than it was between P-Dex-C and Saline or between P-Dex-E and Saline at the same day). In The fast releasing polymer (P-Dex-C) would show the faster therapeutic action (Figure 4.1), however, would also show an obvious disease activity flare which may because the active ingredient (Dex) in the macromolecular conjugates were less than its therapeutic concentration threshold. Insufficient dosage may not only cause the disease flare in the fast releasing drug treatment after a burst release, but also may cause the unobvious therapeutic outcome in the slow releasing treatment (P-Dex-D, which showed the slowest releasing rate in the pH 7.4). With the even slower releasing rate in the lysosomal acidic condition (pH 5.0), P-Dex-D showed a slight better improvement of the ankle joint protection than Saline treatment (joints' diameter significant smaller than those of Saline treated group on only Day 15, no significant bone structure protection was found in micro-CT analyses compared with Saline group). This may be the consequence of that slow-releasing may not offer enough therapeutic active ingredient at the inflammatory site. However, to different degree, the P-Dex-A and P-Dex-E showed a sustained protection for the rats' ankle. When approaching to the end of this animal study, the ankles from the rats received P-Dex-E showed a trend to start swelling, while the diameter of the ankles from the rats received P-Dex-A was

still decreasing although it was not significant compared with Saline treatment group because this animal model can self-recover. Considering in both pH7.4 and pH 5.0, P-Dex-A showed slower releasing rates than P-Dex-E, the results from the *in vivo* assessment was in agreement of the *in vitro* releasing study. P-Dex-E may show a better therapeutic efficacy when comparing the treatment of P-Dex-A and P-Dex-E at the same day post-treatment, at the same dosing level. However, to further conclude if P-Dex-E or P-Dex-A was the better therapeutic would need more evaluation on their effects on reduction the Dex side effect which may be done in the future and a fully dose escalation comparison study.

4.5 Conclusion

We proved the therapeutic efficacy was highly related to the macromolecular conjugates' releasing kinetics. We also provided the chemical structure guidance for the future drug designation for different releasing rate purpose of use.

CHAPTER 5

DESIGN, SYNTHESIS AND CHARACTERIZATION OF MACROMOLECULAR PRODRUG OF TOFACITINIB

5.1 Introduction

As an emerging class of medication, Janus kinase (JAK) inhibitors offer an alternative for RA patients who have experienced severe side effects or are refractory to current treatments. Tofacitinib (Tofa, CP-690 550), is a JAK inhibitor that exhibits functional selectivity for JAK1/3 and JAK1/2 signaling pathways. It was approved by the US Food and Drug Administration in 2012 for the treatment of adults with moderate-to-severe RA who have had an inadequate response or who are intolerant to methotrexate (MTX). Recent results from randomized clinical trials indicate that Tofa, used either as monotherapy [159-163] or in combination [164-167] with MTX or other non-biologic disease-modifying anti-rheumatic drugs (DMARDs) [168], leads to clinical improvement compared to placebo or MTX alone in patients with moderate-to-severe RA.

As a potent suppressor of innate and adaptive immunity, Tofa has been associated with dose-dependent toxicity, including higher risk of infections, malignancy, liver toxicity and hematologic abnormalities, which at least in part can be attributed to its the ubiquitous biodistribution [169]. We hypothesized that the development of a macromolecular prodrug of Tofa would modify its pharmacokinetics and biodistribution (PK/BD) pattern, favoring deposition in arthritic joints, which in turn could widen the drug's therapeutic window with sustained efficacy, providing the

opportunity for future development of safer Tofa dosing regimens. To test this hypothesis, a Tofa prodrug (P-Tofa) was synthesized by conjugating Tofa to a water-soluble, biocompatible *N*-(2-hydroxypropyl) methacrylamide (HPMA) copolymer via a hydrolysable carbamate linker (Figure 5.1).

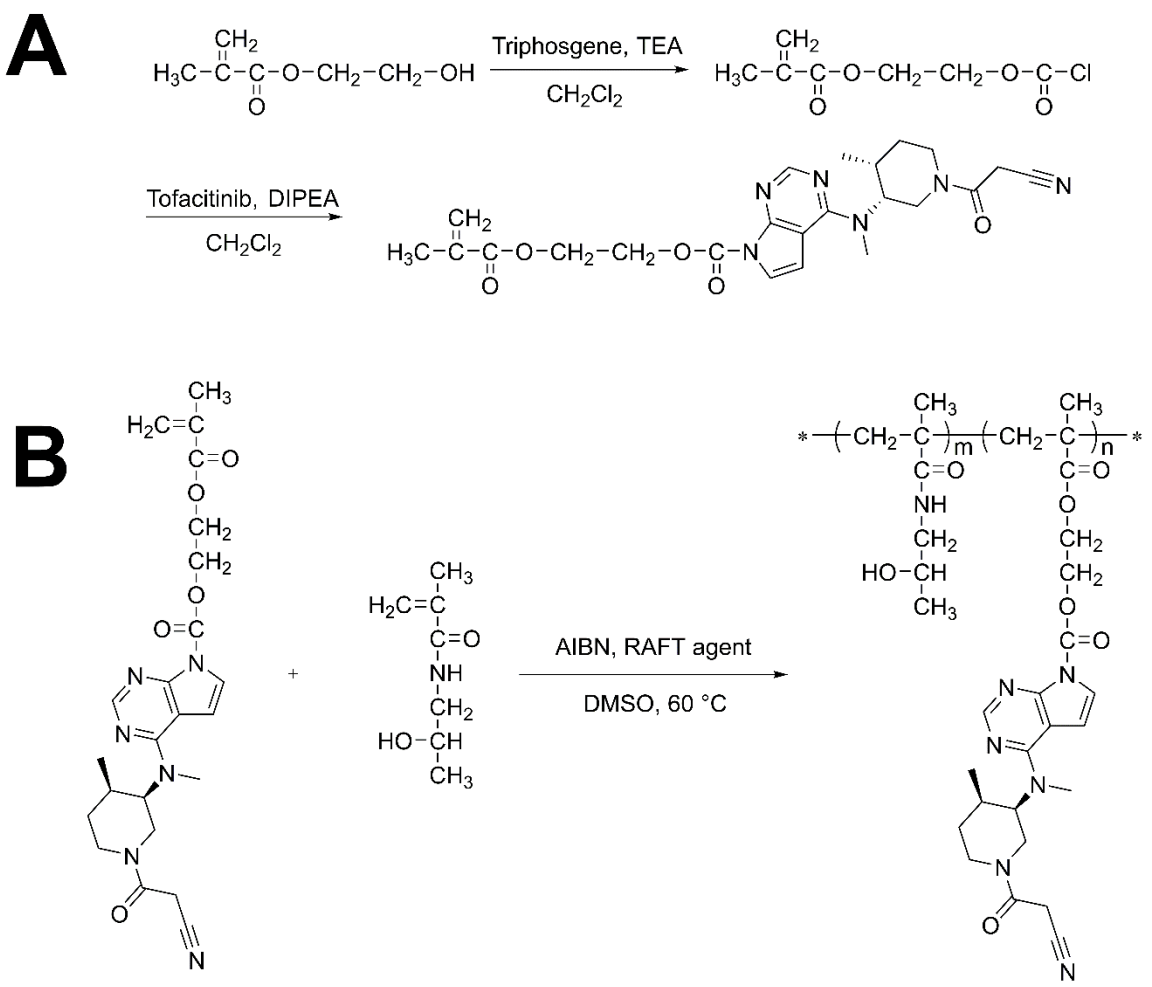

Figure 5.1 A macromolecular prodrug of Tofacitinib (P-Tofa). (A) The synthesis of HEMA-Tofa monomer; (B) The synthesis of P-Tofa.

5.2 Materials and Methods

5.2.1 Materials

N-(2-Hydroxypropyl) methacrylamide (HPMA), S,S′-bis(α,α′-dimethyl-α″-acetic acid)-trithiocarbonate, and *N,N*-dioctadecyl-*N″,N″*-bis(2-hydroxyethyl)-1,3-propanediamine (LA) were prepared as described in chapter 2. Tofacitinib and Tofacitinib citrate were purchased from JINLAN Pharm-Drugs Technology Co., Ltd (Hangzhou, China). IRDye® 800CW carboxylate was purchased from LI-COR, Inc. (Lincoln, NE, USA). Alexa Fluor® 647 NHS ester was purchased from Life Technologies, Inc. (Eugene, OR, USA). All other reagents and solvents, if not specified, were purchased from either Sigma-Aldrich (St. Louis, MO, USA) or Acros Organics (Morris Plains, NJ, USA). All compounds were reagent grade and used without further purification.

5.2.2 Instruments

^{1}H and ^{13}C NMR spectra were recorded on a 500 MHz NMR spectrometer (Varian, Palo Alto, CA, USA). The weight average molecular weight (Mw) and number average molecular weight (Mn) of copolymers were determined by size exclusion chromatography (SEC) using an ÄKTA FPLC system (GE HealthCare, Chicago, IL) equipped with UV and RI (KNAUER, Berlin, Germany) detectors. SEC measurements were performed on a Superdex 200 column (HR 10/30) with phosphate-buffered saline (PBS, pH=7.4) as the eluent. HPMA homopolymer (PHPMA) samples with narrow polydispersity were used as calibration standards. HPLC analyses were performed on an Agilent 1100 HPLC system (Agilent Technologies, Inc.,

Santa Clara, CA) with a Hypersil™ ODS C18 Columns (Thermo Scientific, Waltham, MA).

5.2.3 Synthesis of methacryloxyethyl chloroformate (HEMA-COCl)

Triphosgene (1710 mg, 5.7 mmol) in dichloromethane (4 mL, anhydrous) was added dropwise into a solution of hydroxyethyl methacrylate (HEMA, 500 mg, 3.8 mmol) and triethylamine (390 mg, 3.8 mmol) in dichloromethane (6 mL, anhydrous) maintained in an ice bath. The resulting mixture was stirred in the ice bath for 1 hr and then at room temperature for 1 hr. After removal of the solvent and excess phosgene using a rotary evaporator, the resultant white residue was extracted with dry ether (5 mL). The solid was filtered and the filtrate was concentrated to give HEMA chloroformate as colorless oil (715 mg, 96% yield).

^{1}H NMR (500 MHz, $CDCl_3$): δ = 6.16 (m, 1H, $=CH_2$), 5.64 (m, 1H, $=CH_2$), 4.56 (t, J = 4.5 Hz, 2H, $-CH_2-$), 4.42 (t, J = 4.5 Hz, 2H, $-CH_2-$), 1.96 (s, 3H, $-CH_3$); ^{13}C NMR (125.7 MHz, $CDCl_3$): δ = 166.89 (O-C=O), 150.86 (Cl-C=O), 135.59 (=C), 126.62 ($=CH_2$), 69.02 ($-CH_2-$), 61.51 ($-CH_2-$), 18.21 ($-CH_3$).

5.2.4 Synthesis of Tofa-containing monomer (HEMA-Tofa)

HEMA-COCl (370 mg, 1.92 mmol) in dichloromethane (5 mL, anhydrous) was added dropwise into a solution of Tofa (500 mg, 1.60 mmol) and diisopropylethylamine (DIPEA, 310 mg, 2.40 mmol) in dichloromethane (15 mL, anhydrous) maintained in an ice bath. The reaction mixture was stirred in the ice bath for 1 hr before quenching with water (10 mL). The organic layer was separated and washed with brine, then dried over anhydrous magnesium sulfate. After removal of the solvent,

the resulting light-yellow residue was subjected to flash column chromatography (CH_2Cl_2:CH_3OH = 20:1) to afford the monomer as a white solid (715 mg, 95% yield).

^{1}H NMR (500 MHz, $CDCl_3$): δ = 8.44 and 8.42 (s, 1H), 7.41 and 7.40 (d, J = 4.2 Hz, 1H), 6.64 and 6.58 (d, J = 4.2 Hz, 1H), 6.16 (s, 1H), 5.60 (s, 1H), 5.08 (br, 1H), 4.71 (t, J = 3.6 Hz, 2H), 4.54 (t, J = 3.6 Hz, 2H), 4.05 (dd, J_1 = 13.2, J_2 = 4.2 Hz, 0.5H), 4.07-3.45 (m, 6.5H), 3.33 (s, 3H), 2.51 and 2.46 (p, J = 6.1, 1H), 1.94 and 1.96 (s, 3H), 1.89-1.85 (m, 1H), 1.76-1.66 (m, 1H), 1.09 and 1.06 (d, J = 7.1 Hz, 3H); ^{13}C NMR (125.7 MHz, $CDCl_3$): δ = 167.05 (O-C=O), 160.82, 160.38, 157.61, 157.52, 153.04, 153.01, 148.87 (N-C=O), 135.78, 126.36, 126.24, 121.60, 121.44, 114.33, 114.12, 106.21, 105.99, 105.17, 65.16, 65.06, 62.20, 61.98, 53.86, 53.58, 46.71, 43.74, 42.76, 39.48, 35.21, 34.75, 31.48, 31.22, 29.66, 25.20, 25.15, 18.25, 18.29 (CH_3), 14.25, 14.10. ESI-MS: $[M+H]^+$ = 468.8.

5.2.5 Synthesis of HPMA copolymer-Tofa conjugate (P-Tofa) via RAFT copolymerization

HPMA (3712 mg, 22.47 mmol) and HEMA-Tofa (750 mg, 1.60 mmol) were dissolved in anhydrous dimethyl sulfoxide (DMSO, 21 mL) with 2,2′-azobisisobutyronitrile (AIBN, 37.7 mg, 0.17 mmol) as initiator and *S*,*S*′-bis(*α*, *α*′-dimethyl-*α*″-acetic acid)-trithiocarbonate (CTA, 33.7mg, 0.13 mmol) as the RAFT agent. The solution was purged with argon and polymerized at 60 °C for 40 hr. The resulting polymer was first purified by precipitation in acetone/diethyl ether (v/v = 1:1, 200 mL) twice to remove the unreacted low molecular weight compounds, and then dialyzed against ddH_2O. The molecular weight cutoff size of the dialysis tubing

was 25 kDa of globular protein. The resulting solution was then lyophilized to afford the final P-Tofa (4.21 g).

To quantify Tofa loading, P-Tofa (1 mg/mL) was hydrolyzed in 0.01 N NaOH in CH_3OH overnight. The resulting solution was neutralized and analyzed with HPLC (mobile phase: acetonitrile/water = 3/1; detection, UV 284 nm; flow rate = 1 mL/min; injection volume = 20 μL). The analyses were performed in triplicate. The mean value and standard deviation were obtained with Microsoft Excel.

5.2.6 The synthesis of P-Tofa-APMA

To introduce fluorescent labels to the P-Tofa for biodistribution and immunofluorescence analysis, primary amine was introduced into P-Tofa using the following procedure: HPMA (700 mg, 4.89 mmol) and HEMA-Tofa (142 mg, 0.3 mmol) were dissolved in anhydrous dimethyl sulfoxide (DMSO, 6 mL), *N*-(3-aminopropyl) methacrylamide hydrochloride (APMA, 9.5 mg, 0.05 mmol), 2,2′-azobisisobutyronitrile (AIBN, 7.11 mg, 0.04 mmol) as initiator and *S*,*S*′-bis(*α*, *α*′-dimethyl-*α*″-acetic acid)-trithiocarbonate (CTA, 6.79mg, 0.02 mmol) as the RAFT agent, placed in an ampule, and purged with argon and polymerized at 60 °C for 40 hr. The resulting polymer was first purified by precipitation in acetone/diethyl ether (v/v = 1:1, 200 mL) twice to remove the unreacted low molecular weight compounds, and then dialyzed against ddH_2O. The amine content of the copolymer was determined as 3.56×10^{-5} mol/g using the ninhydrin assay.

5.2.7 The synthesis of P-Tofa-IRDye

To monitor its distribution after systemic administration, P-Tofa was labeled with IRDye® 800CW. The labeling procedure is briefly described as follows: IRDye® 800CW carboxylate (1.25 mg, 1.1 μmol), *N*-(3-dimethylaminopropyl)-*N*'-ethylcarbodiimide hydrochloride (EDC, 1.56 mg, 8.1 mmol) and hydroxybenzotriazole (HOBt, 0.49 mg, 3.6 mmol) were dissolved in *N*,*N*-dimethylformamide (DMF, 1 mL) in dark at 21 °C and stirred for 30 min. DIPEA (7 mg, 0.054 mmol) and P-Tofa-APMA (50 mg, $[NH_2]$ = 1.78 μmol) in DMF (1 mL) were added into the reaction mixture and then stirred overnight. The reaction solution was dialyzed to remove DMF and low molecular weight reactants. P-Tofa-IRDye was then obtained via lyophilization with [IRDye® 800CW] = 6.88×10^{-6} mol/g of the conjugate.

5.2.8 The synthesis of P-Tofa-Alexa

To monitor the cellular sequestration of the P-Tofa in the rat after systemic administration, P-Tofa was labeled with Alexa Fluor® 647. The labeling procedure is briefly described as follows: Alexa Fluor™ 647 NHS Ester (1 mg, 0.8 μmol), DIPEA (3.5 mg, 0.027 mmol) and P-Tofa-APMA (50 mg, $[NH_2]$ = 1.78 μmol) were dissolved in *N*,*N*-dimethylformamide (DMF, 1 mL) in dark at 21 °C and stirred overnight. The reaction solution was dialyzed to remove DMF and low molecular weight reactants. P-Tofa-IRDye was then obtained via lyophilization with [50] = 5.62×10^{-6} mmol/g of the conjugate.

5.2.9 *In vitro* Tofa release from P-Tofa

P-Tofa conjugates (~ 3 mg) were dissolved in 5 mL of buffer solutions with 0.2% sodium dodecyl sulfate (SDS, to create the “sink” condition) and different pH values (pH=7.4, pH=5.5, pH =10), and rats’ serum (Invitrogen). The release experiments were conducted in a shaking water bath (37 °C, shaking rate 20 rpm). Hydrolysis samples (400 µL) were withdrawn at designated time points. The released Tofa was extracted with ethyl acetate (1200 µL), with a recovery rate at 94.3±0.48%. The solution of Tofa (300 µL) was subsequently dried using a centrifugal evaporator. The sample was then stored at -80 °C for HPLC analysis as described above.

5.3 Results

5.3.1 Characterization of P-Tofa

P-Tofa has a weight average molecular weight (M_w) of 30.4 kDa, a number average molecular weight (M_n) of 23 kDa and a polydispersity index (PDI) of 1.32, representing a narrow polydispersity. The Tofa drug loading in P-Tofa was found to be ~ 13 wt%. The *in vitro* Tofa release rate was found to be highly dependent upon buffer pH values (Figure 5.2). Both acidic and basic pH environments accelerated Tofa release, when compared to the release rate at pH 7.4. The presence of serum proteins in the releasing medium was also found to increase the Tofa release rate. Under each condition tested, intact Tofa was gradually released from P-Tofa. Interestingly, Tofa degradation was observed over time in the basic buffer (pH 10), which is in agreement with previous findings [170]. During the course of

the experiment (20 days), the release rates of Tofa from P-Tofa at pH = 5.5 and 7.4, in the rat serum averaged at ~1.5%, 2% and 2.5% of the loaded drug per day, respectively.

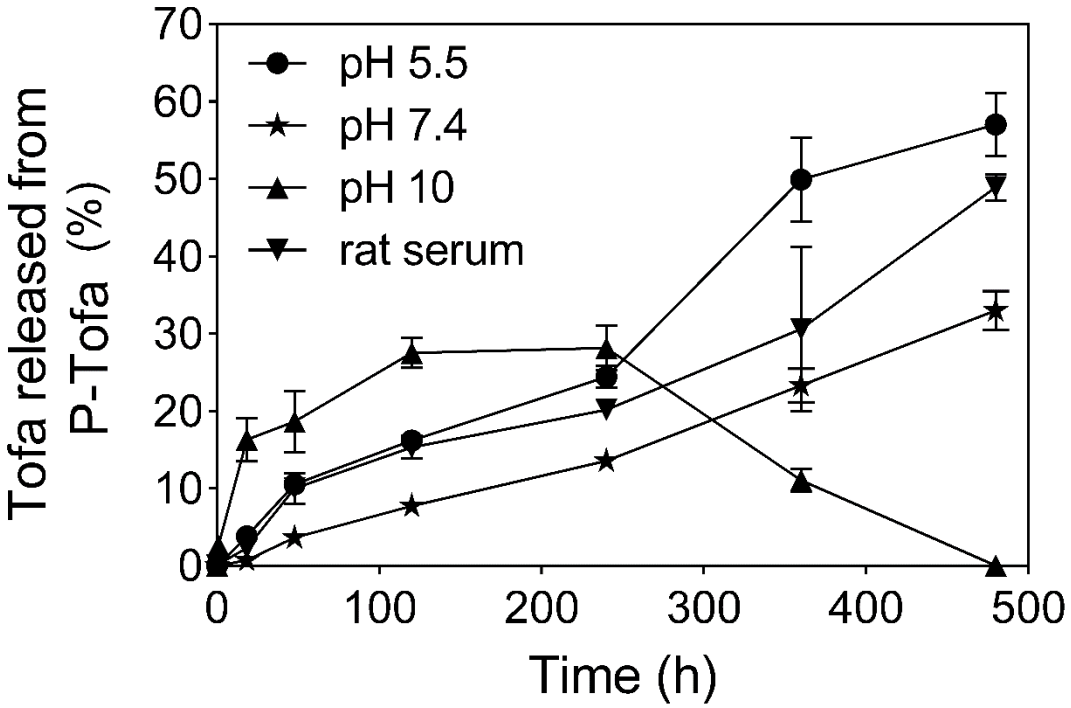

Figure 5.2 *In vitro* Tofa release from P-Tofa at pH = 5.0, 7.4, 10.0 and in rat serum. The mean values and standard deviation were calculated with GraphPad Prism, n = 3.

5.4 Discussion

In recent years, significant progress has been made in understanding the essential role of specific proinflammatory cytokines and other immunological processes responsible for RA initiation and progression [17, 171]. Subsequent

studies showed that the receptors for several proinflammatory cytokines exert their effects through the activation of intracellular signaling pathways mediated by a unique family of Janus kinases that phosphorylate downstream molecular targets that control key inflammatory and immunological processes [172, 173]. This led to the development of Tofacitinib (Tofa, CP-690 550), the first selective JAK inhibitor tested in humans. Tofa inhibits both JAK3 and JAK1, to a lesser extent JAK2, and was found to be effective in disease suppression in a variety of clinical conditions and experimental models ranging from inflammatory arthritis, autoimmune disorders and transplantation. A major challenge in the development of JAK inhibitors for the treatment of inflammatory and autoimmune disorders has been their ubiquitous expression in multiple tissues and cell types, and the broad range of biological activities that they control. Thus, despite demonstrated efficacy in RA, their systemic administration is associated with many serious and potentially life threatening adverse side effects, including infections, malignancy, liver toxicity and hematologic abnormalities [169]. We hypothesized that selective targeting of Tofa to sites of joint inflammation might substantially enlarge the therapeutic window of Tofa, with the potential for an improved safety profile. We have previously shown in animal models that the macromolecularization of glucocorticoids significantly potentiates their therapeutic efficacy and reduces systemic toxicities [146, 147, 174, 175], via a unique targeting pattern of macromolecular prodrugs based on the ELVIS mechanism (***E***xtravasation through ***L***eaky ***V***asculature and ***I***nflammatory cell-mediated ***S***equestration), in which the systemically administered prodrug ex-

travasates through the leaky vasculature at the inflammatory lesion and is sequestered locally via inflammatory cell infiltrates and activated resident cells [134]. Concurrently, for systemic inflammatory conditions, a fraction of the nanomedicine administered may also be sequestered by circulating white blood cells (WBC) and be actively transported to the inflammatory lesion.

Based upon these previous studies, we hypothesized that a macromolecular Tofacitinib prodrug would selectively target inflamed joints, followed by sequestration in resident cells and activation to release Tofa locally to suppress joint inflammation. Our initial attempt to conjugate Tofa to HPMA copolymer was challenging. The secondary amine in the pyrrole ring is the only available site for chemical conjugation. Given the regional pyrrole/pyrimidine-conjugation, this amine is not very reactive. Attempts to conjugate Tofa to HPMA copolymer via peptides or citraconic acid linkers failed. Eventually, Tofa was successfully conjugated to HEMA via a carbamate bond and the Tofa-containing monomer was copolymerized with HPMA (Figure 5.1A and 5.1B). We purposely set the P-Tofa molecular weight (~ 30 kDa) lower than the glomerular filtration threshold of 45 kDa of HPMA copolymer to allow eventual renal clearance of the prodrug. There was an initial concern regarding the use of a carbamate linker as it has been known to be relatively stable *in vivo*. The *in vitro* release study (Figure 5.2), however, provided strong evidence that the prodrug can be gradually activated under acidic environments (e.g. inflammatory acidosis or lysosomal pH).

5.5 Conclusion

In this study, we have developed a macromolecular prodrug of a Janus Kinase (JAK) inhibitor, Tofacitinib (P-Tofa) using a well-established, water-soluble and bi-ocompatible *N*-(2-hydroxypropyl) methacrylamide (HPMA) copolymer.

CHAPTER 6

IN VITRO AND IN VIVO EVALUATION OF TOFACITINIB PRODRUG THERAPEUTIC EFFICACY AND REDUCTION OF TOXICITY

6.1 Introduction

Rheumatoid arthritis (RA) is a chronic, inflammatory disorder that affects up to 1% of adults worldwide [176, 177]. The disease often leads to significant pain associated with progressive articular damage. At present, there is no cure for RA [9, 178]. The identification of the key role of intracellular kinase signaling pathways in the regulation of proinflammatory cytokines and immune cell activation has led to the recent development of orally available low molecular weight drugs that selectively target individual members of the Janus kinase pathway [172].

As discussed in Chapter 5, we successfully synthesized Tofa prodrug (P-Tofa). To further investigate this prodrug, the therapeutic efficacy and potential toxicities of P-Tofa were evaluated in an adjuvant-induced arthritis (AA) rat model.

6.2 Materials and Methods

6.2.1 Instruments

Histology slides were scanned with a VENTANA iScanner HT (Tucson, AZ, USA). Bone quality were analyzed using a Skyscan 1172 high resolution micro-CT system (Skyscan, Kontich, Belgium). A Faxitron® MX-20 Cabinet X-ray System (Tucson, Arizona, USA) was used to monitor the hard tissue decalcification progress. A Leica RM2255 rotary microtome (Leica Biosystems Inc., Buffalo Grove, IL, USA) was used for paraffin-embedded tissue sectioning. Tissue slides were

analyzed using a ZEISS LSM 800 confocal microscope (Carl Zeiss Microscopy, LLC, Peabody, MA, USA). Live animals were imaged using Xenogen IVIS® Spectrum *in vivo* imaging system (PerkinElmer Inc., Waltham, MA, USA).

6.2.2 Treatment of adjuvant-induced arthritis (AA) rats

As described previously [146], male Lewis rats (175-200 g) from Charles River Laboratories (Wilmington, MA, USA) were used to establish the adjuvant-induced arthritis (AA) rat model. The established AA rats were then divided into 3 groups: P-Tofa treatment (n = 10, single i.v. injection on day 14 post-induction, dose equivalent of Tofa = 130.2 mg/kg), Tofa treatment (n=10, Tofa was suspended in 0.5% methylcellulose/0.025% Tween 20 (Sigma), once daily oral gavage for 21 days from day 14 post-induction, 6.2 mg/kg/day) [179], and saline control (n=8). An additional group (n=5) of healthy rats were used as a negative control. Joint inflammation and body weight were monitored daily from day 11. Hematology profiles including absolute count of white blood cells (WBC), neutrophils (NE), lymphocytes (LY), monocytes (MO), eosinophils (EO) and basophils (BA) were analyzed using an HEMAVET 950 FS Hematology System (Drew Scientific Inc., Miami Lakes, FL, USA) every week post treatment initiation until the last date of free Tofa treatment. Blood was collected for liver enzyme analysis at necropsy. Liver function including alanine aminotransferase (ALT), aspartate aminotransferase (AST), and alkaline phosphatase (ALP) were analyzed using a DTX 880 Multimode Detector (Beckman Coulter, Jersey City, NJ, USA) at UNMC clinical test lab. All major organs were collected at the euthanasia and fixed with buffered formalin before paraffin embedding. Tissue sections (5 μm) were processed and

H&E stained for histological evaluation by a pathologist (SML), who was blinded to the treatment group arrangement. All animal experiments were performed in accordance with protocols approved by the Institutional Animal Care and Use Committee (IACUC) of the University of Nebraska Medical Center or Hospital for Special Surgery.

6.2.3 Observational assessment of AA rats' joint inflammation

The articular index (AI) score was recorded during the treatment by the same observers (XW and GZ) as described previously [146]. An AI score was given to each hind limb from day 11 to day 56 post-arthritis induction. The AI scoring system is based on a 0-4 numeric system as the following: 0 = no signs of swelling or erythema; 1 = slight swelling and/or erythema; 2 = low-to-moderate edema and signs involving the tarsals; 3 = pronounced edema with limited use of the joint and signs extending to the metatarsals; 4 = excessive edema with joint rigidity and severe signs involving the entire hind paw. The sum of the two hind limb scores for each animal was recorded. Ankle diameter (medial to lateral) was measured using a digital caliper as confirmation of inflammation-associated edema/hyperplasia.

6.2.4 Micro-CT analysis of articular bone quality

Hind limbs were isolated after euthanasia and fixed with buffered formalin for no less than 48 hr. The left ankle joint bone quality was analyzed using a Skyscan 1172 micro-CT system. Micro-CT scanning parameters were set as follows: voltage, 70 kV; current, 142 μA; exposure time, 3650 ms; resolution, 13.1 μm; with

aluminum filter (0.5 mm); rotation step = 0.4°; frame averaging = 6; random movement = 10; using 360° rotation scanning. Raw data were reconstructed using NRecon to obtain a visual representation of the results, and the volume rendering of the samples were performed via CTvox software (Skyscan). To quantitatively compare the four treatments, the entire calcaneus and the selected region of interest (ROI) of the trabecular bone within the calcaneus (Figure 6.1) were used as the anatomical sites for micro-CT analyses. The ROI was defined by aligning the calcaneus bone along the sagittal plane using Dataviewer, with the ROI starts at the 75^{th} slide away from the epiphyseal plate and continues for 76 slides (1.98 mm). The diameter of the cylindrical ROI was set at 1.00 mm. The morphometric parameters, such as percent bone volume (BV/TV), bone surface density (BS/TV), trabecular separation (Tb.Sp), trabecular number (Tb.N), bone mineral density (BMD), and trabecular thickness (Tb.Th) were calculated using CTAn (Skyscan).

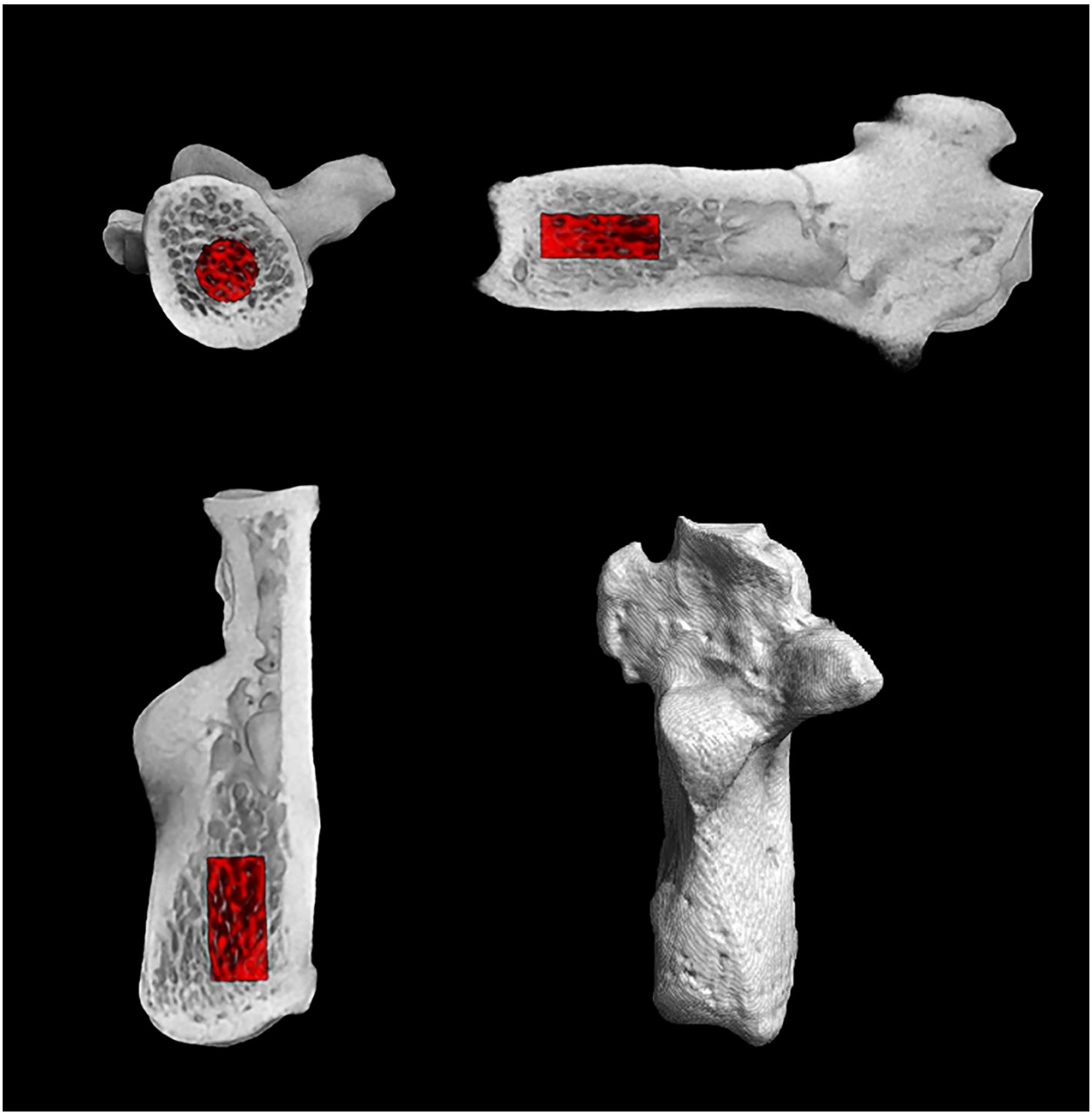

Figure 6.1 Region of interest in micro-CT analyses. Gray color: rat calcaneus bone; Red color: cylindrical ROI within the calcaneus bone.

6.2.5 Joint tissue histological evaluation

Right hind limbs were decalcified using 5% formic acid after fixation for histological analyses. Upon complete decalcification, the tissues were paraffin-embedded, sectioned (8 μm) approximately 200 μm apart, then H&E and Safranin O stained. Stained sections were histologically graded by a pathologist (SML), who was blinded to treatment groups [146], and then scanned using a high-throughput bright-field slide scanner. Each histopathologic feature was graded as follows: synovial cell lining hyperplasia (0 to 2); pannus formation (0 to 3); mononuclear cell infiltration (0 to 3); polymorphonuclear leukocytes infiltration in periarticular soft tissue (0 to 3); cellular infiltration and bone erosion at the distal tibia (0 to 3); and cellular infiltration of cartilage (0 to 2). Scores for all of the histopathologic features were summed for each animal.

6.2.6 P-Tofa biodistribution

P-Tofa was labeled with IRDye® 800CW (P-Tofa-IRDye) and administered i.v. to AA rats (n=5) on day 14 post-induction. Rats were then imaged with a Xenogen IVIS® Spectrum *in vivo* system under anesthesia at designated time points. The images were captured with the following conditions: Excitation: 778 nm (Filter: 745 nm); Emission: 794 nm (Filter: 800nm); exposure times: 2 s; Field of View: 24.5 cm; Binning Factor: 8; f Number: 2. The captured images were then analyzed using the Living Image 4.5 software (PerkinElmer Inc.). For *ex vivo* organ distribution analyses, P-Tofa-IRDye was administered i.v. to AA rats (n=3 per time point) on day 14 post-induction. Rats were perfused and euthanized at the designated time points. Major organs were then collected and imaged using a Pearl® Impulse

small animal imaging system (LI-COR, Lincoln, NE, USA). The image acquiring conditions were set as dual channels (800 nm and white light) with 85 μm resolution. The images for each rat were obtained using the same intensity scale with a common minimum and maximum value.

6.2.7 Immunohistochemically analysis of P-Tofa's cellular uptake within ankle joints

Alexa Fluor® 647-labeled P-Tofa (P-Tofa-Alexa) was administered i.v. to AA rats (n=5) on day 14 post-induction. Twenty-four hours later, rats were perfused and euthanized. Hind limbs were collected, fixed and decalcified using 14% EDTA solution (pH=7.4), paraffin embedded, sectioned (20 μm). The slides were immunohistochemically stained with the following antibodies: mouse anti-rat CD68 (Bio-Rad, MCA341R, dilution 1:100) and rabbit anti-rat P4HB (Abcam, ab85564, dilution 1:50), respectively, overnight at 4 °C after antigen retrieval using sodium citrate buffer and blocked using 10% normal goat serum. Slides incubated with mouse anti-rat CD68 were further incubated with Alexa Fluor 488-labeled goat anti-mouse secondary antibody (Thermo Fisher scientific, A11001, dilution 1:1000) and slides incubated with rabbit anti-rat P4HB were incubated with Alexa Fluor 488-labled goat anti-rabbit secondary antibody (Thermo Fisher scientific, A11008, dilution 1:1000) for another 1 hr at 21 °C in the dark. The stained slides were imaged using a ZEISS LSM 800 confocal microscope after mounted in ProLong® Gold antifade mountant with DAPI (Thermo Fisher scientific, P36931, Waltham, MA).

6.2.8 *In vitro* macrophage cell culture.

Primary bone marrow macrophages (BMMs) were isolated from 6-8 week old C57BL/6 mice [180]. BMMs were treated with Tofa (1 μM) or P-Tofa (Tofa equivalent = 16.1 μM) for 1 hr, after which 0.04 ng/mL, and 0.2 ng/mL of IL-4 was added for 24 hr. For "washout" experiments, a similar procedure was followed, except the P-Tofa/Tofa incubation time was increased to 24 hr, following which the cells were washed and incubated with fresh medium (without P-Tofa or Tofa) for 72 hr or 1 week, prior to the IL-4 challenge. RNA was isolated using RNAeasy kits (Qiagen, Redwood City, CA), in accordance with manufacturer's recommendations and reverse transcribed using the Maxima First Strand cDNA Synthesis Kit for RT-qPCR (Thermo Scientific, Waltham, MA, USA). Real-time qPCR was performed using the Maxima SYBR Green/Fluorescein qPCR Master Mix 2X (Thermo Scientific, Waltham, MA, USA) on a CFX96 real time thermocycler (Bio-Rad, Hercules, CA, USA) and the relative gene expression was measured using the standard ΔΔCq method and normalized to mouse GAPDH expression. Arg1, Ym1/2 and Fizz1 and their respective sequences are listed as follows:

Arg1 (GGAATCTGCATGGGCAACCTGTGT/AGGGTCTACGTCTCGCAAGCCA),

Ym1/2 (GGGCATACCTTTATCCTGAG/CCACTGAAGTCATCCATGTC),

Fizz1 (TCCCAGTGAATACTGATGAGA/CCACTCTGGATCTCCCAAGA),

GAPDH (GGTGCTGAGTATGTCGTGGA/GTGGTTCACACCCATCACAA)

6.2.9 Serum cytokine measurements

CXCL10 protein levels in rat serum samples collected weekly from day 14 to day 56 were quantified by ELISA (Abnova, Rat CXCL10 ELISA Cat #KA2203, Taipei City, Taiwan). The assay was performed in duplicate using a two-fold dilution of serum according to the manufacturer's instruction.

6.2.10 Statistical methods

One-way analysis of variance (ANOVA), followed by Tukey's post hoc test to account for multiple comparisons, was used for data analysis using GraphPad Prism Software. P-values ≤ 0.05 were considered statistically significant.

6.3 Results

6.3.1 P-Tofa provides sustained amelioration of joint inflammation in AA rats.

Ankle diameter and AI score of the Tofa-treated group exhibited a continuous decrease from day 15 to 34 post-arthritis induction, with an immediate flare upon cessation of oral Tofa on day 35 (Figure 6.2). A single injection of P-Tofa (dose equivalent to the entire Tofa treatment) resulted in greater reductions in ankle swelling and AI score from day 15 to 34, a difference that persisted to day 56. The ankle diameter of the P-Tofa group was significantly lower ($P < 0.05$) than both the Tofa group and saline group from day 14 to day 56; and significantly higher ($P < 0.05$) than the healthy control group from day 11 to day 56. No significant differences were found between the Tofa and saline groups except day 16 to day 22.

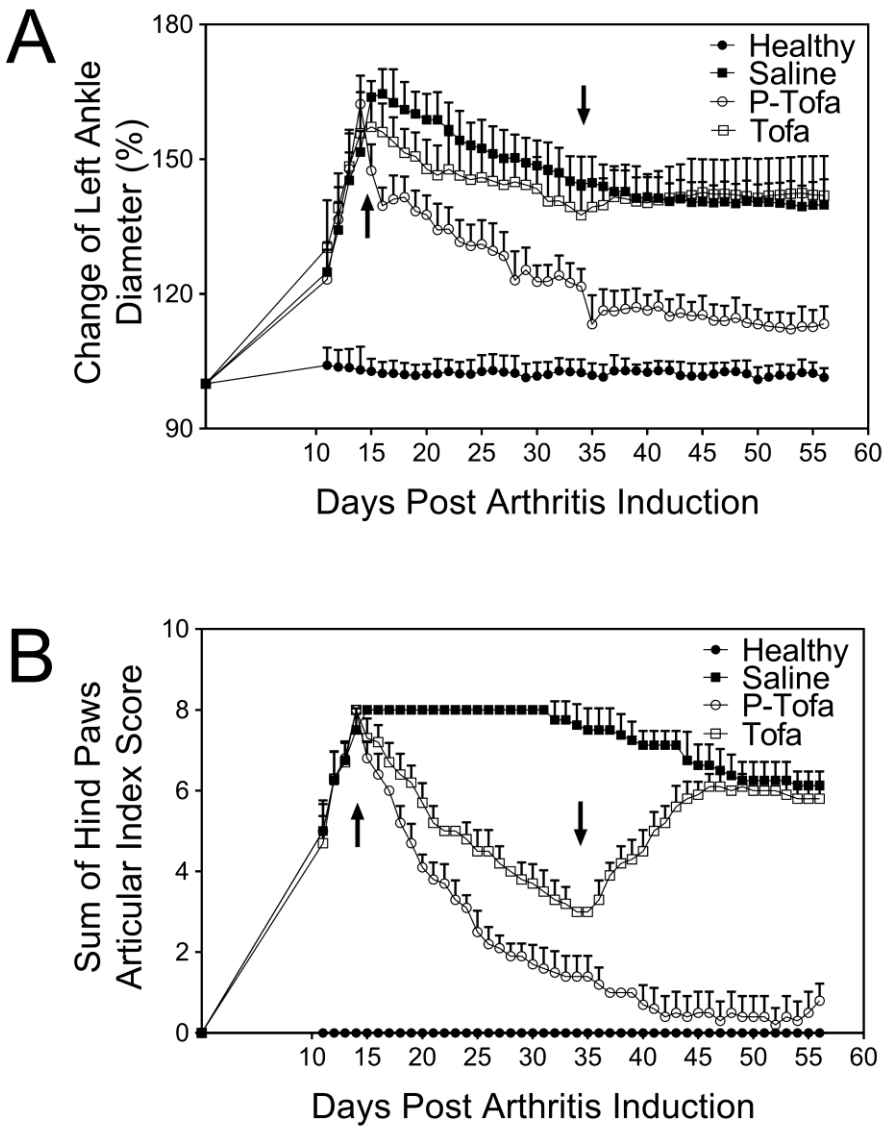

Figure 6.2 P-Tofa can effectively amelioration of joint inflammation in an adjuvant-induced arthritis (AA) rat model. (A) The change of AA rats' left ankle joint size of different groups during the treatment study; (B) The change of articular index score of different groups during the treatment study. The arrow pointing up indicates the day when rats received the single P-Tofa injection and the daily oral Tofa treatment was initiated. The arrow pointing down indicates the day when rats received their

last oral Tofa treatment. The prevention of arthritic ankle swelling by single injection of P-Tofa was sustained for 6 weeks from day 15 to day 56.

6.3.2 Histological Analysis of the Ankle Joints.

Compared to healthy control animals, histological analyses revealed marked bone and cartilage destruction of the distal tibia, calcaneus and talus joints in the saline-treated group, with periosteal expansion and inflammatory cell infiltration. The Tofa-treated group exhibited histological findings similar to the saline group, consistent with a limited capacity in preventing joint bone erosion and cartilage damage. The single dose P-Tofa group, however, displayed markedly reduced joint damage and cellular infiltration, with bone and cartilage morphology maintained similar to that of the healthy rats (Figure 6.3A, 6.3B). The sum of the score from each animal was recorded and shown in Figure 6.3C. The statistically significant difference was found between Healthy vs. Saline, Saline vs. P-Tofa and P-Tofa vs. Tofa groups. No significant difference was found between P-Tofa vs. Healthy or Saline vs. Tofa groups.

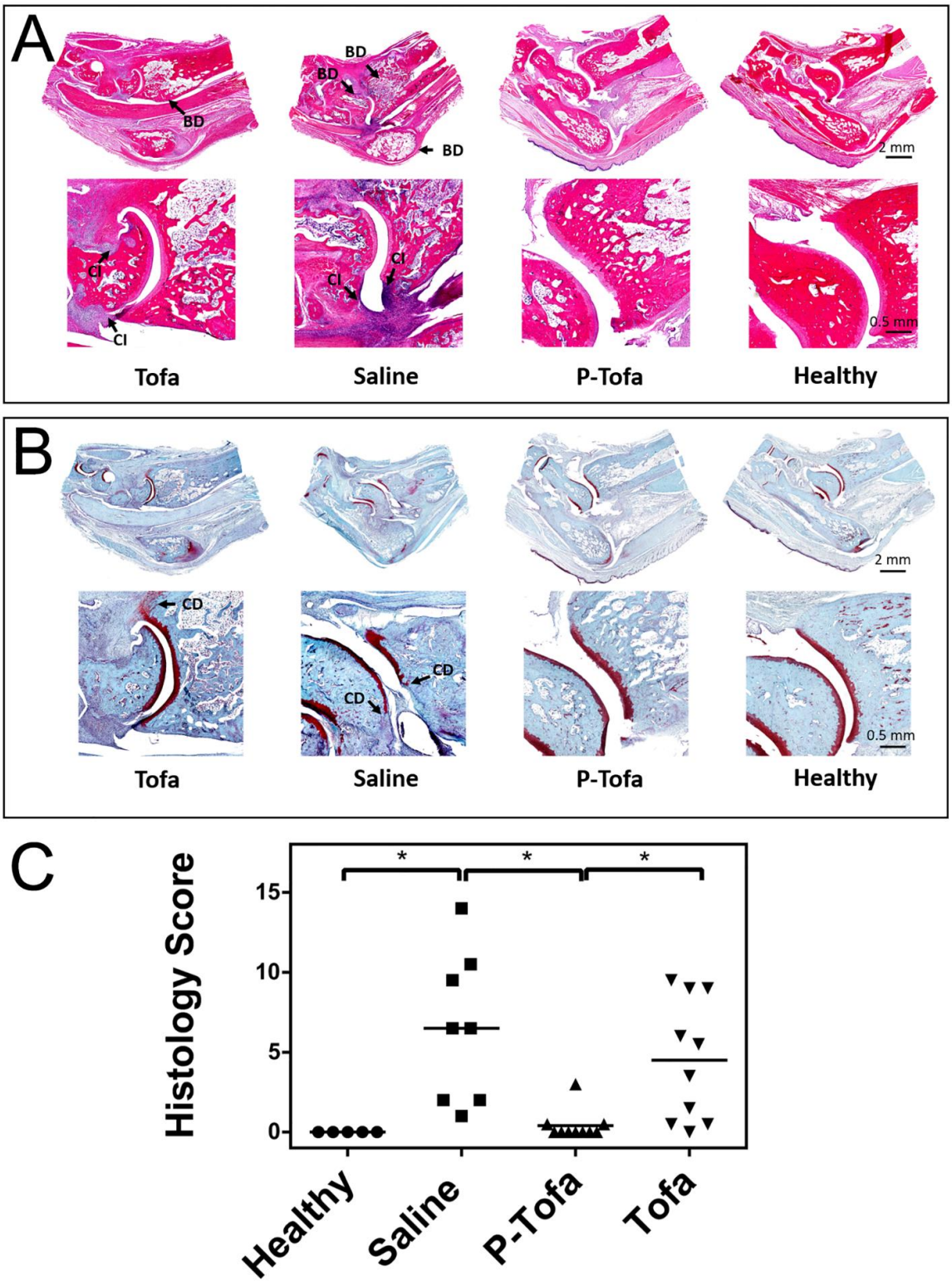

Figure 6.3 Histology evaluation of Tofa and P-Tofa therapeutic efficacy. (A) H&E-stained joint sections (10× and 40×). Cellular infiltration in periarticular soft tissue,

bone and cartilage damage in Tofa and saline groups; (B) Safranin O-stained joint sections (10× and 40×). Ta, talus; Ti, tibia; CD, cartilage damage; CI, cell infiltration; BD, bone damage; (C) Semi-quantitative comparisons of histology scores of all treatment groups (*, $P \leq 0.05$, ANOVA).

6.3.3 Micro-CT evaluation of joint bone quality

The most severe bone damage was found in the saline group, with extensive erosion of the entire distal tibia (Figure 6.4A). Tofa-treated animals demonstrated reduced ankle bone erosion compared to the saline group. Six weeks following the single dose P-Tofa administration, there was only minor bone erosion. The quantitative analysis of the hind paw calcaneus trabecular bone (Figure 6.4B) micro-CT data shows that P-Tofa treatment preserved the bone quality as evident in the morphometric parameters, such as percent bone volume (BV/TV), bone surface density (BS/TV), trabecular separation (Tb.Sp), trabecular number (Tb.N), bone mineral density (BMD), and trabecular thickness (Tb.Th) with their values similar to those observed for healthy controls; and significantly better than those observed for free Tofa-treated and the saline control. When the entire calcaneus bone was analyzed (Figure 6.4C), the Tofa and saline groups were found with significantly increased calcaneus tissue volume and calcaneus bone surface, and significantly decreased calcaneus bone volume percentage, when compared to the healthy and P-Tofa-treated groups.

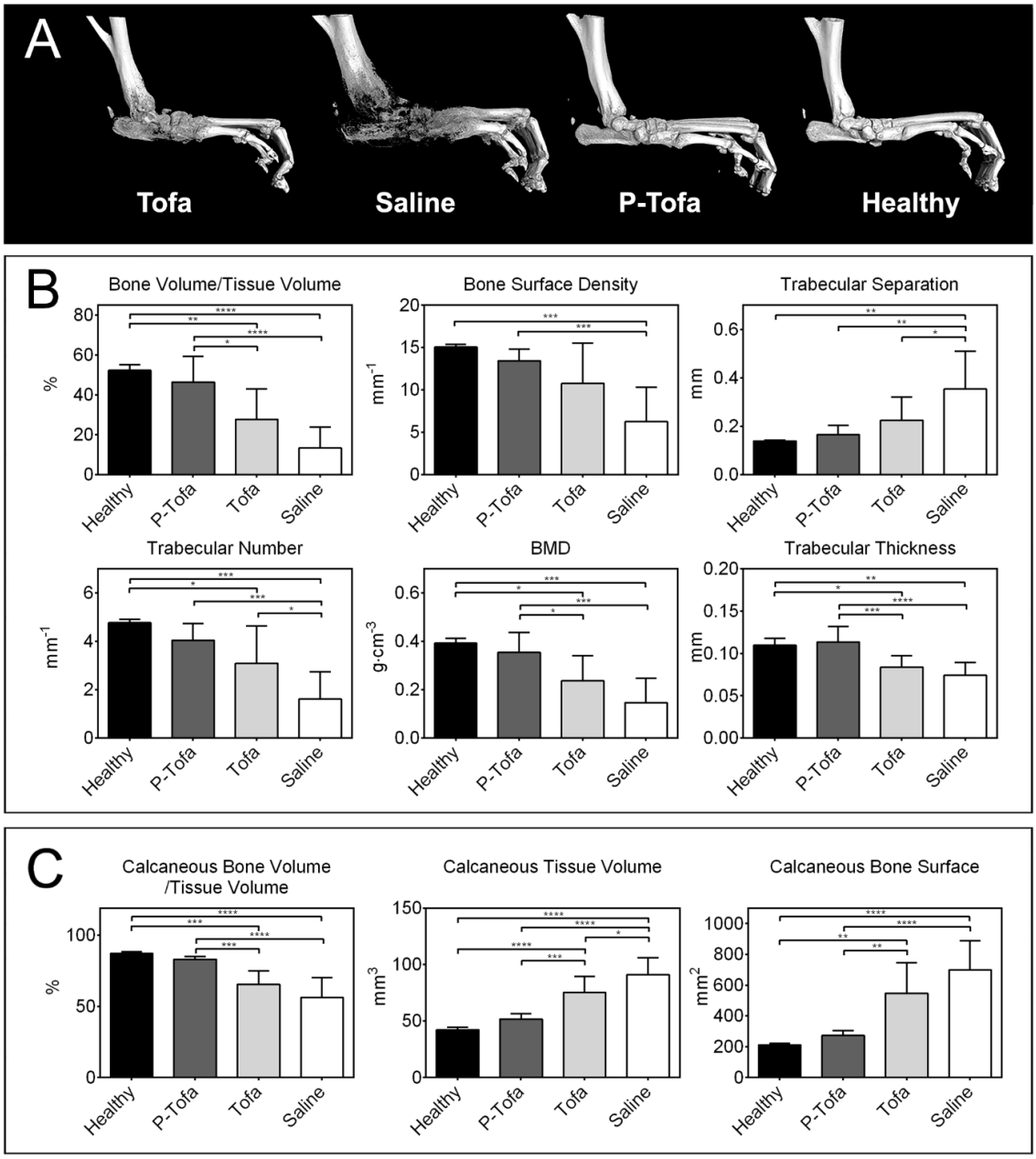

Figure 6.4 Micro-CT analyses of the hind paw of the rats from different treatment groups. (A) Representative 3-D reconstructed ankle joints from each treatment group. P-Tofa-treated rats were most similar structurally to the healthy group, while saline group exhibited extensive bone erosion. Significant bone damage was also found in the Tofa treated animals; (B) Bone morphometric parameters of the

red cylinder ROI within calcaneus bone as shown in Figure 6.1; (C) Bone morphometric parameters of the entire calcaneus bone. No significant difference between the healthy and P-Tofa treated rats was found for all the parameters, indicative of the potent joint preservation capacity of the single dose P-Tofa treatment. (*, $P \leq 0.05$; **, $P \leq 0.01$; ***, $P \leq 0.001$; ****, $P \leq 0.0001$)

6.3.4 Passive targeting and retention of P-Tofa in arthritic joints

Near infrared optical imaging analyses revealed that systemically administered P-Tofa-IRDye was mainly distributed to arthritic joints (Figure 6.5A). Signals observed at the ear and the base of the tail were attributed to the trauma from ear tag installation and inflammation associated with immunization. Signal intensity in the joints gradually decreased from ~1×10^9 to ~2×10^8 (p/sec/cm^2/sr)/(uW/cm^2) over 12-days. To validate live imaging results, major organs and both hind limbs were collected at necropsy and imaged *ex vivo*. The inflamed joints, especially the hind limb ankle joints, were the major sites of P-Tofa-IRDye distribution with moderate-to-high signal intensity also observed in the liver and kidneys (Figure 6.5B). The lack of fluorescent signal observation confirmed the absence of P-Tofa in the other organs. Semi-quantitative analyses of the optical imaging data corroborated this observation (Figure 6.5C).

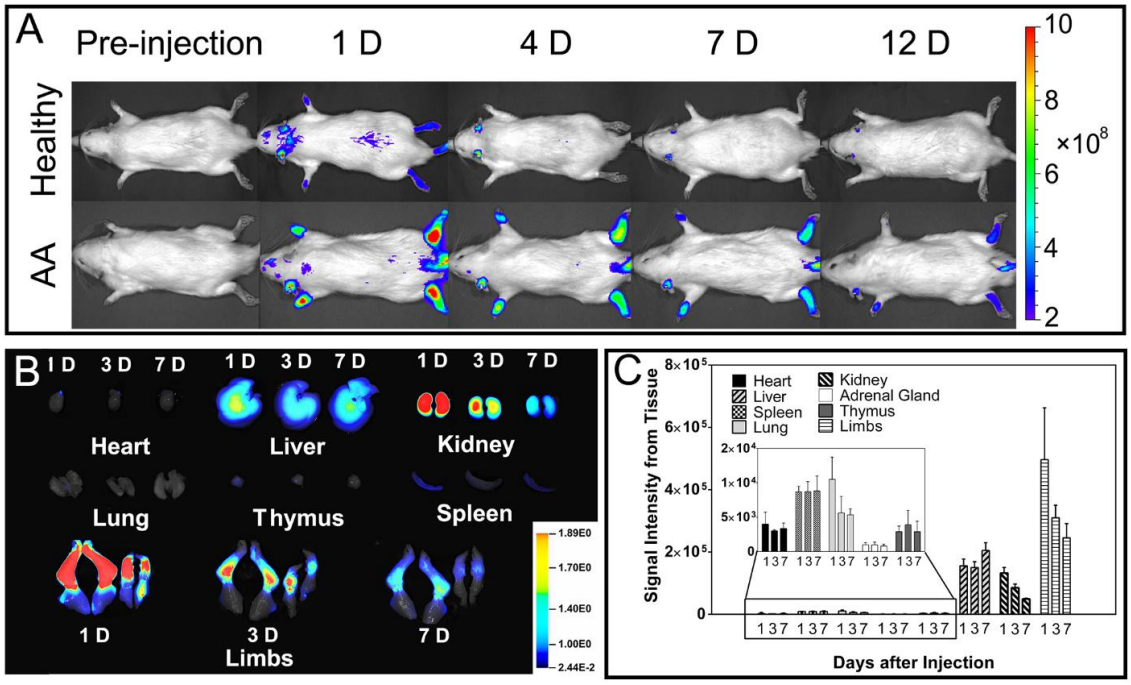

Figure 6.5 Near infrared optical imaging-based analysis of P-Tofa biodistribution. (A) Representative IVIS images depicting P-Tofa-IRDye biodistribution in AA and healthy rats after systemic administration. Images obtained 1, 4, 7 and 12 days after one intravenous injection of P-Tofa-IRDye demonstrate its retention in arthritic joints; (B) Representative ex vivo optical imaging of major organs and limbs from AA rats at 1, 3 and 7-day post P-Tofa-IRDye administration; (C) Semi-quantitative analyses of P-Tofa-IRDye biodistribution. P-Tofa-IRDye signals were detected mainly in the arthritic joints, liver and kidneys.

6.3.5 Cellular distribution of P-Tofa

To identify the cell types that sequestered and retained P-Tofa within the joint, immunohistochemistry staining with a series of cell-specific markers was performed. Numerous P-Tofa-Alexa 647 (red fluorescence) positive cells were found in synovial tissues where they co-localized with $P4HB^{+}$ (fibroblast) and $CD68^{+}$ (monocytes/macrophages) cells, consistent with synoviocyte-mediated subcellular sequestration of P-Tofa-Alexa 647 (Figure 6.6).

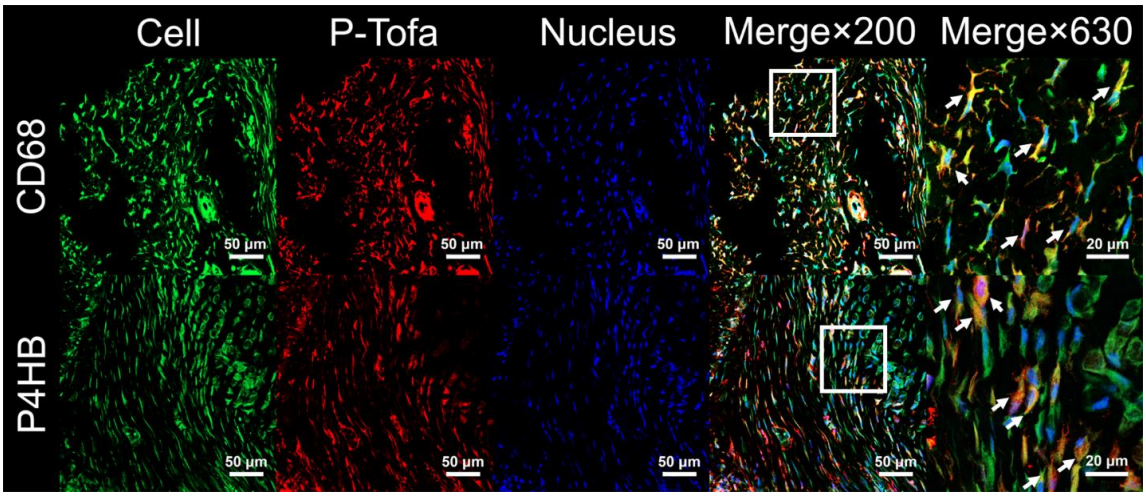

Figure 6.6 Representative confocal microscopy of anti-CD68 and anti-P4HB antibody stained sections of decalcified ankle joints from AA rates following systemic administration of P-Tofa-Alexa. Each panel is composed of five subpanels: Antibody signal (green), P-Tofa-Alexa signal (red), DAPI signal (blue), a merged image at 200× magnification and a merged image at 630× magnification are shown. Co-localization of the red and green colors confirmed the internalization of the P–Tofa-Alexa by P4HB+ (fibroblast) and CD68+ (monocytes/macrophages) synoviocytes in the arthritic joints. White arrow points to the sites of colocalization.

6.3.6 *In vitro* inhibition of JAK/STAT signaling by P-Tofa and Tofa.

To assess the ability of P-Tofa and Tofa to inhibit JAK/STAT signaling, primary murine BMM were treated with or without P-Tofa or Tofa for 1 hr or 24 hr, then challenged with 2 different IL-4 concentrations (0.2 ng/mL and 0.04 ng/mL). qPCR analysis revealed that, as expected, IL-4 strongly induced expression of alternative macrophage activation markers Arg1, Ym1/2 and Fizz1, and both Tofa and P-Tofa pretreatment for 24 hr (Figure 6.7A) or 1 hr (not shown) effectively repressed induction of all three genes. To evaluate if P-Tofa offers sustained anti-inflammatory activity, cells were pretreated with P-Tofa or Tofa, then washed and cultured for an additional 72 hr in the absence of the inhibitors, prior to IL-4 challenge. Notably, under these conditions, P-Tofa retained the ability to repress IL-4 signaling to a significantly greater extent than free Tofa (Figure 6.7B), suggesting that P-Tofa provides sustained efficacy via its cellular sequestration and subsequent subcellular Tofa release.

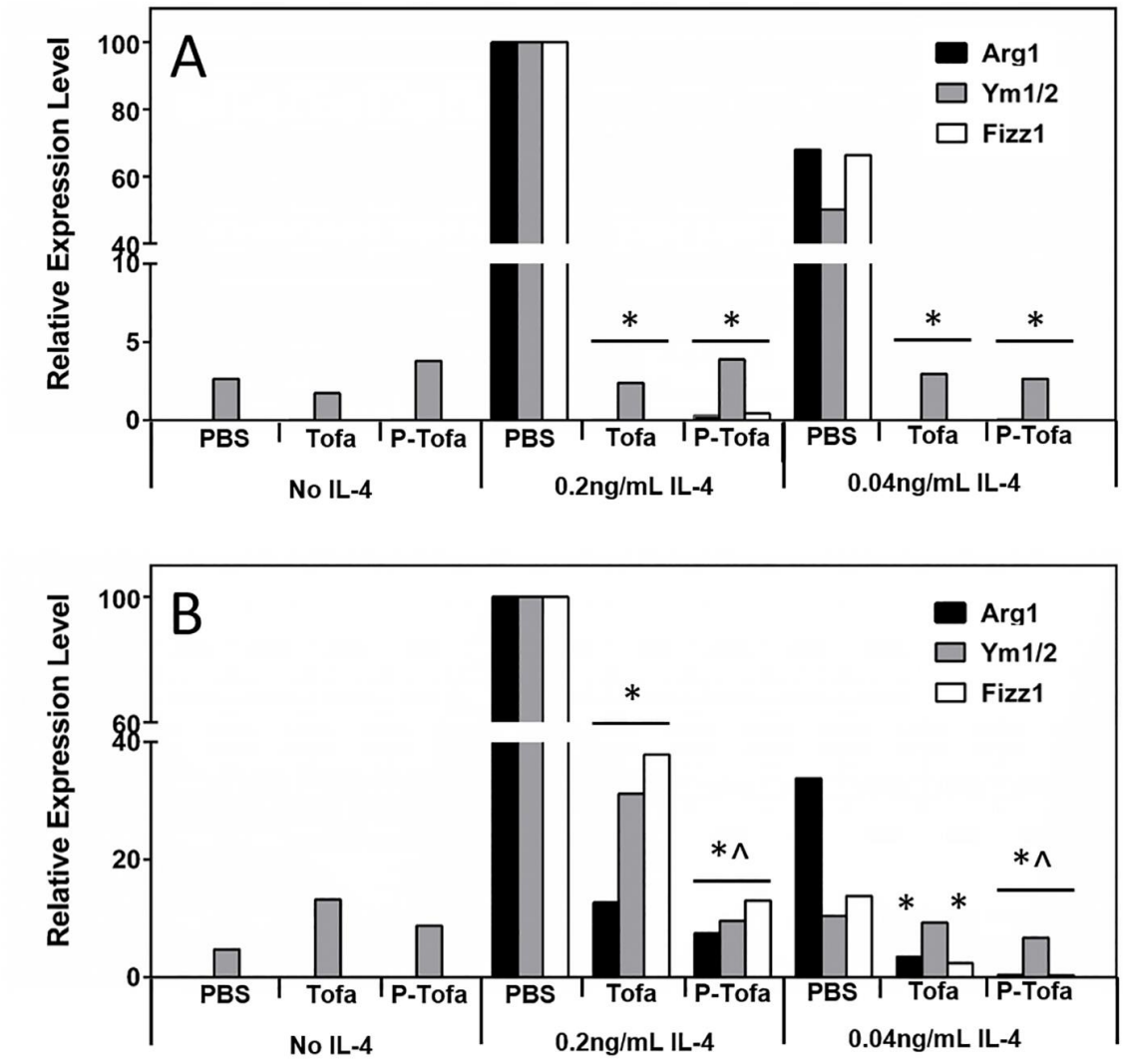

Figure 6.7 qPCR analyses of expression of Arg1, Ym1/2 and Fizz1 from BMMs after treatment with IL-4. (A) Expression levels of IL4-induced genes after 24 hr Tofa or P-Tofa treatment; (B) Expression levels of IL4-induced genes after 24 hr Tofa or P-Tofa treatment, inhibitor washout and 72 hr additional culture without the inhibitors. (*, $P < 0.05$ versus no drug at same level of IL-4; ^, $P < 0.05$ versus Tofa at same level of IL-4)

6.3.7 The impact of Tofa and P-Tofa treatments on serum levels of CXCL 10

To evaluate the effects of Tofa and P-Tofa treatments on systemic inflammatory cytokines, serum levels of CXCL10 were evaluated. As shown in Figure 6.8, CXCL10 levels were significantly elevated in arthritic rats at day 35 post arthritis induction, when compared to the healthy controls. A single dose of P-Tofa completely normalized the CXCL10 levels. Daily Tofa treatments also significantly decreased serum CXCL10 levels, though the levels were significantly higher compared to the P-Tofa group.

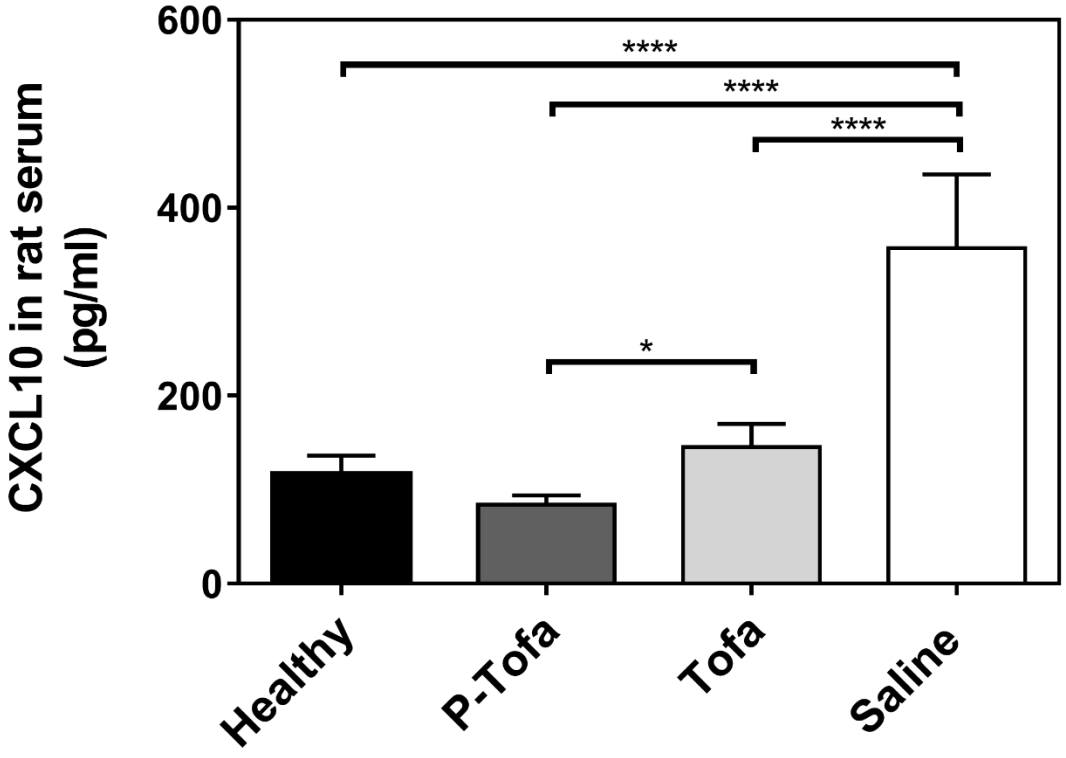

Figure 6.8 Serum CXCL10 levels at days 35 from different groups of rats. (*, P ≤ 0.05; ****, P ≤ 0.0001)

6.3.8 Preliminary toxicity assessment

Under the present dosing level, hematologic profiles of P-Tofa and Tofa treated animals (Table 6.1) were similar until week 3, when significantly lower total white blood cells (WBC), neutrophils (NE), eosinophils (EO) and basophils (BA) were observed in P-Tofa group. A small but significantly lower alkaline phosphatase (ALP) value was found in the P-Tofa group compared to the Tofa group at necropsy. There were no differences in AST or ALT levels. No histological abnormity (not shown) was found in major organs from P-Tofa group by the pathologist (SML) who was blinded to the group arrangement.

	P-Tofa			Tofa		
	CBC					
	1 week	2 weeks	3 weeks	1 week	2 weeks	3 weeks
WBC (K/µL)	22.1 ± 6.1	14.9 ± 3.3	10.2 ± 2.7*	24.6 ± 8.0	17.3 ± 5.9	19.1 ± 5.0
NE (K/µL)	8.3 ± 3.0	5.0 ± 2.0	1.8 ± 1.7*	11.0 ± 3.5	6.4 ± 4.1	7.7 ± 3.3
LY (K/µL)	11.9 ± 3.0	7.7 ± 1.2	6.3 ± 2.0	12.0 ± 4.0	9.0 ± 3.3	9.9 ± 2.4
MO (K/µL)	0.6 ± 0.3	1.2 ± 0.5	0.8 ± 0.5	0.7 ± 0.4	1.0 ± 0.4	0.6 ± 0.3
EO (K/µL)	0.8 ± 0.6	0.6 ± 0.2	0.1 ± 0.1*	0.7 ± 0.5	0.7 ± 0.4	0.6 ± 0.2
BA (K/µL)	0.3 ± 0.3	0.3 ± 0.1	0.04 ± 0.04*	0.3 ± 0.2	0.3 ± 0.2	0.3 ± 0.1
	Liver Function at Necropsy					
AST (U/L)	69.5 ± 2.0			67.6 ± 2.4		
ALT (U/L)	76.3 ± 4.7			76.6 ± 2.7		

ALP (U/L)	315.3 ± 29.4*	347.3 ± 23.4

Table 6.1 Hematologic profiles and liver function tests with P-Tofa and Tofa treatments. *, *P≤0.05, significantly lower than Tofa group*

6.4 Discussion

To test our hypothesis, a HPMA copolymer-based macromolecular prodrug of Tofacitinib (P-Tofa) was designed, synthesized and evaluated using an adjuvant-induced arthritis rat model. To establish the arthrotropism of P-Tofa according to our hypothesis, rats with established AA were administered P-Tofa-IRDye and its biodistribution and tissue-specific retention were evaluated using sequential *in vivo* NIR optical imaging. As shown in Figure 6.5A, the IRDye signal mainly localized in the arthritic limbs. Due to the limited tissue penetration depth of the NIR fluorescent signal [181], the distribution of P-Tofa-IRDye in the major organs and arthritic limbs were imaged *ex vivo* and analyzed semi-quantitatively using an LI-COR small animal imager. The results (Figure 6.5B, 6.5C) confirmed that the inflamed joints in the affected limbs were the major sites of P-Tofa-IRDye localization with additional distribution sites in the main clearance organs (i.e. liver and kidneys). On a cellular level, immunohistochemistry analysis of the decalcified arthritic joints revealed that the P-Tofa-Alexa was sequestered by fibroblast-like (P4HB+) and macrophage-like (CD68+) synoviocytes (Figure 6.6), providing direct evidence of P-Tofa's targeting to key cell types involved in the joint inflammatory pathology [182-184].

We hypothesized that the tissue and cellular specificity of systemically administered P-Tofa would lead to a potent and sustained anti-rheumatic effect. Our original dose equivalent treatment protocol was designed to terminate at day 35 post arthritis induction. The results (Figure 6.2A, 6.2B) established that a single dose of P-Tofa was effective in ameliorating joint inflammation and improving the

articular index (AI) scores during this period of time. Having observed this initial beneficial effect, we further extended the observation period. To maintain dose equivalence, no additional Tofa was given to the Tofa group. Of importance, the single dose P-Tofa treated rats continued to show reduced joint inflammation and articular index score reduction until day 65 post arthritis induction, when signs of a minor arthritis flare (e.g. a small increase of the arthritis score) was observed. Immediately after the cessation of Tofa treatment, a flare was detected in the Tofa treated group, which continued to worsen until the experimental endpoint (day 65 post arthritis induction). Tissue histopathology (Figure 6.3A, 6.3B) and micro-CT (Figure 6.4) analyses of the ankle joints isolated at the end point of the experiment demonstrated preservation of joint cartilage and subchondral bone integrity in the animals treated with the single dose P-Tofa. The Tofa-treated animals, in contrast, showed only moderate bone and cartilage protection when compared to the saline controls; but exhibited more extensive joint tissue damage compared to the P-Tofa-treated group.

In vitro cell culture studies were undertaken to compare the efficacy of P-Tofa and Tofa in inhibition of JAK/STAT signaling. Murine BMM were treated with P-Tofa or Tofa prior to challenge with IL-4. This cytokine signals via the JAK/STAT6 pathway and induces the expression of markers of alternative macrophage activation, including arginase-1 (Arg1), YM1/2, and Fizz1. qPCR analysis revealed that IL-4 strongly induced expression of Arg1, Ym1/2 and Fizz1. Tofa treatment for 24 hr or 1 hr effectively repressed induction of all three genes. P-Tofa was equally effective under these conditions (Figure 6.7A). To assess the relative efficacy of

P-Tofa or Tofa to produce sustained inhibition of IL-4 induced JAK/STAT signaling, in a second set of experiments, cells were pretreated with P-Tofa or Tofa, then washed and cultured for an additional 72 hr in the absence of inhibitors, prior to IL-4 challenge. Of importance, under these conditions, the P-Tofa treatment produced sustained inhibition of IL-4 signaling (Figure 6.7B), whereas the Tofa treated cells became IL-4 responsive by 72 hr. These findings are consistent with sustained release of active drug from the P-Tofa and corroborate well with the *in vitro* data (Figure 6.2) showing the sustained release of free Tofa in acidic environments, present in the synovium of patients with active arthritis and in the subcellular lysosomal compartment in which the macromolecular prodrug is sequestered [175].

To further explore the impact of P-Tofa treatment, we measured the serum levels of CXCL10. In human studies, circulating CXCL10 as well as synovial expression of this chemokine has been shown to be sensitive to Tofa treatment [185] and it has been implicated as a major contributor to the recruitment and activation of immune cells involved in the local synovial inflammation. In this study, we found that CXCL10 levels were significantly elevated in arthritic rats, when compared to the healthy controls; and a single dose of P-Tofa completely suppressed the elevated serum CXCL10 levels at day 35 post induction of arthritis (Figure 6.8).

Our data attributes this superior and long-lasting therapeutic efficacy of P-Tofa to its passive targeting to sites of joint inflammation and synoviocyte-mediated local sequestration and sustained Tofa release, which is distinctively different from Tofa's pharmacokinetic profile [186]. We did detect alterations in WBC count and ALP levels in the P-Tofa group in the later stage of the treatment, suggesting P-

Tofa dosing at this level (130.2 mg/kg, Tofa equivalent, i.v. single dose) may have reached the upper limit of its therapeutic window, which is 20-times higher than the Tofa dose (6.2 mg/kg, daily oral gavage) used in a preclinical therapeutic efficacy study in this particular animal model [187]. Clearly, additional dose escalation and a more comprehensive toxicity studies are necessary to further advance P-Tofa's development. Given its superior and sustained therapeutic efficacy, we postulate that P-Tofa has significant potential for development as a treatment for RA.

6.5 Conclusion

A single i.v. administration of P-Tofa provided superior and sustained therapeutic efficacy in an adjuvant-induced arthritis rat model, when compared to dose equivalent daily Tofa treatment. P-Tofa's significantly widened therapeutic window holds the promise for enhancing the clinical efficacy of Tofacitinib for the treatment of RA.

CHAPTER 7

SUMMARY

7.1 Conclusion

Our laboratory has developed HPMA macromolecular conjugates for early diagnosis and better treatment of the musculoskeletal disorders. The achievement we obtained proved our concept hypothesis that the macromolecular prodrug delivery system may improve the therapeutic outcome and benefit with the diagnostics targeting. In my PhD program of study, I focused on the investigation of the impacts of the different macromolecular conjugates' structure parameters on their pharmacokinetics, biodistribution and therapeutic efficacy. A series of the conjugates with different molecular weight (MW), drug content, drug-activation mechanism and drug payload were synthesized for this comprehensive investigation. The labeled conjugates (conjugates with different MW and drug content) were analyzed for their PK/BD profiles in the murine implant loosening model and *in vitro* cell culture study. The conjugates with different activation mechanisms were studied for their *in vitro* releasing kinetics under different condition (different pH values or with human or rat serum) and *in vivo* therapeutic efficacy in an adjuvant-induced arthritis rat model. Our initial model drug for the above studies is a potent glucocorticoid (dexamethasone). To understand if the development of macromolecular prodrug conjugates may also be beneficial for other drug classes, we designed and synthesized the HPMA copolymer conjugate (P-Tofa) with a disease-modify-

ing-antirheumatic drug (tofacitinib, Tofa). The positive outcome validated our notion that macromolecularization of antirheumatic drug may potneitate the efficacy of the parent drug and potentially reduce associated systemic toxicities.

7.2 Future plan

Overall, this project has provided deep insights of the HPMA copolymer conjugates' structure properties' influence on its efficacy and safety. These information provides further instruction on the rational design of drug delivery systems for the clinical management of musculoskeletal conditions. In the future, other polymeric carrier system and drug classes may also be explored for the improved treatment of musculoskeletal diseases. Besides passive targeting, different active targeting moieties, including bone targeting ligands may be introduced to further potentiate macromolecular prodrug development for better treatment of musculoskeletal diseases.

Reference

1. Hertling, D. and R.M. Kessler, *Management of common musculoskeletal disorders: physical therapy principles and methods*. 2006: Lippincott Williams & Wilkins.

2. Wang, D., et al., *Bone-targeting macromolecular therapeutics.* Advanced drug delivery reviews, 2005. **57**(7): p. 1049-1076.

3. Stuart L. Weinstein, E.H.Y., Gunnar B. J. Andersson, Paul A. Ullucci, et al, *The Burden of Musculoskeletal Diseases in the United States.* 2015.

4. Faces of Orthopaedics, K.P.S., David S. Jevsevar, *Faces of Orthopaedics.* 2016.

5. Armas, L.A. and R.R. Recker, *Pathophysiology of osteoporosis: new mechanistic insights.* Endocrinology and Metabolism Clinics, 2012. **41**(3): p. 475-486.

6. Whyte, M.P., *Paget's disease of bone.* New England Journal of Medicine, 2006. **355**(6): p. 593-600.

7. Gabriel, S.E., *The epidemiology of rheumatoid arthritis.* Rheumatic Disease Clinics, 2001. **27**(2): p. 269-281.

8. Olsen, N.J. and C.M. Stein, *New drugs for rheumatoid arthritis.* New England Journal of Medicine, 2004. **350**(21): p. 2167-2179.

9. Mateen, S., et al., *Understanding the role of cytokines in the pathogenesis of rheumatoid arthritis.* Clinica chimica acta, 2016. **455**: p. 161-171.

10. Mankia, K. and P. Emery, *Preclinical rheumatoid arthritis: progress toward prevention.* Arthritis & Rheumatology, 2016. **68**(4): p. 779-788.

11. Longo, U.G., S. Petrillo, and V. Denaro, *Current concepts in the management of rheumatoid hand.* International journal of rheumatology, 2015. **2015**.

12. De Cock, D., et al., *The optimal combination therapy for the treatment of early rheumatoid arthritis.* Expert opinion on pharmacotherapy, 2015. **16**(11): p. 1615-1625.

13. El Desoky, E.S., *Pharmacotherapy of rheumatoid arthritis: an overview.* Current therapeutic research, 2001. **62**(2): p. 92-112.

14. Danelich, I.M., et al., *Safety of nonsteroidal antiinflammatory drugs in patients with cardiovascular disease.* Pharmacotherapy: The Journal of Human Pharmacology and Drug Therapy, 2015. **35**(5): p. 520-535.

15. Ferreira, J.F., A.A.A. Mohamed, and P. Emery, *Glucocorticoids and rheumatoid arthritis.* Rheumatic Disease Clinics, 2016. **42**(1): p. 33-46.

16. Rasch, L.A., et al., *Glucocorticoid safety for treating rheumatoid arthritis.* Expert opinion on drug safety, 2015. **14**(6): p. 839-844.

17. Ramiro, S., et al., *Safety of synthetic and biological DMARDs: a systematic literature review informing the 2013 update of the EULAR recommendations for management of rheumatoid arthritis.* Annals of the rheumatic diseases, 2014. **73**(3): p. 529-535.

18. Nam, J.L., et al., *Efficacy of biological disease-modifying antirheumatic drugs: a systematic literature review informing the 2016 update of the EULAR recommendations for the management of rheumatoid arthritis.* Annals of the rheumatic diseases, 2017. **76**(6): p. 1113-1136.

19. Schwartz, D.M., et al., *Type I/II cytokines, JAKs, and new strategies for treating autoimmune diseases.* Nature Reviews Rheumatology, 2016. **12**(1): p. 25.

20. Simmons, D.L., *Targeting kinases: a new approach to treating inflammatory rheumatic diseases.* Current opinion in pharmacology, 2013. **13**(3): p. 426-434.

21. Statistics, N.C.f.H., *Health, United States, 2013: With special feature on prescription drugs.* 2014.

22. Abu-Amer, Y., I. Darwech, and J.C. Clohisy, *Aseptic loosening of total joint replacements: mechanisms underlying osteolysis and potential therapies.* Arthritis research & therapy, 2007. **9**(1): p. S6.

23. Hallab, N.J. and J.J. Jacobs, *Biologic effects of implant debris.* Bulletin of the NYU hospital for joint diseases, 2009. **67**(2): p. 182.

24. Callaghan, J.J., A.G. Rosenberg, and H.E. Rubash, *The adult hip*. Vol. 1. 2007: Lippincott Williams & Wilkins.

25. Amstutz, H.C., et al., *Mechanism and clinical significance of wear debris-induced osteolysis.* Clinical orthopaedics and related research, 1992(276): p. 7-18.

26. Anderson, J.M., *Biological responses to materials.* Annual review of materials research, 2001. **31**(1): p. 81-110.

27. Bauer, T.W. and J. Schils, *The pathology of total joint arthroplasty.* Skeletal radiology, 1999. **28**(9): p. 483-497.

28. Ingham, E. and J. Fisher, *The role of macrophages in osteolysis of total joint replacement.* Biomaterials, 2005. **26**(11): p. 1271-1286.

29. Loi, F., et al., *The effects of immunomodulation by macrophage subsets on osteogenesis in vitro.* Stem cell research & therapy, 2016. **7**(1): p. 15.

30. Merkel, K.D., et al., *Tumor necrosis factor-α mediates orthopedic implant osteolysis.* The American journal of pathology, 1999. **154**(1): p. 203-210.

31. Yokohama, Y., et al., *Production of matrix metalloproteinases at the bone-implant interface in loose total hip replacements.* Laboratory investigation; a journal of technical methods and pathology, 1995. **73**(6): p. 899-911.

32. Kaplan, F.S., D.L. Glaser, and E.M. Shore, *Fibrodysplasia (myositis) ossificans progressiva.* Primer on the Metabolic Bone Diseases and Disorders of Mineral Metabolism, 2006: p. 450-453.

33. Kaplan, F.S., et al., *Heterotopic ossification.* Journal of the American Academy of Orthopaedic Surgeons, 2004. **12**(2): p. 116-125.

34. Cohen, R.B., et al., *The natural history of heterotopic ossification in patients who have fibrodysplasia ossificans progressiva. A study of forty-four patients.* JBJS, 1993. **75**(2): p. 215-219.

35. Kaplan, F.S., et al., *Progressive osseous heteroplasia: a distinct developmental disorder of heterotopic ossification. Two new case reports and follow-up of three previously reported cases.* JBJS, 1994. **76**(3): p. 425-436.

36. Brooker, A.F., et al., *Ectopic ossification following total hip replacement: incidence and a method of classification.* JBJS, 1973. **55**(8): p. 1629-1632.

37. Ahrengart, L., *Periarticular heterotopic ossification after total hip arthroplasty: Risk factors and consequences.* Clinical Orthopaedics and Related Research, 1991(263): p. 49-58.

38. McAfee, P.C., et al., *Classification of heterotopic ossification (HO) in artificial disk replacement.* Clinical Spine Surgery, 2003. **16**(4): p. 384-389.

39. Mehren, C., et al., *Heterotopic ossification in total cervical artificial disc replacement.* Spine, 2006. **31**(24): p. 2802-2806.

40. Alfieri, K.A., J.A. Forsberg, and B.K. Potter, *Blast injuries and heterotopic ossification.* Bone and Joint Research, 2012. **1**(8): p. 174-179.

41. Maender, C., D. Sahajpal, and T.W. Wright, *Treatment of heterotopic ossification of the elbow following burn injury: recommendations for surgical excision and perioperative prophylaxis using radiation therapy.* Journal of shoulder and elbow surgery, 2010. **19**(8): p. 1269-1275.

42. Nelson, E.R., et al., *Heterotopic ossification following burn injury: the role of stem cells.* Journal of Burn Care & Research, 2012. **33**(4): p. 463-470.

43. Peterson, S.L., et al., *Postburn heterotopic ossification: insights for management decision making.* Journal of Trauma and Acute Care Surgery, 1989. **29**(3): p. 365-369.

44. Genêt, F., et al., *Troublesome Heterotopic Ossification after Central Nervous System Damage: A Survey of 570 Surgeries.* PLOS ONE, 2011. **6**(1): p. e16632.

45. Sakellariou, V., et al., *Heterotopic ossification following traumatic brain injury and spinal cord injury: insight into the etiology and pathophysiology.* J Musculoskelet Neuronal Interact, 2012. **12**(4): p. 230-240.

46. Cipriano, C.A., S.G. Pill, and M.A. Keenan, *Heterotopic ossification following traumatic brain injury and spinal cord injury.* Journal of the American Academy of Orthopaedic Surgeons, 2009. **17**(11): p. 689-697.

47. Garland, D.E., *A clinical perspective on common forms of acquired heterotopic ossification.* Clinical orthopaedics and related research, 1991. **263**: p. 13-29.

48. Shehab, D., A.H. Elgazzar, and B.D. Collier, *Heterotopic Ossification*.* Journal of Nuclear Medicine, 2002. **43**(3): p. 346-353.

49. Potter, C.B.K., et al., *Heterotopic Ossification Following Traumatic and Combat-Related Amputations: Prevalence, Risk Factors, and Preliminary Results of Excision.* JBJS, 2007. **89**(3): p. 476-486.

50. Forsberg, J.A., et al., *Heterotopic Ossification in High-Energy Wartime Extremity Injuries: Prevalence and Risk Factors.* JBJS, 2009. **91**(5): p. 1084-1091.

51. Strauss, J.B., et al., *Cost of Radiotherapy Versus NSAID Administration for Prevention of Heterotopic Ossification After Total Hip Arthroplasty.* International Journal of Radiation Oncology*Biology*Physics, 2008. **71**(5): p. 1460-1464.

52. Sharifi, H., *Cost Effectiveness Analysis in Orthopaedic Surgery.* 2010.

53. Baird, E.O. and Q.K. Kang, *Prophylaxis of heterotopic ossification–an updated review.* Journal of orthopaedic surgery and research, 2009. **4**(1): p. 12.

54. Karlsson, A., *Autonomic dysreflexia.* Spinal cord, 1999. **37**(6).

55. Mathias, C. and H. Frankel, *Autonomic disturbances in spinal cord lesions*. 1999.

56. Perkash, A., et al., *Persistent hypercoagulation associated with heterotopic ossification in patients with spinal cord injury long after injury has occurred.* Spinal Cord, 1993. **31**(10): p. 653-659.

57. Evans, K.N., et al., *Inflammatory Cytokine and Chemokine Expression is Associated With Heterotopic Ossification in High-Energy Penetrating War Injuries.* Journal of Orthopaedic Trauma, 2012. **26**(11): p. e204-e213.

58. Lounev, V.Y., et al., *Identification of progenitor cells that contribute to heterotopic skeletogenesis.* The Journal of Bone and Joint Surgery. American volume., 2009. **91**(3): p. 652.

59. Medici, D., et al., *Conversion of vascular endothelial cells into multipotent stem-like cells.* Nature medicine, 2010. **16**(12): p. 1400.

60. Wu, X., T.J. Walters, and C.R. Rathbone, *Skeletal muscle satellite cell activation following cutaneous burn in rats.* Burns, 2013. **39**(4): p. 736-744.

61. Suda, R.K., et al., *Circulating osteogenic precursor cells in heterotopic bone formation.* Stem cells, 2009. **27**(9): p. 2209-2219.

62. Kan, L., et al., *Dysregulation of local stem/progenitor cells as a common cellular mechanism for heterotopic ossification.* Stem Cells, 2009. **27**(1): p. 150-156.

63. Kalajzic, Z., et al., *Use of an alpha-smooth muscle actin GFP reporter to identify an osteoprogenitor population.* Bone, 2008. **43**(3): p. 501-510.

64. Kaplan, F.S., et al., *Hematopoietic stem-cell contribution to ectopic skeletogenesis.* JBJS, 2007. **89**(2): p. 347-357.

65. Moriatis, J.M., et al., *Limb swelling in patients who have fibrodysplasia ossificans progressiva.* Clinical orthopaedics and related research, 1997. **336**: p. 247-253.

66. Wozney, J.M., et al., *Novel regulators of bone formation: molecular clones and activities.* Science, 1988. **242**(4885): p. 1528-1534.

67. Paul, B.Y., et al., *BMP type I receptor inhibition reduces heterotopic ossification.* Nature medicine, 2008. **14**(12): p. 1363.

68. Banovac, K., et al., *Prevention of heterotopic ossification after spinal cord injury with indomethacin.* Spinal cord, 2001. **39**(7): p. 370.

69. Weber, E., et al., *COX 2 selectivity of non-steroidal anti-inflammatory drugs and perioperative blood loss in hip surgery. A randomized comparison of indomethacin and meloxicam.* European journal of anaesthesiology, 2003. **20**(12): p. 963-966.

70. Neal, B.C., et al., *A systematic survey of 13 randomized trials of non-steroidal anti-inflammatory drugs for the prevention of heterotopic bone formation after major hip surgery.* Acta Orthopaedica Scandinavica, 2000. **71**(2): p. 122-128.

71. Grohs, J.G., M. Schmidt, and A. Wanivenhaus, *Selective COX-2 inhibitor versus indomethacin for the prevention of heterotopic ossification after hip replacement: a double-blind randomized trial of 100 patients with 1-year follow-up.* Acta orthopaedica, 2007. **78**(1): p. 95-98.

72. Saudan, M., et al., *Celecoxib versus ibuprofen in the prevention of heterotopic ossification following total hip replacement: a prospective randomised trial.* Bone & Joint Journal, 2007. **89**(2): p. 155-159.

73. Legenstein, R., P. Bösch, and A. Ungersböck, *Indomethacin versus meloxicam for prevention of heterotopic ossification after total hip arthroplasty.* Archives of orthopaedic and trauma surgery, 2003. **123**(2-3): p. 91-94.

74. Cooley, L.M. and R.J. Goss, *The effects of transplantation and x‐irradiation on the repair of fractured bones.* Developmental Dynamics, 1958. **102**(2): p. 167-181.

75. Coventry, M.B. and P.W. Scanlon, *The use of radiation to discourage ectopic bone. A nine-year study in surgery about the hip.* The Journal of bone and joint surgery. American volume, 1981. **63**(2): p. 201-208.

76. Childs, H.A., et al., *A prospective evaluation of the timing of postoperative radiotherapy for preventing heterotopic ossification following traumatic acetabular fractures.* International Journal of Radiation Oncology• Biology• Physics, 2000. **47**(5): p. 1347-1352.

77. Chao, S.T., et al., *External beam radiation helps prevent heterotopic bone formation in patients with a history of heterotopic ossification.* The Journal of arthroplasty, 2006. **21**(5): p. 731-736.

78. Balboni, T.A., R. Gobezie, and H.J. Mamon, *Heterotopic ossification: Pathophysiology, clinical features, and the role of radiotherapy for prophylaxis.* International Journal of Radiation Oncology• Biology• Physics, 2006. **65**(5): p. 1289-1299.

79. Allmeroth, M., et al., *Modifying the body distribution of HPMA-based copolymers by molecular weight and aggregate formation.* Biomacromolecules, 2011. **12**(7): p. 2841-2849.

80. Hunt, J.L., et al., *Heterotopic ossification revisited: a 21-year surgical experience.* Journal of burn care & research, 2006. **27**(4): p. 535-540.

81. Brantus, J.-F. and P.J. Meunier, *Effects of intravenous etidronate and oral corticosteroids in fibrodysplasia ossificans progressiva.* Clinical orthopaedics and related research, 1998(346): p. 117-120.

82. Vardy, J., et al., *Side effects associated with the use of dexamethasone for prophylaxis of delayed emesis after moderately emetogenic chemotherapy.* British journal of cancer, 2006. **94**(7): p. 1011.

83. Barnes, P.J. and I.M. Adcock, *Glucocorticoid resistance in inflammatory diseases.* The Lancet, 2009. **373**(9678): p. 1905-1917.

84. Bangham, A., M.M. Standish, and J.C. Watkins, *Diffusion of univalent ions across the lamellae of swollen phospholipids.* Journal of molecular biology, 1965. **13**(1): p. 238-IN27.

85. Gentile, L., et al., *Multilamellar vesicle formation from a planar lamellar phase under shear flow.* Langmuir, 2014. **30**(28): p. 8316-8325.

86. Lokappa, S.B. and T.S. Ulmer, *α-Synuclein populates both elongated and broken helix states on small unilamellar vesicles.* Journal of Biological Chemistry, 2011. **286**(24): p. 21450-21457.

87. Moyano, F., J.J. Silber, and N.M. Correa, *On the investigation of the bilayer functionalities of 1, 2-di-oleoyl-sn-glycero-3-phosphatidylcholine (DOPC) large unilamellar vesicles using cationic hemicyanines as optical probes: a wavelength-selective fluorescence approach.* Journal of colloid and interface science, 2008. **317**(1): p. 332-345.

88. Ning, Y.-M., et al., *Liposomal Doxorubicin in Combination With Bortezomib for Relapsed or Refractory Multiple Myeloma: Page 3 of 3.* Oncology, 2007. **21**(12).

89. Judson, I., et al., *Randomised phase II trial of pegylated liposomal doxorubicin (DOXIL®/CAELYX®) versus doxorubicin in the treatment of advanced or metastatic soft tissue sarcoma: a study by the EORTC Soft Tissue and Bone Sarcoma Group.* European Journal of Cancer, 2001. **37**(7): p. 870-877.

90. Northfelt, D.W., et al., *Pegylated-liposomal doxorubicin versus doxorubicin, bleomycin, and vincristine in the treatment of AIDS-related Kaposi's sarcoma: results of a randomized phase III clinical trial.* Journal of clinical oncology, 1998. **16**(7): p. 2445-2451.

91. Chen, F., et al., *The development of dentotropic micelles with biodegradable tooth-binding moieties.* Pharmaceutical research, 2013. **30**(11): p. 2808-2817.

92. Wiedwald, U., et al., *Preparation and characterization of supported magnetic nanoparticles prepared by reverse micelles.* Beilstein journal of nanotechnology, 2010. **1**: p. 24.

93. Koizumi, F., et al., *Novel SN-38–incorporating polymeric micelles, NK012, eradicate vascular endothelial growth factor–secreting bulky tumors.* Cancer research, 2006. **66**(20): p. 10048-10056.

94. Nederberg, F., et al., *Biodegradable nanostructures with selective lysis of microbial membranes.* Nature chemistry, 2011. **3**(5): p. 409.

95. Ventola, C.L., *Progress in nanomedicine: approved and investigational nanodrugs.* Pharmacy and Therapeutics, 2017. **42**(12): p. 742.

96. Xu, X.-L., et al., *Endogenous sialic acid-engineered micelles: a multifunctional platform for on-demand methotrexate delivery and bone repair of rheumatoid arthritis.* Nanoscale, 2018. **10**(6): p. 2923-2935.

97. Low, S.A., et al., *Biodistribution of fracture-targeted GSK3β inhibitor-loaded micelles for improved fracture healing.* Biomacromolecules, 2015. **16**(10): p. 3145-3153.

98. Low, S.A., et al., *Healing efficacy of fracture-targeted GSK3β inhibitor-loaded micelles for improved fracture repair.* Nanomedicine, 2017. **12**(3): p. 185-193.

99. Kocbek, P., et al., *Targeting cancer cells using PLGA nanoparticles surface modified with monoclonal antibody.* Journal of controlled release, 2007. **120**(1-2): p. 18-26.

100. Verma, P. and M. Ahuja, *Optimization, characterization and evaluation of chitosan-tailored cubic nanoparticles of clotrimazole.* International journal of biological macromolecules, 2015. **73**: p. 138-145.

101. Wang, Y., et al., *Shape-controlled paclitaxel nanoparticles with multiple morphologies: rod-shaped, worm-like, spherical, and fingerprint-like.* Molecular pharmaceutics, 2014. **11**(10): p. 3766-3771.

102. Chen, J., et al., *Shape-tunable hollow silica nanomaterials based on a soft-templating method and their application as a drug carrier.* ACS applied materials & interfaces, 2014. **6**(24): p. 21921-21930.

103. Kurien, T., R. Pearson, and B. Scammell, *Bone graft substitutes currently available in orthopaedic practice: the evidence for their use.* The bone & joint journal, 2013. **95**(5): p. 583-597.

104. Epstein, N.E., *Preliminary documentation of the comparable efficacy of vitoss versus NanOss bioactive as bone graft expanders for posterior cervical fusion.* Surgical neurology international, 2015. **6**(Suppl 4): p. S164.

105. Strietzel, F.P., P.A. Reichart, and H.L. Graf, *Lateral alveolar ridge augmentation using a synthetic nano‐crystalline hydroxyapatite bone substitution material (Ostim®). Preliminary clinical and histological results.* Clinical oral implants research, 2007. **18**(6): p. 743-751.

106. Schwarz, F., et al., *Healing of intrabony peri‐implantitis defects following application of a nanocrystalline hydroxyapatite (Ostim™) or a bovine‐derived xenograft (Bio‐Oss™) in combination with a collagen membrane (Bio‐Gide™). A case series.* Journal of Clinical Periodontology, 2006. **33**(7): p. 491-499.

107. Cutter, C.S. and B.J. Mehrara, *Bone grafts and substitutes.* Journal of long-term effects of medical implants, 2006. **16**(3).

108. Damron, T.A., *Use of 3D β-tricalcium phosphate (Vitoss®) scaffolds in repairing bone defects.* 2007.

109. Mura, S. and P. Couvreur, *Nanotheranostics for personalized medicine.* Advanced drug delivery reviews, 2012. **64**(13): p. 1394-1416.

110. Li, Y., et al., *New reversed-phase/anion-exchange/hydrophilic interaction mixed-mode stationary phase based on dendritic polymer-modified porous silica.* Journal of Chromatography A, 2014. **1337**: p. 133-139.

111. Kushwaha, D. and V.K. Tiwari, *Click chemistry inspired synthesis of glyco-porphyrin dendrimers.* The Journal of organic chemistry, 2013. **78**(16): p. 8184-8190.

112. Jansen, J.F. and E. Meijer, *Encapsulation of guest molecules into a dendritic box.* Science, 1994. **266**(5188): p. 1226-1229.

113. Newkome, G.R., et al., *Unimolecular micelles.* Angewandte Chemie International Edition in English, 1991. **30**(9): p. 1178-1180.

114. Thanki, K., et al., *Oral delivery of anticancer drugs: challenges and opportunities.* Journal of controlled release, 2013. **170**(1): p. 15-40.

115. Yamashita, S., et al., *Development of PEGylated carboxylic acid-modified polyamidoamine dendrimers as bone-targeting carriers for the treatment of bone diseases.* Journal of Controlled Release, 2017. **262**: p. 10-17.

116. Yamashita, S., et al., *Bone-targeting dendrimer for the delivery of methotrexate and treatment of bone metastasis.* Journal of drug targeting, 2018: p. 1-11.

117. Couvreur, P. and C. Vauthier, *Nanotechnology: intelligent design to treat complex disease.* Pharmaceutical research, 2006. **23**(7): p. 1417-1450.

118. Ren, K., et al., *Early detection and treatment of wear particle-induced inflammation and bone loss in a mouse calvarial osteolysis model using HPMA copolymer conjugates.* Molecular pharmaceutics, 2011. **8**(4): p. 1043-1051.

119. Yuan, F., et al., *Dexamethasone prodrug treatment prevents nephritis in lupus‐prone (NZB × NZW) F1 mice without causing systemic side effects.* Arthritis & Rheumatology, 2012. **64**(12): p. 4029-4039.

120. Garay, R.P., et al., *Therapeutic perspectives on uricases for gout.* Joint Bone Spine, 2012. **79**(3): p. 237-242.

121. Maeda, H., J. Takeshita, and R. Kanamaru, *A lipophilic derivative of neocarzinostatin a polymer conjugation of an antitumor protein antibiotic.* International journal of peptide and protein research, 1979. **14**(2): p. 81-87.

122. Fang, J., H. Nakamura, and H. Maeda, *The EPR effect: unique features of tumor blood vessels for drug delivery, factors involved, and limitations and augmentation of the effect.* Advanced drug delivery reviews, 2011. **63**(3): p. 136-151.

123. Maeda, H., et al., *Tailor-making of protein drugs by polymer conjugation for tumor targeting: a brief review on smancs.* Journal of protein chemistry, 1984. **3**(2): p. 181-193.

124. Maeda, H. and T. Konno, *Metamorphosis of neocarzinostatin to SMANCS: Chemistry, biology, pharmacology, and clinical effect of the first prototype anticancer polymer therapeutic*, in *Neocarzinostatin*. 1997, Springer. p. 227-267.

125. Matsumura, Y. and H. Maeda, *A new concept for macromolecular therapeutics in cancer chemotherapy: mechanism of tumoritropic accumulation of proteins and the antitumor agent smancs.* Cancer research, 1986. **46**(12 Part 1): p. 6387-6392.

126. Seymour, L., et al., *Effect of molecular weight (M w) of N‐(2‐hydroxypropyl) methacrylamide copolymers on body distribution and rate of excretion after subcutaneous, intraperitoneal, and intravenous administration to rats.* Journal of biomedical materials research, 1987. **21**(11): p. 1341-1358.

127. Dand, N.M., et al., *Polymeric micelles as a drug carrier for tumor targeting.* Chronicles of Young Scientists, 2013. **4**(2): p. 94.

128. Folkman, J., *Angiogenesis in cancer, vascular, rheumatoid and other disease.* Nature medicine, 1995. **1**(1): p. 27.

129. Hashizume, H., et al., *Openings between defective endothelial cells explain tumor vessel leakiness.* The American journal of pathology, 2000. **156**(4): p. 1363-1380.

130. Jain, R.K., *Transport of molecules, particles, and cells in solid tumors.* Annual review of biomedical engineering, 1999. **1**(1): p. 241-263.

131. Jain, R.K., L.L. Munn, and D. Fukumura, *Dissecting tumour pathophysiology using intravital microscopy.* Nature Reviews Cancer, 2002. **2**(4): p. 266.

132. Roberts, W.G. and G.E. Palade, *Neovasculature induced by vascular endothelial growth factor is fenestrated.* Cancer research, 1997. **57**(4): p. 765-772.

133. Wang, D. and S.R. Goldring, *The bone, the joints and the Balm of Gilead*. 2011, ACS Publications.

134. Yuan, F., et al., *Development of macromolecular prodrug for rheumatoid arthritis.* Advanced drug delivery reviews, 2012. **64**(12): p. 1205-1219.

135. Quan, L.-d., et al., *Development of a macromolecular prodrug for the treatment of inflammatory arthritis: mechanisms involved in arthrotropism and sustained therapeutic efficacy.* Arthritis research & therapy, 2010. **12**(5): p. R170.

136. Weiner, S. and P.M. Dove, *An overview of biomineralization processes and the problem of the vital effect.* Reviews in mineralogy and geochemistry, 2003. **54**(1): p. 1-29.

137. Albert, A. and C. Rees, *Avidity of the tetracyclines for the cations of metals.* Nature, 1956. **177**(4505): p. 433.

138. Grenier, D., M.-P. Huot, and D. Mayrand, *Iron-chelating activity of tetracyclines and its impact on the susceptibility of actinobacillus actinomycetemcomitansto these antibiotics.* Antimicrobial agents and chemotherapy, 2000. **44**(3): p. 763-766.

139. Fleisch, H., *From polyphosphates to bisphosphonates and their role in bone and calcium metabolism*, in *Inorganic Polyphosphates*. 1999, Springer. p. 197-216.

140. Wayburn, B. and T. Volk, *LRT, a tendon-specific leucine-rich repeat protein, promotes muscle-tendon targeting through its interaction with Robo.* Development, 2009. **136**(21): p. 3607-3615.

141. Ren, K., et al., *Macromolecular prodrug of dexamethasone prevents particle-induced peri-implant osteolysis with reduced systemic side effects.* Journal of Controlled Release, 2014. **175**: p. 1-9.

142. Gao, S.-Q., et al., *Biodistribution and pharmacokinetics of colon-specific HPMA copolymer–9-aminocamptothecin conjugate in mice.* Journal of controlled release, 2007. **117**(2): p. 179-185.

143. Pan, H., et al., *Biodistribution and pharmacokinetic studies of bone-targeting N-(2-hydroxypropyl) methacrylamide copolymer− alendronate conjugates.* Molecular pharmaceutics, 2008. **5**(4): p. 548-558.

144. Quan, L.-d., et al., *Pharmacokinetic and biodistribution studies of N-(2-hydroxypropyl) methacrylamide copolymer-dexamethasone conjugates in adjuvant-induced arthritis rat model.* Molecular pharmaceutics, 2010. **7**(4): p. 1041-1049.

145. Lai, J.T., D. Filla, and R. Shea, *Functional polymers from novel carboxyl-terminated trithiocarbonates as highly efficient RAFT agents.* Macromolecules, 2002. **35**(18): p. 6754-6756.

146. Liu, X.-M., et al., *Synthesis and Evaluation of a Well-defined HPMA Copolymer–Dexamethasone Conjugate for Effective Treatment of Rheumatoid Arthritis.* Pharmaceutical Research, 2008. **25**(12): p. 2910-2919.

147. Ren, K., et al., *Macromolecular glucocorticoid prodrug improves the treatment of dextran sulfate sodium-induced mice ulcerative colitis.* Clinical Immunology, 2015. **160**(1): p. 71-81.

148. Purdue, P.E., et al., *Development of polymeric nanocarrier system for early detection and targeted therapeutic treatment of peri-implant osteolysis.* HSS Journal®, 2013. **9**(1): p. 79-85.

149. Maeda, H., *The enhanced permeability and retention (EPR) effect in tumor vasculature: the key role of tumor-selective macromolecular drug targeting.* Advances in enzyme regulation, 2001. **41**(1): p. 189-207.

150. Zhang, Y., et al., *The Evaluation of Therapeutic Efficacy and Safety Profile of Simvastatin Prodrug Micelles in a Closed Fracture Mouse Model.* Pharmaceutical research, 2016. **33**(8): p. 1959-1971.

151. Jia, Z., et al., *Simvastatin prodrug micelles target fracture and improve healing.* Journal of Controlled Release, 2015. **200**: p. 23-34.

152. Allmeroth, M., et al., *PEGylation of HPMA-based block copolymers enhances tumor accumulation in vivo: A quantitative study using radiolabeling and positron emission tomography.* Journal of controlled release, 2013. **172**(1): p. 77-85.

153. Etrych, T., et al., *HPMA copolymer-doxorubicin conjugates: The effects of molecular weight and architecture on biodistribution and in vivo activity.* Journal of controlled release, 2012. **164**(3): p. 346-354.

154. Ren, K., et al., *Early diagnosis of orthopedic implant failure using macromolecular imaging agents.* Pharmaceutical research, 2014. **31**(8): p. 2086-2094.

155. Quan, L., et al., *The evaluation of the therapeutic efficacy and side effects of a macromolecular dexamethasone prodrug in the collagen-induced arthritis mouse model.* Pharmaceutical research, 2016. **33**(1): p. 186-193.

156. Yu, Q., et al., *Polymer–Doxorubicin Conjugate Micelles Based on Poly (ethylene glycol) and Poly (N-(2-hydroxypropyl) methacrylamide): Effect of Negative Charge and Molecular Weight on Biodistribution and Blood Clearance.* Biomacromolecules, 2015. **16**(9): p. 2645-2655.

157. Kettiger, H., et al., *Engineered nanomaterial uptake and tissue distribution: from cell to organism.* International journal of nanomedicine, 2013. **8**: p. 3255.

158. Drobník, J. and F. Rypáček, *Soluble synthetic polymers in biological systems*, in *Polymers in Medicine*. 1984, Springer. p. 1-50.

159. Fleischmann , R., et al., *Placebo-Controlled Trial of Tofacitinib Monotherapy in Rheumatoid Arthritis.* New England Journal of Medicine, 2012. **367**(6): p. 495-507.

160. Fleischmann, R., et al., *Phase IIb dose-ranging study of the oral JAK inhibitor tofacitinib (CP-690,550) or adalimumab monotherapy versus placebo in patients with active rheumatoid arthritis with an inadequate response to disease-modifying antirheumatic drugs.* Arthritis & Rheumatism, 2012. **64**(3): p. 617-629.

161. Kremer, J.M., et al., *The safety and efficacy of a JAK inhibitor in patients with active rheumatoid arthritis: Results of a double-blind, placebo-controlled phase IIa trial of three dosage levels of CP-690,550 versus placebo.* Arthritis & Rheumatism, 2009. **60**(7): p. 1895-1905.

162. van Vollenhoven , R.F., et al., *Tofacitinib or Adalimumab versus Placebo in Rheumatoid Arthritis.* New England Journal of Medicine, 2012. **367**(6): p. 508-519.

163. Lee, E.B., et al., *Radiographic, Clinical and Functional Comparison of Tofacitinib Monotherapy Versus Methotrexate in Methotrexate-Nave Patients with Rheumatoid Arthritis.* Arthritis and Rheumatism, 2012. **64**(Supplement 10): p. 2486.

164. Kremer, J.M., et al., *A phase IIb dose-ranging study of the oral JAK inhibitor tofacitinib (CP-690,550) versus placebo in combination with background methotrexate in patients with active rheumatoid arthritis and an inadequate response to methotrexate alone.* Arthritis & Rheumatism, 2012. **64**(4): p. 970-981.

165. Burmester, G.R., et al., *Tofacitinib (CP-690,550) in combination with methotrexate in patients with active rheumatoid arthritis with an inadequate response to tumour necrosis factor inhibitors: a randomised phase 3 trial.* The Lancet, 2013. **381**(9865): p. 451-460.

166. Tanaka, Y., et al., *Phase II study of tofacitinib (CP-690,550) combined with methotrexate in patients with rheumatoid arthritis and an inadequate response to methotrexate.* Arthritis Care & Research, 2011. **63**(8): p. 1150-1158.

167. van der Heijde, D., et al., *Tofacitinib (CP-690,550) in patients with rheumatoid arthritis receiving methotrexate: Twelve-month data from a twenty-four–month phase III randomized radiographic study.* Arthritis & Rheumatism, 2013. **65**(3): p. 559-570.

168. Kremer, J., et al., *Tofacitinib in combination with nonbiologic disease-modifying antirheumatic drugs in patients with active rheumatoid arthritis: A randomized trial.* Annals of Internal Medicine, 2013. **159**(4): p. 253-261.

169. Tanaka, Y., *Recent progress and perspective in JAK inhibitors for rheumatoid arthritis: from bench to bedside.* Journal of Biochemistry, 2015. **158**(3): p. 173-179.

170. Wu, X., et al., *Identification of related substances in tofacitinib citrate by LC-MS techniques for synthetic process optimization.* Journal of Pharmaceutical and Biomedical Analysis, 2017. **143**: p. 17-25.

171. Nam, J.L., et al., *Efficacy of biological disease-modifying antirheumatic drugs: a systematic literature review informing the 2016 update of the EULAR recommendations for the management of rheumatoid arthritis.* Annals of the Rheumatic Diseases, 2017.

172. Schwartz, D.M., et al., *Type I/II cytokines, JAKs, and new strategies for treating autoimmune diseases.* Nat Rev Rheumatol, 2016. **12**(1): p. 25-36.

173. O'Shea, J.J., A. Laurence, and I.B. McInnes, *Back to the future: oral targeted therapy for RA and other autoimmune diseases.* Nat Rev Rheumatol, 2013. **9**(3): p. 173-182.

174. Yuan, F., et al., *A Dexamethasone Prodrug Reduces the Renal Macrophage Response and Provides Enhanced Resolution of Established Murine Lupus Nephritis.* PLOS ONE, 2013. **8**(11): p. e81483.

175. Yuan, F., et al., *Dexamethasone prodrug treatment prevents nephritis in lupus-prone (NZB × NZW)F1 mice without causing systemic side effects.* Arthritis & Rheumatism, 2012. **64**(12): p. 4029-4039.

176. Gabriel, S.E., *The Epidemiology of Rheumatoid Arthritis.* Rheumatic Disease Clinics of North America, 2001. **27**(2): p. 269-281.

177. Olsen , N.J. and C.M. Stein *New Drugs for Rheumatoid Arthritis.* New England Journal of Medicine, 2004. **350**(21): p. 2167-2179.

178. Mankia, K. and P. Emery, *Preclinical Rheumatoid Arthritis: Progress towards Prevention.* Arthritis & Rheumatology, 2016: p. 779-88.

179. LaBranche, T.P., et al., *JAK inhibition with tofacitinib suppresses arthritic joint structural damage through decreased RANKL production.* Arthritis & Rheumatism, 2012. **64**(11): p. 3531-3542.

180. Takeshita, S., K. Kaji, and A. Kudo, *Identification and Characterization of the New Osteoclast Progenitor with Macrophage Phenotypes Being Able to Differentiate into Mature Osteoclasts.* Journal of Bone and Mineral Research, 2000. **15**(8): p. 1477-1488.

181. Frangioni, J.V., *In vivo near-infrared fluorescence imaging.* Current Opinion in Chemical Biology, 2003. **7**(5): p. 626-634.

182. Bartok, B. and G.S. Firestein, *Fibroblast-like synoviocytes: key effector cells in rheumatoid arthritis.* Immunological Reviews, 2010. **233**(1): p. 233-255.

183. Dennis, G., et al., *Synovial phenotypes in rheumatoid arthritis correlate with response to biologic therapeutics.* Arthritis Research & Therapy, 2014. **16**(2): p. R90.

184. Buckley, C.D. and A. Filer, *Chapter 14 - Fibroblasts and Fibroblast-like Synoviocytes A2 - Firestein, Gary S*, in *Kelley and Firestein's Textbook of Rheumatology (Tenth Edition)*, R.C. Budd, et al., Editors. 2017, Elsevier. p. 231-249.e4.

185. Boyle, D.L., et al., *The JAK inhibitor tofacitinib suppresses synovial JAK1-STAT signalling in rheumatoid arthritis.* Annals of the Rheumatic Diseases, 2015. **74**(6): p. 1311-1316.

186. Dowty, M.E., et al., *The Pharmacokinetics, Metabolism, and Clearance Mechanisms of Tofacitinib, a Janus Kinase Inhibitor, in Humans.* Drug Metabolism and Disposition, 2014. **42**(4): p. 759-773.

187. *European Medicines Agency Assessment report EMA/CHMP/425279/2013*. European Medicines Agency